Study on position-controlled GaN nanorod arrays and their

application to three dimensional light emitting diodes

JUNG Byungoh

Study on position-controlled GaN nanorod arrays and their application to three dimensional light emitting diodes

JUNG Byungoh

Nagoya University

Graduate School of Engineering

Department of Electrical Engineering and Computer Science

窒化ガリウムナノ構造の選択成長と

3次元発光ダイオードに関する研究

鄭 柄 午

名古屋大学

工学研究科

電子情報システム専攻電子工学分野

ABSTRACT OF THIS THESIS

Study on position-controlled GaN nanorod arrays and their application to three dimensional light emitting diodes

By JUNG Byungoh

Thesis Advisor: Professor Hiroshi Amano

As reported in this thesis, the realization and characterization of artificially position-controlled gallium nitride (GaN) nanorods have been investigated to establish nanostructure arrays for GaN-based core-shell architecture embedded three-dimensional (3D) light-emitting diodes (LEDs). The basic strategies for the selective area growth (SAG) of GaN nanorod arrays are (i) the utilization of catalyst-free metalorganic chemical vapor deposition (MOCVD) for material synthesis, (ii) the deployment of an amorphous growth mask such as SiO_2 or SiN for position-controlled growth, (iii) the use of a *c*-axis-oriented thick GaN underlayer as an epitaxial seed and conducting layer, and (iv) the use of the well-established MOCVD technique for heteroepitaxy and the growth of the LED structure. The systematic position-controlled and selective growth of GaN nanorod arrays was advanced and successfully demonstrated using these strategies. In addition, the formation mechanism, the physical and optical properties of the grown GaN nanorod arrays, and their core-shell architecture were investigated in more detail. First, pulsed-mode MOCVD growth was carried out to realize the selective growth of GaN nanorod arrays with shape-controlled GaN nanorods. In particular, the effect of the gas injection and interruption timing on pulsed-mode MOCVD growth were investigated. Also, the influence of growth conditions such as the temperature, pressure, patterning, and V/III ratio on SAG GaN nanorod arrays was studied. Additionally, the physical and optical properties of grown GaN nanorod arrays under

ABSTRACT

different synthesis conditions were examined by high-resolution transmission electron microscopy (HR-TEM) and photoluminescence (PL) measurement. Next, highly-ordered, position-controlled GaN nanorod based $In_xGa_{1-x}N$/GaN multiple-quantum-wells (MQWs) core-shell architecture arrays were synthesized by MOCVD. In particular, the possibility of using GaN nanorod arrays as a basal template for the growth of $In_xGa_{1-x}N$/GaN MQWs was investigated. The structural characteristics of $In_xGa_{1-x}N$/GaN core-shell arrays were inspected by cross-sectional HR-TEM. Also, the luminescent characteristics of the MQWs core-shell architecture were determined by PL and cathodoluminescence (CL) measurements. It was found that the light emission intensity shows different behavior depending on the area of the GaN nanorod $\{1\bar{1}00\}$ m-plane sidewalls. Finally, the fabrication and characterization of a 3D-LED structure were demonstrated using $In_xGa_{1-x}N$/GaN core-shell arrays with the growth of p-GaN. The temperature and excitation power dependences of the PL measurements were carried out to reveal the physical and optical properties of this structure. The realized 3D-LED showed color-changeable luminescence properties from the green to blue region upon adjusting the external applied bias. This phenomenon might be related to features of the MQWs such as the thickness and the dissimilar indium incorporation rates in $In_xGa_{1-x}N$ quantum-wells caused by different crystal facets of GaN nanorods. These results are essential for realizing effective light emission in the longer-wavelength region. The position-controlled 3D structure grown by MOCVD is expected to lead to substantial opportunities for realizing next-generation optoelectronic technologies.

CONTENTS

Chapter 1

Introduction

1.1 Overview of semiconductor nanorod structures

Nanotechnology (or nanotech) is the manipulation of matter on an atomic, molecular, or supramolecular scale (1~1000 Å).[1] Nanotechnology is opening up a new paradigm in a wide variety of application fields to create new materials, structures, devices, and physical and chemical phenomena. Therefore, in a wide range of areas of human life such as the industrial, environmental, ergonomical, and scientific fields, it is expected that nanotech will become the most significant technology for future developments. Examples include clothes that are more stain-repellant, sunscreen that is more radiation-resistant, car bumpers that are lighter, glass packaging for drinks with a longer lifetime or greater reusability, synthetic bones that are more powerful or have a longer shelf-life, and smart phone displays that are brighter and lighter.[2] Nanotechnology is now producing advances diverse semiconductor based application fields, such as the electrical, optical, and optoelectronic fields, through the use of semiconductor nanostructures including nanorods, nanotubes, nanocones, nanoparticles, quantum-wells, quantum dots, and etc.) especially nanorod and nanowire structure. As shown in Fig. 1.1., nanorod structures (both axial and radial) have been considered as a key factor in realizing new types of self-integrated electric circuit and for improving device performances such as the sensitivity of sensor applications, the conversion efficiency of solar cells, and the light emission efficiency of light-emitting diodes (LEDs). This is due to their potential for exhibiting novel phenomena and exotic chemical and physical properties such as defect-free structure, a large surface area to volume ratio, or a high aspect ratio. Consequently, a large number of studies have concentrated on developing methods for synthesizing materials and
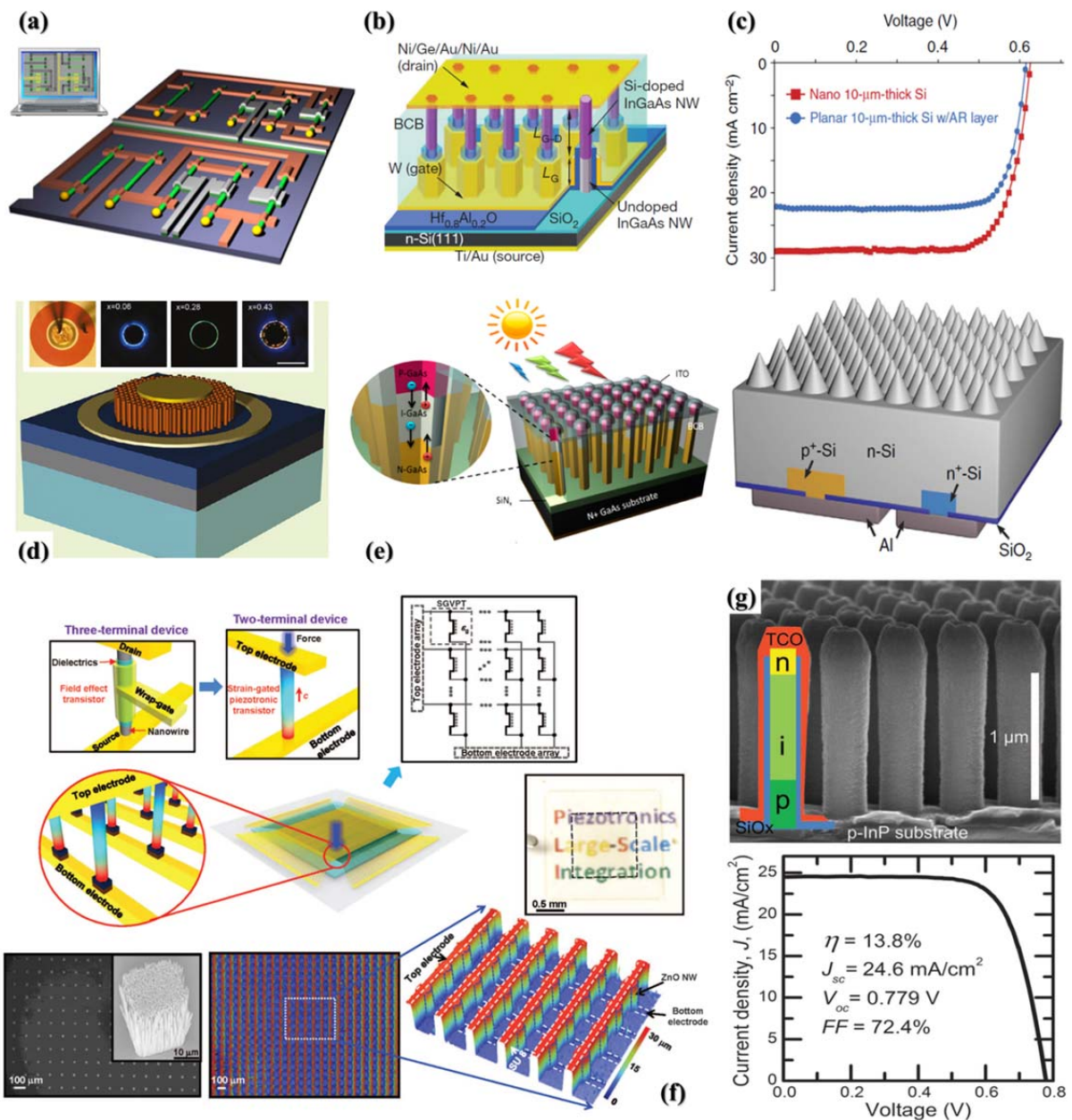
Figure 1.1 Various nanostructure-based electronic and optoelectronic devices applications. (a) Self-integration of nanowires into circuits. (b) InGaAs-nanowire channel based vertical transistor. (c) Silicon (Si)-nanocone based solar cell with high power conversion efficiency. (d) InGaN-nanowire based LED. (e) GaAs-nanowire array solar cell with axial p-i-n junctions. (f) Taxel-addressable matrix of vertical-nanowire piezotronic transistors. (g) InP-nanowire array based solar cell with 13.8% efficiency.[3-9)]

device fabrication within the field of opto-electronic devices application in recent years.

Typically, there are two types of approach to manufacturing nanorod structures (nanowires, nanocolumns, and nanocylinders, i.e., building block structures) regardless of the material. (i) The first is a top-down approach, in which a large amount of material is reduced to small parts by lithography. Although this technique is the most successful, accessible, and easiest way to fabricate nanorods structures owing to the straightforward patterning, lithography, and etching procedures previously used for micro-optoelectronics. However, due to the latest possibilities of nanoscale (1~1000 Å) structures and the problems of the top-down approach such as economic limitations and scientific issues, recent research trend have inclined to realize novel phenomena or behaviors toward bottom-up based synthesis techniques. (ii) The second is bottom-up approaches. The meaning of bottom-up is to synthesize the nanostructure by combining constituent adatoms which functional structures are integrated from well-confined physically and chemically synthesized nanorod arrays. This is an important alternative approach in substitute for typical top-down methods. Studies on nanorod structures formed by a bottom-up growth technique have been extensively carried out, particularly focusing on the field of optoelectronics devices, to utilize the properties such structures including perfect crystallinity, mismatched material combinations, and atomically sharp interfaces. Nanorod structures have led to the realization of novel physical, chemical, optical, and structural properties by reducing of their size. For example, the reducing the size can lead to the effective transport of electrical carriers, enabling their effective adoption within assembled nanoscale electrical systems. In this manner, nanorod structures can also play an important role in the field of electronic, optoelectronic, optical, electrochemical, electromechanical, electrophysical, medical, and magnetic devices owing to their innovative properties resulting from their nanoscale dimensions or size.[10-14] One-dimensional (1D) nanorod array structures have generated considerable interest in the last few decades ever

since it was discovered that they can produce artificial potentials in semiconductors for electrons, holes, and carriers, at length scales comparable to or shorter than the de Broglie wavelength.[15] Therefore, the quantum confinement effect in semiconductors becomes not only significant, but adjustable to a large degree as well. It has been confidently predicted that the quantum confinement of carriers by the potential wells of a nanoscale structure can generate one of the most versatile and powerful ways to govern numerous properties of solid-state functional materials such as their optical, electrical, physical, and magnetic properties.[16] Consequently, the realization of new devices for application in the optical, electrical, optoelectronic, and other fields is practicable through the use of the confinement effect, which provides supplementary degrees of freedom in the design. Among the numerous semiconductor materials for which nanorod structures can be fabricated the III-V compound semiconductors stand out as among the most versatile materials owing to their excellent functionalities, properties, and potential for utilization in various application fields. Nanorod arrays based on III-V materials exhibit not only unique properties that can be utilized in many ways to the improve performance of devices, but also possess unusual characteristics associated with the size confinement and anisotropic geometry.

1.2 Importance of Gallium Nitride (GaN)

Among the numerous III-V compound semiconductor materials, the research history of gallium nitride (GaN) and LEDs, which are the representative GaN-based device, will be introduced in this chapter. GaN and related group III-nitride compound semiconductors (AlN, InN, InGaN, and AlGaN) have established themselves as important materials for realizing revolutionary semiconductor device systems such as visible-wavelength optoelectronic devices,[17-19] power electronics,[20] and high-frequency electronics.[21] This kind of interesting is mainly due to their special bandgap energy characteristics covering a broad spectrum from

ultraviolet (UV) to infrared (IR). In particular, III-N systems have been widely utilized in full color displays, solid-state lighting, and high-density information storage in people's everyday lives. In addition, III-N materials have high thermal and chemical stability, allowing them to be utilized in extremely harsh environments.[22]

1.2.1 Properties of GaN

III-N materials can be crystallized into three different types of alloy systems, binary (A_xB_{1-x}), ternary ($A_xB_{1-x}C$), and quaternary ($A_xB_{1-x}C_yD_{1-y}$), ($A_xB_yC_{1-x-y}D$), or ($AB_xC_yD_{1-x-y}$) alloy systems. In particular, the binary-alloy-system-based III-N materials such as GaN, InN, and AlN have wurtzite or zinc-blende crystal structures as shown in Fig. 1.2, (which shows the case of GaN).
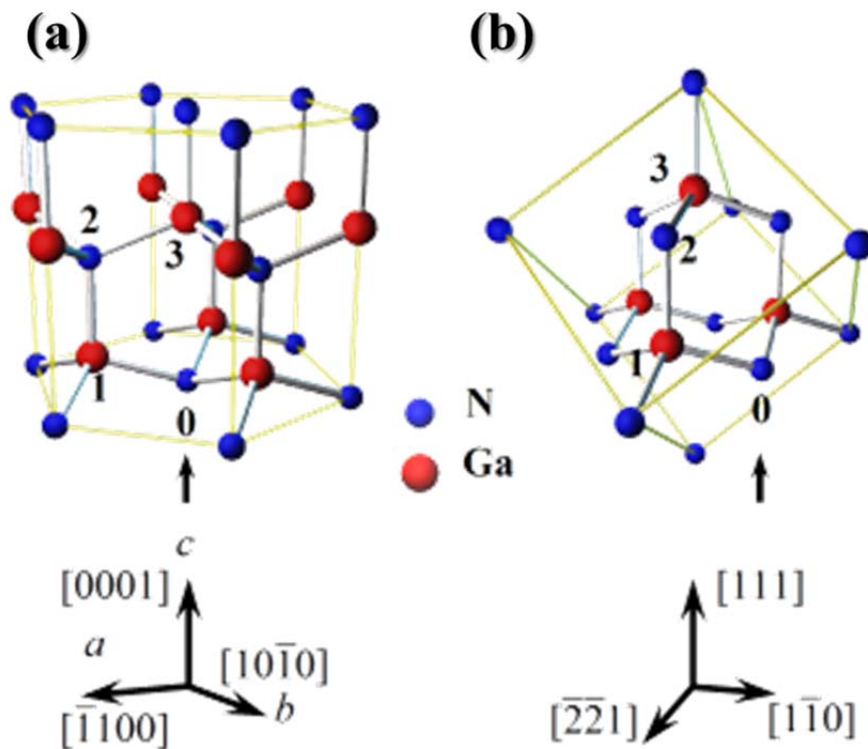
Figure 1.2 Arrangements of crystal structure: (a) hexagonal (wurtzite), and (b) cubic (zinc-blende) GaN.

The zinc-blende (cubic) structure of GaN and InN has a direct bandgap energy, while AlN has an indirect bandgap.[23] GaN, InN, and AlN have direct bandgap energies of 3.42, 0.7, and 6.1 eV, respectively, at room temperature for the wurtzite (hexagonal) crystal structure.[17, 22] The lattice constant versus the bandgap energy in various nitride and related materials is summarized in Fig. 1.3. Also, nitride materials have larger elastic stiffness constant than other compound semiconductor materials such as III-V and II-VI materials as shown in Table 1.1.[17]

Table 1.1 Elastic stiffness constants (c_{ij}) of III-N, III-V (GaAs), and II-VI (ZnSe).[17, 24]

	Wz-AlN	Wz-GaN	Wz-InN	ZB-GaN	GaAs	ZnSe
c_{13} ($\times 10^{11}$ dyn/cm^2)	12.0	11.4	9.4			
c_{33} ($\times 10^{12}$ dyn/cm^2)	39.5	38.1	20.0			
c_{11} ($\times 10^{11}$ dyn/cm^2)				26.4	11.88	8.59
c_{12} ($\times 10^{11}$ dyn/cm^2)				15.3	5.82	5.06
c_{44} ($\times 10^{11}$ dyn/cm^2)				6.8	5.94	4.06

This results in strong bonds between group III and nitrogen atoms. Therefore, GaN is a very hard and thermally, chemically, and mechanically stable material. Silicon (Si) and magnesium (Mg) have been utilized as *n*-type and *p*-type doping sources of GaN, respectively.[25-27] GaN possesses various special characteristics such as a wide bandgap energy (3.42 eV), which can be utilized in optoelectronic device applications field. GaN has a high saturation velocity (2.5×10^5 *m·s*$^{-1}$), and breakdown field (3×10^6 *V·cm*$^{-1}$ @ 300 K). These properties can be used in electronic devices such as high-frequency and high-power transistors. The high absorption coefficient (4×10^4 cm^{-1}) of GaN for wavelengths shorter than 365 nm makes it a suitable for use in visible-blind UV photodetectors. Other fundamental properties of the nitride semiconductors are given in Table 1.2. These properties have enabled the development of various devices application for over 50 years.
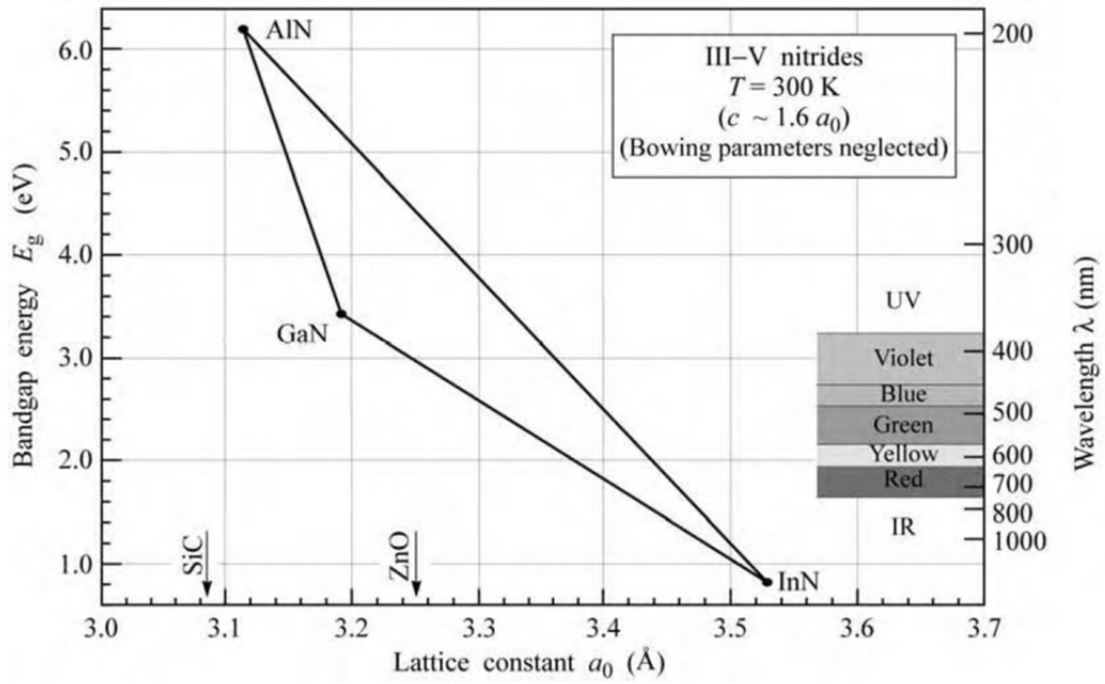
Figure 1.3 Lattice constant versus bandgap energy of III-nitride compound semiconductor materials at room temperature.[28]

Table 1.2 Fundamental properties of AlN, GaN, and InN compound semiconductors.[29]

	AlN	GaN		InN
		Zinc blende	Wurzite	
Bandgap Energy (eV)	6.10	3.20	3.42	0.70
Lattice Constant (Å)	a = 3.112 c = 4.892	a = 4.52	a = 3.189 c = 5.185	a = 3.533 c = 5.693
Thermal Expansion Coefficient (10^{-6}/K)	$\Delta a/a = 4.2$ $\Delta c/c = 5.3$	$\Delta a/a = 5.59$ $\Delta c/c = 3.17$		$\Delta a/a = 3.8$ $\Delta c/c = 2.9$
Thermal Conductivity (W/m·K)	285	130		45
Melting Point (K)	3487	2791		2146
Index of Refraction	2.15	2.3		2.9
Dielectric Constant	8.5	9.7	8.9	15.3
Effective Electron Mass (m_0)	0.4	0.13	0.2	0.11

1.2.2 GaN-based light-emitting diodes (LEDs)

Although Juza *et al*. first reported the synthesis of GaN from liquid Ga metal with ammonia (NH_3) at an elevated temperature in 1938,[30] the GaN did not attract any interest owing to the difficulty of its synthesis. In 1959, Grimmeiss *et al*. demonstrated the growth of small crystals of GaN by the synthesis technique of Juza *et al*. in order to measure the GaN photoluminescence (PL) spectrum. Maruska *et al*. reported the growth of single-crystalline GaN on a sapphire substrate in NH_3 atmosphere by a vapor-phase growth method and its bandgap properties in 1969.[31] Pankove *et al*. first demonstrated the possibility of using GaN as a light emitter by fabricating a metal-insulator-semiconductor (MIS) structure with a undoped *n*-type layer, a Zn-doped insulating region, and an indium surface contact in the early 1970s, which showed blue and green light emission upon current injection.[32] Actually, many researchers attempted to demonstrate light emission in 1970s in addition to Pankove *et al*. Despite significant physical discoveries about the synthesis and properties of GaN, there were no conclusive studies at that time as to improve crystal quality of GaN. The most difficult problems in realizing high-efficiency GaN-based LEDs were the growth of highly crystalline GaN and a *p*-type GaN layer. However, Prof. Hiroshi Amano first developed the novel growth technique of employing low-temperature buffer layers for the synthesis of high-quality group III-N semiconductor thin-films on a sapphire substrate in 1985,[33] which led to the realization of III-N materials based LEDs and laser diodes (LDs). In addition, he was the first person to produce *p*-type conductive GaN by *electron-beam irradiation* and he fabricated *p-n* junction type GaN-based UV and visible LEDs at 1989.[26] After his discovery, a high temperature *post-annealing* technique for the activation of Mg acceptors was introduced by Prof. Shuji Nakamura in 1992.[27] LEDs are considerably more energy-efficient than incandescent and fluorescent light bulbs, leading to both environmental and financial benefits as well as energy conservation. These technical developments led to the present

successful *p-n* junction LEDs and LDs. Especially, Prof. Isamu Akasaki, Hiroshi Amano, and Shuji Nakamura were awarded the Nobel Prize in Physics 2014 for their contribution to the development of GaN-based LEDs.[34]

1.3 Research history of III-N materials crystal growth

The growth of III-N materials began in 1928 and there have been several important advances in their synthesis during their long research history. (i) The synthesis of AlN by Tiede *et al.*,[35] (ii) the discovery of GaN through the reaction of NH_3 and Ga by Johnson *et al.*,[36] (iii) the synthesis of InN by Juza *et al.*,[30] (iv) the growth of single-crystal GaN via hydride vapor phase epitaxy (HVPE) by Maruska *et al.*,[31] (v) the insertion of a nucleation layer by Amano *et al.*,[33] (vi) the achievement of *p*-GaN through Mg doping by Amano *et al.*,[26, 37], (vii) the bandgap engineering of nitride-related materials such as In, Ga, and Al III-V compound systems by Matsuoka *et al.*[38], and (viii) the growth of a high-quality InGaN layer by Nakamura *et al.*[39] Various growth techniques have been developed in the field of III-N materials including catalyst-free and catalyst-assisted growth methods. However, catalyst-free growth techniques such as metalorganic chemical vapor deposition (MOCVD), which is the same as metalorganic vapor phase epitaxy (MOVPE) and organometallic vapor phase epitaxy (OMVPE), as well as HVPE and molecular beam epitaxy (MBE), have received considerable attention owing to their many advantages.[33, 39, 40] In particular, over the past 30 years, MOCVD has become the primary epitaxial growth technique for the synthesis of high-quality III-V materials.[40, 41] MOCVD was first developed by Manasevit in 1968 for the growth of GaAs epitaxial layers.[42] Since then, MOCVD has become the most popular growth technique in the field of compound semiconductors owing to the development of the technology. In more recent LED market, most commercial GaN-based LEDs have been manufactured by MOCVD growth.

1.4 Current research status of nanostructures and selective area growth (SAG)

Research on various semiconductor-nanostructure based electronic and photonic device applications has mainly followed a bottom-up approach in the last decade.[43-47] Since the development of bottom-up synthetic methods, single-crystalline nanomaterials have attracted great interest, and it is expected that high-crystallinity materials based on homo- or hetero-structure can be used as components of functional device applications.[47-49] In addition, nanostructured materials self-assembled by bottom-up growth method do not require a complex fabrication process such as lithography or etching to control the scaling and morphology. Among the various types of 1D nanostructure, nanorods or nanowires have received most attention owing to their simple fabrication and manipulation to realize numerous device applications.[48, 50-52] Furthermore, the versatility of nanorod arrays allows them to be used to create heterostructures in not only the longitudinal direction but also the radial direction, making them more suitable for the realization of nanostructure-based optoelectronic device applications than other nanostructures based devices.[53-55] Specifically, both the high aspect ratio and the large surface-to-volume ratio of nanorod arrays can play a key role in enhancing the output performance of device applications such as the light efficiency of LEDs and photovoltaic devices,[9, 55] sensitivity or responsivity of optical, chemical, and biological sensors,[14, 56, 57] and the electrical properties of electronic devices.[4, 8] Also, the nanorod structure is expected to filter out structural defects such as dislocations owing to their nanoscaled dimensions.[58, 59] These ideas have been utilized in nanorod-based superlattice structures along both the radial and longitudinal directions by modulating reactants within various materials during synthesis. These structures include GaAs/AlGaAs core-shell nanowires,[55] InAs/InP nanowires,[59] Si/SiGe superlattice nanowires,[60] carbon nanotube (CNT)/Si nanowire heterostructures,[61] and even more refined ZnO/MgZnO coaxial structures.[62] The exploitation of nanorod and nanowire-based heterostructures can be

expanded to the field of LEDs, enabling their utilization as lighting sources with more extended larger junction area than that of conventional planar devices. To effectively utilize the unique properties of nanorod structures, scalable and accurate techniques for the growth of semiconductor nanorods have become more important factor in various application fields. In particular, the selective area growth (SAG) of compound semiconductor nanorod arrays is expected to lead to a major breakthrough in not only optoelectronic applications but electronic applications as well. Spatially independent nanorod structures allow to the fabrication of complicated three-dimensional (3D) device structures more easily than self-assembled non-separated nanorod arrays used for vertical device architectures. Furthermore, the development of the position-controlled SAG of nanorod arrays is positively necessary to advance nanoscale Si flash memory devices, integration systems, super-junction structures, and electronic circuitry in addition to photonic device applications.[3, 63] Several well-established SAG techniques have been developed that are based on not only catalyst-free approaches such as MOCVD and MBE but also metal-catalyst-assisted methods such as vapor-liquid-solid (VLS) technique on patterned substrates in the past.[64-66] Although position-controlled growth techniques is more complicated than non-position-controlled synthesis for producing various appliances, the position-controlled SAG of nanorod arrays combined with catalyst-free growth techniques is expected to improve the output performance of devices owing to their many advantages as explained above.[9, 16]

1.5 Objectives of this research

According to the previous section, nanorods structures grown by a fundamental bottom-up approach using a catalyst-free growth technique may provide an ideal geometry for 3D optoelectronic device structure. However, bottom-up based nanostructures and most applications are still at an early stage compared with the conventional thin-film planar

structure. Many unsolved problems clearly remain and more work will be needed before this type of nanostructure can be utilized conventional industrial applications. Several questions can be proposed: (i) Can we grow position-controlled nanorod structures using typical epitaxy technology ? If not, why not ? (ii) How can we grow or synthesize well-aligned nanorod arrays with high quality ? (iii) Which techniques can be used for the fabrication of 3D device structures with a large area ? (iv) Do such structures have any advantages or exhibit interesting phenomena ? compared with conventional structure ? Answering these questions will be a huge challenge. However, we consider that such questions can be solved by applying well-established techniques in semiconductor technologies. Therefore, to answer these questions, this research involves the three topics as shown in Fig. 1.4.
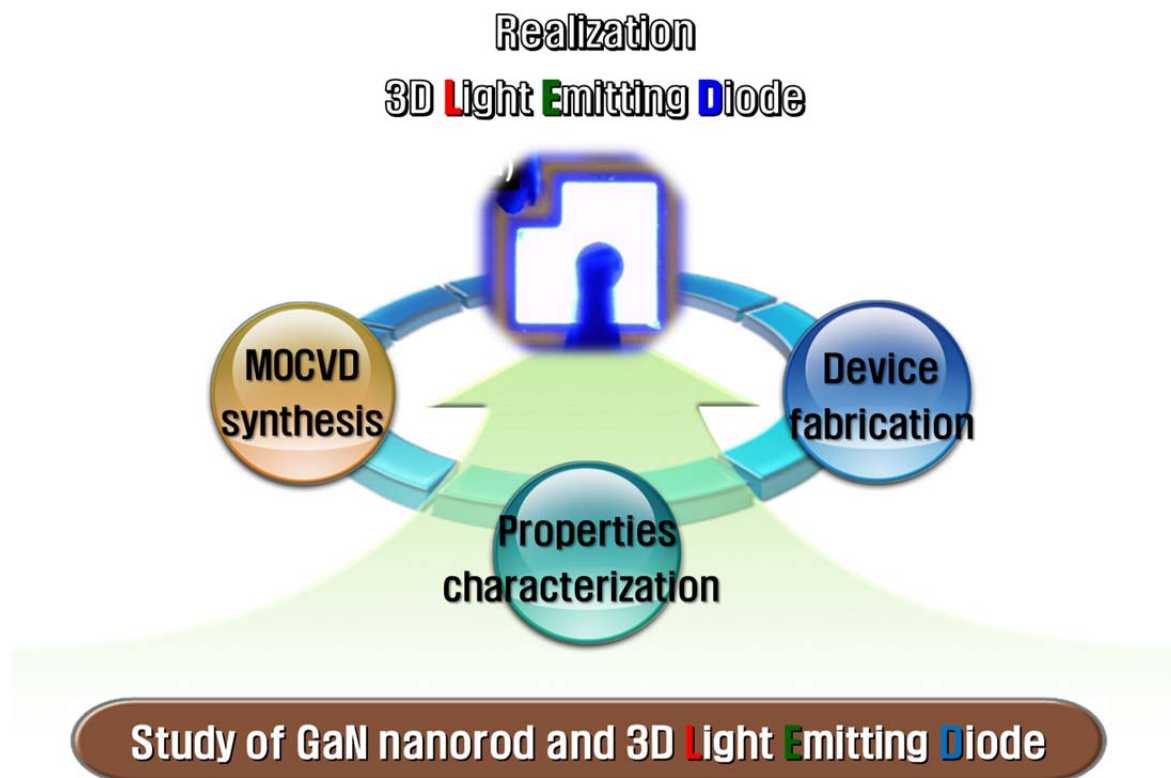
Figure 1.4 Schematic diagram showing the topics in this thesis.

The first purpose of this thesis is to (i) present a special MOCVD growth technique for the SAG of GaN nanorods with low-dimensional features and morphological evolution. This special MOCVD growth technique with optimal growth conditions is required to control the physical and chemical reactions in the SAG of GaN nanorod arrays. The second is to (ii) describe the physical, optical, and structural characterization of selective-area-grown GaN nanorod arrays and its based $In_xGa_{1-x}N$/GaN multiple-quantum-well (MQW) core-shell architecture. Owing to their distinctive properties such as their nanoscale structure and different crystal facets, the MQW core-shell architecture exhibits different characteristics from planar structures. Therefore, the understanding of their optical and physical properties is important for realizing the 3D-LED structures. The final purpose is to (iii) fabricate an $In_xGa_{1-x}N$/GaN MQW core-shell nanorods embedded 3D-LED structure. Through these three research topics, this research aims to prove that a 3D-LED structure can act as a more efficient lighting source than a conventional structure.

1.6 Synopsis of thesis

This thesis is organized into the following chapters as also shown in Fig. 1.5. Chapter 2 describes the experimental process including the growth method, characterization tools, and patterning procedures. In Chapter 3, the pulsed-mode MOCVD growth technique for the SAG of GaN nanorod arrays and the evolution of their morphology are presented, and the physical and optical properties of the grown GaN nanorod arrays are discussed. Chapter 4 explains ways of optimizing the growth conditions to obtain high-quality GaN nanorod arrays through the control of various growth parameters in pulsed-mode MOCVD procedure. Chapter 5 examines the possibility of using GaN nanorod arrays as a basal template for the growth of $In_xGa_{1-x}N$/GaN MQWs. In particular, the structural and optical characteristics of $In_xGa_{1-x}N$/GaN MQW core-shell architecture arrays are investigated by various analysis tools

such as PL and cathodoluminescence (CL) measurement, and high-resolution transmission electron microscopy (HR-TEM). Chapter 6 reports the analysis of the light emission properties of $In_xGa_{1-x}N$/GaN MQW core-shell architecture arrays, and the fabrication of the 3D-LED structure. The chapter mainly focuses on revealing its electrical and luminescent properties. Finally, chapter 7 summarizes this thesis and discusses future directions of research and the prospect of GaN-nanorod based 3D-LEDs.

Chapter 1. Introduction

- Background of this study: fundamental study of GaN material & nanostructure
- History of GaN-based light emitting diode and MOCVD growth technology
- Application of nanostructures and current status of position-controlled selective area growth (SAG)

Chapter 2. Technical background: MOCVD & T-NIL processes

- Introduction of metalorganic chemical vapor deposition (MOCVD) equipment used in this work
- Introduction of thermal nanoimprinting process used in this work

Chapter 3. Pulsed-mode MOCVD growth

- Growth of GaN nanorods by pulsed-mode MOCVD procedure
- Propose of growth model for GaN nanorods

Chapter 4. Optimal growth conditions

- Growth of GaN nanorods by pulsed MOCVD procedure under various growth conditions
- Characterization of properties of GaN nanorods

Chapter 5. InGaN/GaN core-shell nanorods

- Growth of $In_xGa_{1-x}N$/GaN MQWs core-shell nanorods
- Investigation of their structural properties

Chapter 6. 3D-Light Emitting Diode

- Investigation of optical properties of InGaN/GaN MQWs core-shell nanorods
- Realization of core-shell nanorod embedded LED and discussion of its properties

Chapter 7. Conclusions

Figure 1.5 Research flow of each chapter in this thesis.

1.7 References

1) K. E. Drexler '*Nanosystems: molecular machinery, manufacturing, and computation'*, John Wiley & Sons, Inc.: 1st Ed., (1992).

2) B. Bhushan '*Springer handbook of nanotechnology'*, Springer: 3rd Ed., (2010).

3) M. Schvartzman, D. Tsivion, D. Mahalu, O. Raslin, E. Joselevich; Proc. Nat. Acad. Sci. U.S.A. **110**, 15195 (2013).

4) K. Tomioka, M. Yoshimura, T. Fukui; Nature **488**, 189 (2012).

5) S. Jeong, M. D. McGehee, Y. Cui; Nat. Commun. **4**, 2950 (2013).

6) C. Hahn, Z. Zhang, A. Fu, C. H. Wu, Y. J. Hwang, D. J. Gargas, P. Yang; ACS Nano **5**, 3970 (2011).

7) M. Yao, N. Huang, S. Cong, C.-Y. Chi, M. A. Seyedi, Y.-T. Lin, Y. Cao, M. L. Povinelli, P. D. Dapkus, C. Zhou; Nano Lett. **14**, 3293 (2014).

8) W. Wu, X. Wen, Z. L. Wang; Science **340**, 952 (2013).

9) J. Wallentin, N. Anttu, D. Asoli, M. Huffman, I. Åberg, M. H. Magnusson, G. Siefer, P. Fuss-Kailuweit, F. Dimroth, B. Witzigmann; Science **339**, 1057 (2013).

10) G. Fasol; Science **280**, 545 (1998).

11) J. Xiang, W. Lu, Y. Hu, Y. Wu, H. Yan, C. M. Lieber; Nature **441**, 489 (2006).

12) R. S. Friedman, M. C. McAlpine, D. S. Ricketts, D. Ham, C. M. Lieber; Nature **434**, 1085 (2005).

13) Y. Wu, J. Xiang, C. Yang, W. Lu, C. M. Lieber; Nature **430**, 61 (2004).

14) S.-W. Hwang, G. Park, C. Edwards, E. A. Corbin, S.-K. Kang, H. Cheng, J.-K. Song, J.-H. Kim, S. Yu, J. Ng, J. E. Lee, J. Kim, C. Yee, B. Bhaduri, Y. Su, F. G. Omennetto, Y. Huang, R. Bashir, L. Goddard, G. Popescu, K.-M. Lee, J. A. Rogers; ACS Nano **8**, 5843 (2014).

15) J. Stangl, V. Holý, G. Bauer; Rev. Mod. Phys. **76**, 725 (2004).

16)   Y. Xia, P. Yang, Y. Sun, Y. Wu, B. Mayers, B. Gates, Y. Yin, F. Kim, H. Yan; Adv. Mater. **15**, 353 (2003).

17)   I. Akasaki, H. Amano; Jpn. J. Appl. Phys. **36**, 5393 (1997).

18)   F. Ponce, D. Bour; Nature **386**, 251 (1997).

19)   S. Nakamura, T. Mukai, M. Senoh; Jpn. J. Appl. Phys. **30**, L1998 (1991).

20)   M. A. Khan, A. Bhattarai, J. Kuznia, D. Olson; Appl. Phys. Lett. **63**, 1214 (1993).

21)   L. F. Eastman, V. Tilak, V. Kaper, J. Smart, R. Thompson, B. Green, J. Shealy, T. Prunty; Phys. Stat. Sol. (a) **194**, 433 (2002).

22)   J. Pankove, T. Moustakas, R. Willardson '*Gallium Nitride (GaN) I : Semiconductors and Semimetals'*, Academic Press: 1st Ed., Vol. 50, (1998).

23)   F. Litimein, B. Bouhafs, Z. Dridi, P. Ruterana; New J. Phys. **4**, 64 (2002).

24)   G. Martin, A. Botchkarev, A. Rockett, H. Morkoc; Appl. Phys. Lett. **68**, 2541 (1996).

25)   N. Koide, H. Kato, M. Sassa, S. Yamasaki, K. Manabe, M. Hashimoto, H. Amano, K. Hiramatsu, I. Akasaki; J. Cryst. Growth **115**, 639 (1991).

26)   H. Amano, M. Kito, K. Hiramatsu, I. Akasaki; Jpn. J. Appl. Phys. **28**, L2112 (1989).

27)   S. Nakamura, T. Mukai, M. Senoh, N. Iwasa; Jpn. J. Appl. Phys. **31**, L139 (1992).

28)   E. F. Schubert, T. Gessmann, J. K. Kim '*Light-Emitting Diodes'*, Cambridge University Press: 2nd Ed., (2006).

29)   L. Liu, J. H. Edgar; Mater. Sci. Eng. R **37**, 61 (2002).

30)   R. Juza, H. Hahn; Z. Anorg. Allg. Chem. **239**, 282 (1938).

31)   H. P. Maruska, J. Tietjen; Appl. Phys. Lett. **15**, 327 (1969).

32)   J. Pankove, E. Miller, D. Richman, J. Berkeyheiser; J. Lumin. **4**, 63 (1971).

33)   H. Amano, N. Sawaki, I. Akasaki, Y. Toyoda; Appl. Phys. Lett. **48**, 353 (1986).

34)   Y. Shi; Mod. Phys. Lett. B **29**, 1530001 (2015).

35)   E. Tiede, M. Thimann, K. Sensse; Chem. Berichte. **61**, 1568 (1928).

36) W. C. Johnson, J. Parson, M. Crew; J. Phys. Chem. **36**, 2651 (1932).

37) I. Akasaki, H. Amano, M. Kito, K. Hiramatsu; J. Lumin. **48**, 666 (1991).

38) T. Matsuoka, H. Tanaka, T. Sasaki, A. Katsui; Inst. Phys. Conf. Ser. **106**, 141 (1990).

39) S. Nakamura, T. Mukai; Jpn. J. Appl. Phys. **31**, L1457 (1992).

40) R. Moss; J. Cryst. Growth **68**, 78 (1984).

41) H. Moffat, K. F. Jensen; J. Cryst. Growth **77**, 108 (1986).

42) H. M. Manasevit; Appl. Phys. Lett. **12**, 156 (1968).

43) C. Murray, C. Kagan, M. Bawendi; Science **270**, 1335 (1995).

44) W. C. Chan, S. Nie; Science **281**, 2016 (1998).

45) S. J. Tans, A. R. Verschueren, C. Dekker; Nature **393**, 49 (1998).

46) Y. Li, F. Qian, J. Xiang, C. M. Lieber; Mater. Today **9**, 18 (2006).

47) C. M. Lieber, Z. L. Wang; MRS Bull. **32**, 99 (2007).

48) G.-C. Yi, C. Wang, W. I. Park; Semicond. Sci. Tech. **20**, S22 (2005).

49) D. Appell; Nature **419**, 553 (2002).

50) Z. Zhong, D. Wang, Y. Cui, M. W. Bockrath, C. M. Lieber; Science **302**, 1377 (2003).

51) C. Thelander, P. Agarwal, S. Brongersma, J. Eymery, L. Feiner, A. Forchel, M. Scheffler, W. Riess, B. Ohlsson, U. Gösele; Mater. Today **9**, 28 (2006).

52) W. Lu, C. M. Lieber; Nat. Mater. **6**, 841 (2007).

53) M. S. Gudiksen, L. J. Lauhon, J. Wang, D. C. Smith, C. M. Lieber; Nature **415**, 617 (2002).

54) W. I. Park, G. C. Yi; Adv. Mater. **16**, 87 (2004).

55) K. Tomioka, J. Motohisa, S. Hara, K. Hiruma, T. Fukui; Nano Lett. **10**, 1639 (2010).

56) B. O. Jung, D. C. Kim, B. H. Kong, D.-W. Kim, H. K. Cho; Sens. Actuators B **160**, 740 (2011).

57) Y. Cui, Q. Wei, H. Park, C. M. Lieber; Science **293**, 1289 (2001).

58) R. Colby, Z. Liang, I. H. Wildeson, D. A. Ewoldt, T. D. Sands, R. E. García, E. A. Stach; Nano Lett. **10**, 1568 (2010).

59) M. W. Larsson, J. B. Wagner, M. Wallin, P. Håkansson, L. E. Fröberg, L. Samuelson, L. R. Wallenberg; Nanotechnology **18**, 015504 (2007).

60) Y. Wu, R. Fan, P. Yang; Nano Lett. **2**, 83 (2002).

61) J. Hu, M. Ouyang, P. Yang, C. M. Lieber; Nature **399**, 48 (1999).

62) W. Liu, Y. Liang, H. Xu, L. Wang, X. Zhang, Y. Liu, S. Hark; J. Phys. Chem. C **114**, 16148 (2010).

63) C. Sun, K. Miyaji, K. Johguchi, K. Takeuchi; IEEETrans. Circuits Syst. I, Reg. Papers **61**, 382 (2014).

64) S. D. Hersee, X. Sun, X. Wang; Nano Lett. **6**, 1808 (2006).

65) M. Yoshizawa, A. Kikuchi, M. Mori, N. Fujita, K. Kishino; Jpn. J. Appl. Phys. **36**, L459 (1997).

66) T. Kuykendall, P. J. Pauzauskie, Y. Zhang, J. Goldberger, D. Sirbuly, J. Denlinger, P. Yang; Nat. Mater. **3**, 524 (2004).

Chapter 2

Experimental technique

2.1 MOCVD system (EpiQuest, SH4001-HTA)

This section describes our metalorganic chemical vapor deposition (MOCVD) equipment system and growth process used for clarification of our growth method. We used an SH4001-HTA system manufactured by EpiQuest of Japan.
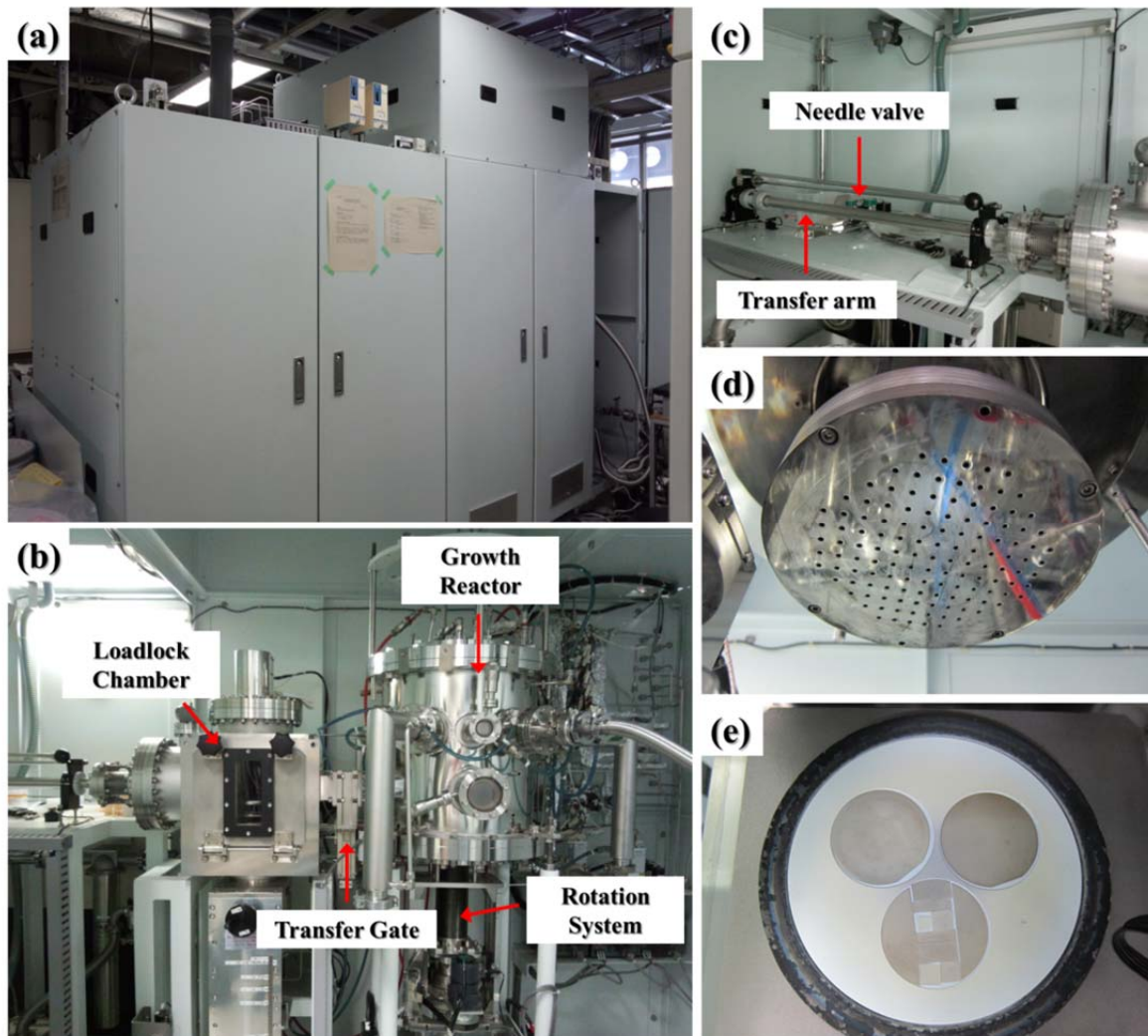
Figure 2.1 (a) SH4001-HTA (EpiQuest, Japan) MOCVD equipment. (b) and (c) indicate the detailed parts of the MOCVD system. (d) Showerhead in reactor of MOCVD system. (e) Eight-inch type susceptor.

This MOCVD system was utilized for the growth of all the III-N materials in this study including GaN templates, GaN nanorods, $In_xGa_{1-x}N$/GaN MQWs, and the *p*-GaN layer for the 3D-LED structure. The EpiQuest SH4001-HTA system is a vertical (shower-head-type) and low-rotation-speed reactor. Figure 2.2 show the detailed schematic of the SH4001-HTA MOCVD reactor. Figure 2.1 (a) – (c) show the main reactor used for material growth and the adjacent loadlock chamber, which are connected through a 6-inch gate shutter. The loadlock configuration enables samples to be moved toward the main reactor by a transfer arm and prevents reactor contamination by atmospheric particles when samples are transferred into the main chamber through the transfer gate, hence it is helpful to maintain a low oxygen (O_2) level and stable humidity in the main reactor. A schematic of the MOCVD system is shown in Fig. 2.3.
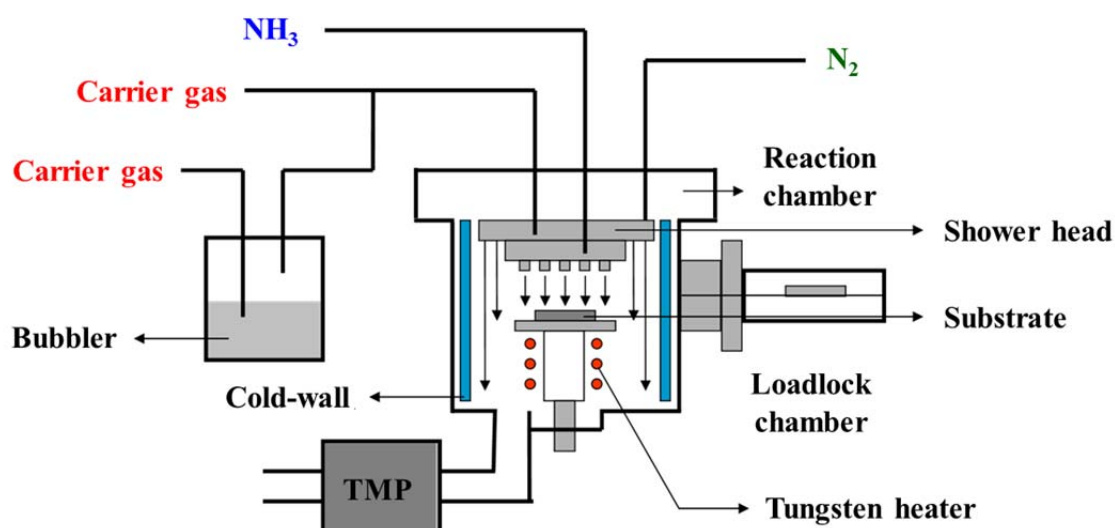
Figure 2.2 Detailed schematic of SH4001-HTA (EpiQuest, Japan) MOCVD reactor

The conditions in the MOCVD system during material growth are maintained by cooling water and circulating gaseous nitrogen (GN_2). The metalorganic (MO) sources of the group
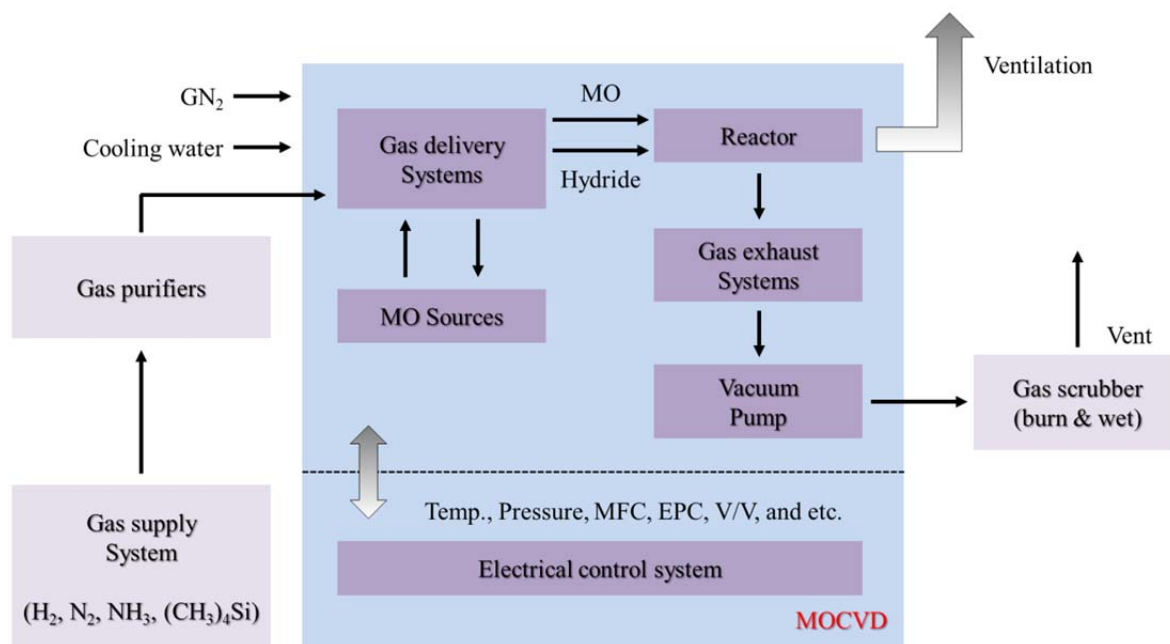
Figure 2.3 Schematic of III-nitride MOCVD system.

III materials such as TMGa, TEG, TMA, and TMI are stored in bubblers. The temperatures of the bubblers are kept at the optimal values using a water bath to maintain a stable vapor pressure. Pure hydrogen (H_2) and nitrogen (N_2) were utilized in the reactor as carrier gases after passing through gas purifiers. Ammonia (NH_3) was used as the group V source for III-N material synthesis. Cyclopentadienyl magnesium (Cp_2Mg) and tetramethylsilane (($CH_3)_4Si$) were used as *p*-type and *n*-type dopants, respectively. The utilized MO sources and hybride are transferred into a gas scrubber by the exhaust system to evacuate acidic gases. The overall control of the MOCVD system was carried out using well-established electrical components, which control the mass flow controller (MFC), electronic pressure controller (EPC) to adjust gas flow rate, pressure, temperature, vent valve (V/V), and other kinds of situations.

2.2 Chemical reaction of GaN in MOCVD

The MOCVD synthesis procedure involves the flow of gaseous precursors on a heated
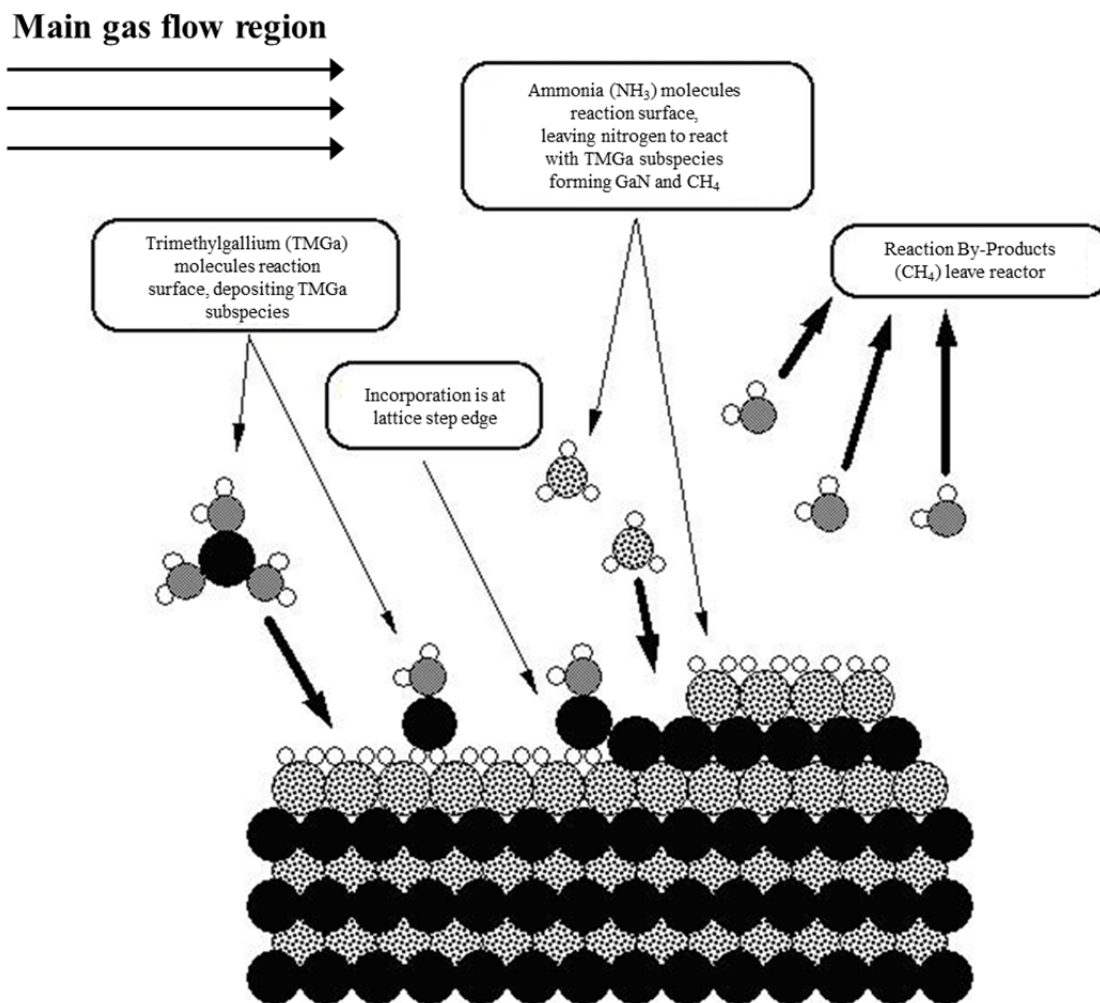
Figure 2.4 Schematic of the fundamental mass transfer and reaction process in GaN growth by MOCVD.[1]

substrate, where the reactants decompose by pyrolysis then epitaxial growth occurs. The group III reactants used, known as metal alkyls, are generally trimethylgallium (TMGa), triethylgallium (TEG), trimethylaluminum (TMA), and trimethylindium (TMI). The group V source is generally a hydride such as NH_3. The fundamental MOCVD reaction describing the GaN deposition process can be expressed as [1] :

$$Ga(CH_3)_3(v) + NH_3(v) \rightarrow GaN(s) + 3CH_4(v)$$
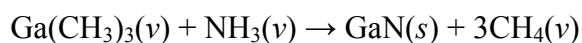
(where, v = vapor, s = solid)

This balanced expression disregards the specific reaction path and the nature of the reaction. Thus, that should make the expression more complex. Consequently, the reaction for the growth of GaN considering practical factors such as the decomposition of hydrogen bonds and the intermediate reaction of TMGa should be written as [1] :

$$GaCH_3(s/v) + NH(s/v) \rightarrow GaN(s) + 1/2H_2$$
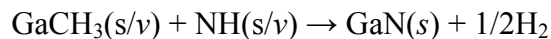
(where, v = vapor, s = solid)

When the metalorganic and hydride reactants are injected into the reactor, several processes, partly in series and partly in parallel, take place during the growth as displayed in Fig. 2.4. The reactants are mixed and transferred to the deposition area. The Ga and N molecules escape by pyrolysis owing to high growth temperature then other vapor phase reactions, thereby the precursors are formed that allow subsequent phenomena to occur on the surface such as adsorption, desorption, migration, and diffusion. The new crystalline layer is synthesized by the chemical reaction between atoms and substrate surface.[2]

2.3 Nanoimprint lithography system (SCIVAX, X-500)

This section discribes our nanoimprint equipment, which is X-500 system manufactured by SCIVAX of Japan. The approach used for position control employing the thermal nanoimprint lithography (T-NIL) technique is also explained along with the whole patterning procedure. Nanoimprint lithography patterning process was first developed by Chou in 1995 for nanoscaled patterning,[3, 4] and is now used in many application fields after his development.[5-8] The SCIVAX X-500 of thermal nanoimprint type system is utilized in the process of position control. As shown in Fig 2.6, the pattern with various aperture size of from 230 to 460 nm and pitch of from 460 to 1380 nm was used as the growth mask designs in this study and mr-I 7020E produced by *micro resist technology* of Germany was used as

main polymer for nanoimprinting. Detailed information, such as the equipment, standard pattern design, and an imprint mould image, is given in Fig. 2.5. The thermal nanoimprint lithography process consists of six procedures: (1) substrate preparation, (2) the coating of a nanoimprint polymer, (3) baking, (4) imprinting, (5) an opening process, and (6) removal of the nanoimprint polymer, in addition to reactive-ion etching (RIE) process.
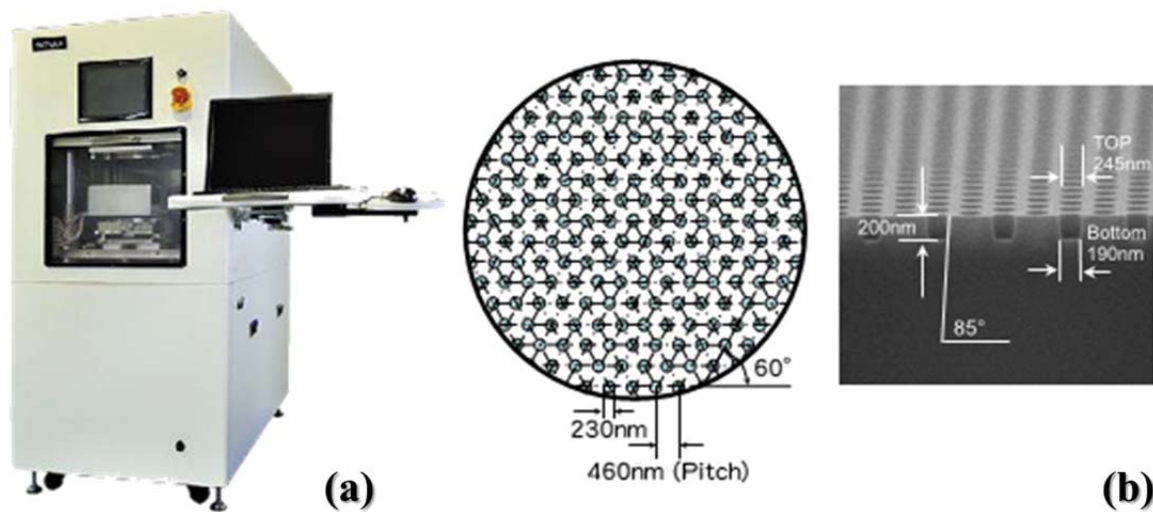
Figure 2.5 (a) Nanoimprint lithography equipment (X-500, manufactured by SCIVAX of Japan). (b) Schematic of standard pattern design and FE-SEM image of nanoimprint mould.
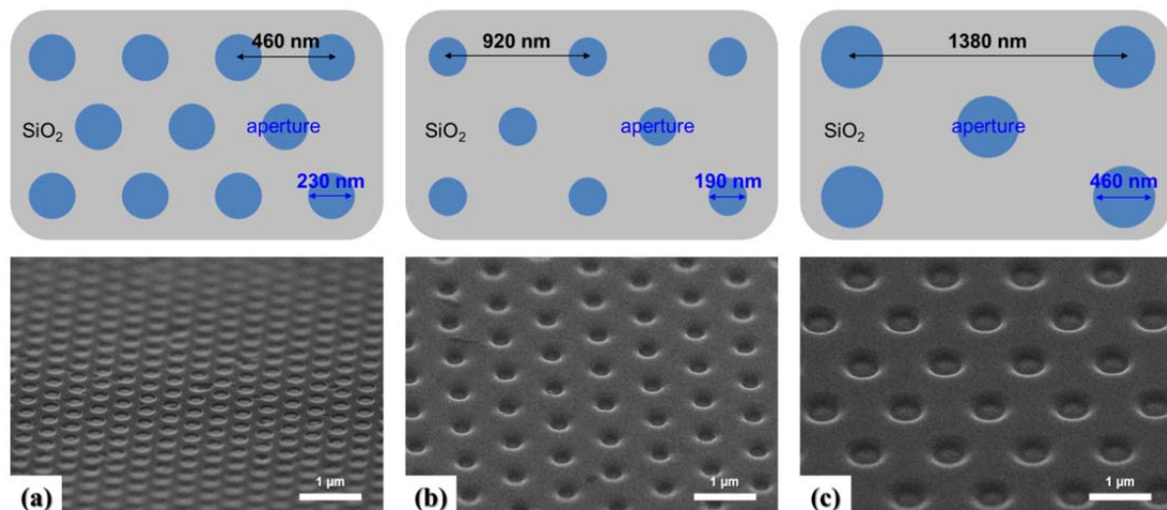
Figure 2.6 Schematic and FE-SEM images of different three types of nanoscale pattern for growth of GaN nanorods (aperture size and pitch distance, respectively). (a) 230 nm, 460 nm. (b) 190 nm, 920 nm. (c) 460 nm, 1380 nm.
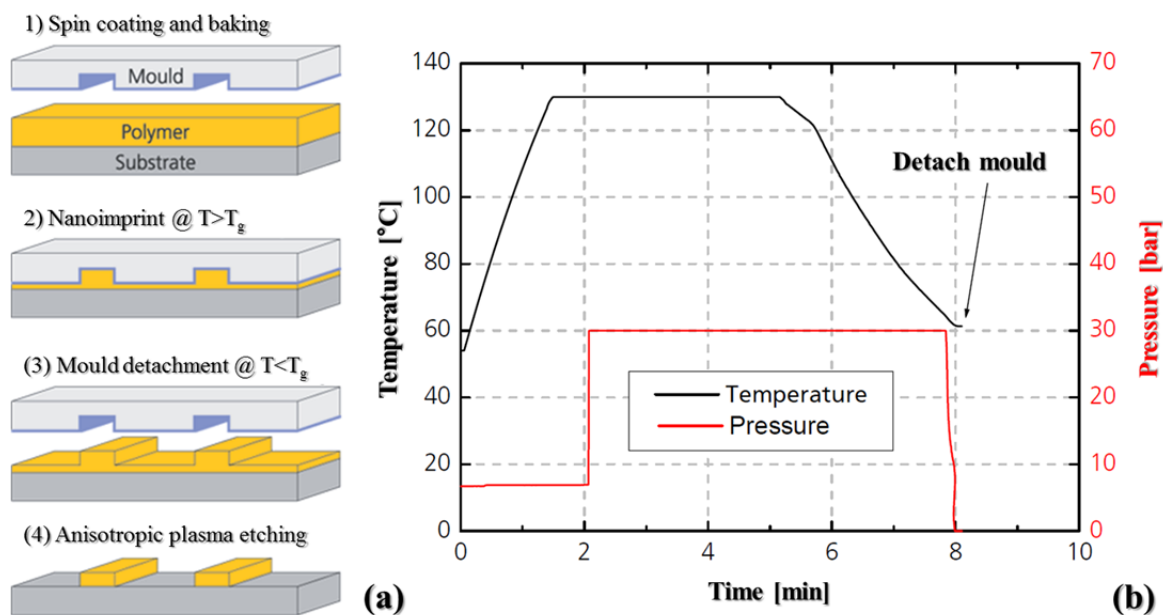
Figure 2.7 (a) Schematic of thermal nanoimprint lithography process. (b) Details of the procedure during the imprint step.

Figure 2.7 (a) displays a schematic of the whole T-NIL process. During the substrate preparation, the sample is requested to be baked at 200 °C for 30 min in a convection oven then cooled to room temperature. This is followed by the coating of the nanoimprint polymer and baking, the conventional spin coating procedure is necessary to ensure the uniformity of the polymer and the coated polymer sample is baked at 140 °C in a convection oven for 15 min. Moreover, well-established imprinting conditions are required to ensure the uniformity of the pattern, particularly the temperature, pressure, and printing time. Details of the nanoimprint procedure are shown in Fig. 2.7 (b). After the imprinting step, the CF_4 based RIE process is needed here to open the window area. Finally, an O_2 plasma process for a suitable time or organic solvents such as 1-methoxy-2-propyl acetate or acetone is performed to completely remove the residual nanoimprint polymer on the sample. This well-established nanoimprint procedure enables excellent position control in the SAG of GaN nanorod arrays.

2.4 References

1) J. Pankove, T. Moustakas, R. Willardson '*Gallium Nitride (GaN) I : Semiconductors and Semimetals'*, Academic Press: 1st Ed., Vol. 50, (1998).

2) W. Kern '*Thin film processes II'*, Academic press: 1st Ed., Vol. 2, (2012).

3) S. Y. Chou, P. R. Krauss, P. J. Renstrom; Appl. Phys. Lett. **67**, 3114 (1995).

4) S. Y. Chou, P. R. Krauss, P. J. Renstrom; J. Vac. Sci. Technol. B **14**, 4129 (1996).

5) W. Zhang, S. Y. Chou; Appl. Phys. Lett. **83**, 1632 (2003).

6) J. H. Lee, D. W. Kim, H. Jang, J. K. Choi, J. Geng, J. W. Jung, S. C. Yoon, H. T. Jung; Small **5**, 2139 (2009).

7) J.-S. Son, Y. Honda, H. Amano; Opt. Express **22**, 3585 (2014).

8) S. H. Ahn, L. J. Guo; ACS Nano **3**, 2304 (2009).

Chapter 3

Pulsed-mode MOCVD growth of GaN nanorod arrays

3.1 Background

Low-dimensional nanostructure materials such as GaN, GaAs, and ZnO have attracted great interest in the fields of electrical and optical application owing to their unique chemical and physical properties.[1-3] Among these materials, nanorods composed of GaN and related group III-V compound semiconductor materials have a huge potential for realizing revolutionary semiconductor device configurations.

The position-controlled selective growth of GaN nanorod arrays has received considerable interest over the past few years because these structures have great promise for various applications, such as light-emitting diodes (LEDs), laser diodes (LDs), optical sensors, high power transistors, and solar cells.[4-9] In particular, the controlled growth of GaN nanorods allows the possibility of pushing III-V based optoelectronic devices further towards their efficiency limits. Compared with the conventional planar structure, structures based on GaN nanorod arrays have a number of advantages. The nanorod size of less than a few hundred nm can help completely eliminate the threading dislocations formed during homoepitaxial growth.[10] Therefore, the crystal quality of GaN nanorods can be improved much higher than that of the conventional planar structure. Also, because of the small dimensions of nanorods, there is a potential of higher level of indium incorporation during $In_xGa_{1-x}N$/GaN multi-quantum-well (MQW) growth due to possibility of lateral strain relaxation on either the top or sidewall plane.[11, 12] In addition, the growth of c-axis-oriented GaN nanorods can lead to nonpolar or semipolar planes on either the sidewall or slanted plane.[1] If the shape of nanorods can be controlled, it will also be possible to expose preferred

planes (*m*- or *a*-planes) on the nanostructure, which can act as basal templates for the growth of epitaxial layers to obtain the desired functions in devices. For example, the commonly used conventional planar *c*-plane InGaN/GaN LEDs on sapphire substrates suffer from acute piezoelectric polarization due to the large lattice mismatch between GaN and InGaN, which leads to the quantum-confined Stark effect (QCSE) and results in decreased radiative recombination efficiency, as is widely known.[13] However, the exposed nonpolar planes (*m*-planes) of GaN nanorod arrays are known to eliminate piezoelectric polarization, which can dramatically reduce the QCSE in the quantum-well.[14] To grow vertically well-aligned GaN nanorod arrays, it is necessary to understand the growth mechanism of GaN nanorods in detail.

GaN nanorod arrays are typically grown by the metalorganic chemical vapor deposition (MOCVD),[1] molecular beam epitaxy (MBE),[15] and vapor-liquid-solid (VLS) growth methods.[16] In many previous studies on catalyst-free MOCVD with selective area growth (SAG), Ga-polar GaN nanorod arrays were successfully grown on a GaN template.[1] N-polar GaN nanorods also have recently been successfully grown on a GaN template by constant-mode MOCVD growth (also known as conventional-mode growth, continuous-mode growth, or the continuous flow mode).[17] However, it is well known that conventional-mode growth, in which the III and V precursors are introduced simultaneously into the reactor, generally leads to the formation of pyramid structures through the emergence of $\{1\bar{1}01\}$ semipolar planes on the GaN template.[18] The pulsed-mode MOCVD growth technique (also called the pulsed source injection mode, or source modulation mode) was first introduced in 2006 by Hersee *et al.*[1] Since then, many research groups have used this technique to successfully form GaN nanostructures as a hexagonal rod shape with $\{1\bar{1}00\}$ six *m*-planes forming the vertical sidewalls of the structures on a GaN template. The growth mechanism of N-polar

GaN nanorods under constant-mode growth has already been clarified in detail.[17] Although many studies on Ga-polar GaN nanorod growth have been carried out using the technique of Hersee *et al.*, including growth parameters such as source injection and interruption time, the growth mechanism of Ga-polar GaN nanorods under pulsed-mode MOCVD growth technique is still unknown. Growth conditions such as the role of the carrier gas, temperature, NH_3 partial pressure, nucleation dependence, and the use of a source injection or interruption step, may strongly affect the growth rates of facets and the surface morphology.

In this chapter, we report the successful selective growth of vertically well-aligned Ga-polar GaN nanorod arrays on *c*-GaN templates by pulsed-mode MOCVD technique and our investigation of their structural properties for different growth conditions. The dependence of the Ga-polar GaN nanorod arrays on growth parameters, including the initial nucleation layer dependence, growth temperature, precursor injection, and interruption duration, are presented and discussed in detail. Finally, the growth model for these vertically aligned GaN nanorod arrays is summarized briefly.

3.2 Experimental section

3.2.1 Growth procedure and approach

Table 3.1 Types of experiment carried out in this chapter with controlled growth parameters.

Exp. Set	Temp. [°C]	TMGa injection [sec]	TMGa interruption [sec]	NH_3 injection [sec]	NH_3 interruption [sec]	Controlled parameters
I	1000	5	1	10	1	Initial grwoth (filling process)
II	900 - 1025	5	1	10	1	Growth temperature
III	975	5 - 20	1 - 3	10	1	Ga injection & interruption
IV	975	5	1	10 - 40	1 - 3	NH_3 injection & interruption

Our approach to clarifying the growth mechanism of GaN nanorod arrays is shown in detail in Table 3.1. GaN templates consisting of an epitaxial layer of *c*-plane GaN grown on a sapphire substrate were prepared for nanorod arrays growth by patterning the substrate with a SiO_2 growth mask containing a hexagonal array of nanoscale openings prepared by thermal nanoimprinting and reactive-ion etching (RIE). First, a 30-nm-thick SiO_2 growth mask was deposited by RF magnetron sputtering on a 2-μm-thick undoped GaN template grown on a *c*-plane sapphire substrate. Then, SiO_2 circular aperture arrays were formed by thermal nanoimprinting. Each circular aperture had a diameter of 230 nm and the center-to-center spacing was 460 nm as shown in Fig 2.6 (a). The pattern was transferred from the resist to the SiO_2 growth mask using a CF_4-based RIE process, and the surface was then cleaned with solvents and further treated with oxygen plasma for 10 min to remove any residual resist. The SiO_2/GaN/sapphire substrate was then loaded into showerhead MOCVD equipment for GaN nanorod arrays growth. The GaN nanorod arrays were initially grown at 1000 °C at a pressure of 200 Torr. Trimethylgallium (TMGa) and ammonia (NH_3) were used as the precursors in the growth. The TMGa flow rate was maintained at 78 μmol/min (15 sccm) and the NH_3 flow rate was kept at 223.21 mmol/min (5 slm). Pure hydrogen (H_2) was used as the carrier gas.
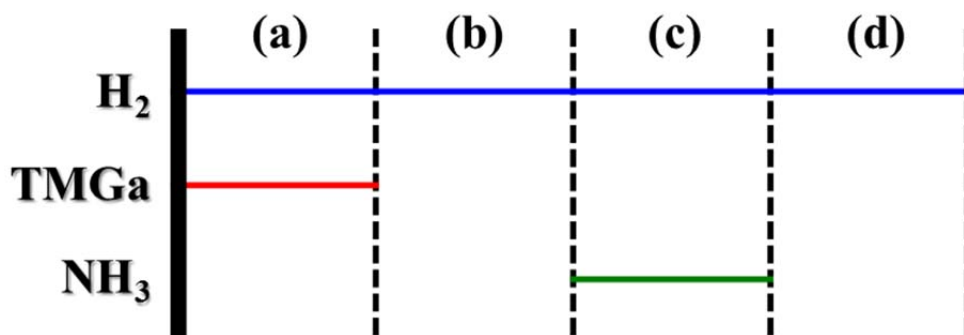

Figure 3.1 Schematic diagram of steps in each cycle in pulsed-mode MOCVD growth. (a) TMGa injection, (b) TMGa interruption, (c) NH_3 injection, and (d) NH_3 interruption steps.

TMGa and NH_3 were introduced into reactor separately with the H_2 carrier gas during the each injection steps. During both the TMGa and NH_3 interruption steps, only the H_2 carrier gas was introduced into the MOCVD chamber. The optimized pulsed-mode growth cycle consists of (a) a TMGa injection step (5 sec), (b) a TMGa interruption step (1 sec), (c) an NH_3 injection step (10 sec), and (d) an NH_3 interruption step (1 sec) as schematically shown in Fig. 3.1. Also, we defined the value of pulsed-mode growth ratio (PMGR) as sources injection ratio divided by sources interruption ratio. The injection ratio means N injection time divided by Ga injection time and interruption ratio means N interruption time divided by Ga interruption time. For example, our optimized PMGR value is 2 during growth.

$$PMGR = \left[\frac{(N\ injection\ time \div Ga\ injection\ time)}{(N\ interruption\ time \div Ga\ interruption\ time)} \right] \qquad (1)$$

The pulsed-growth cycles of between 10 and 30 were applied in the experiments and a nucleation step (namely, a *filling process*) was performed in some experiments.

3.2.2 Characterization tools

The morphology of the GaN nanorod arrays was observed by field-emission scanning electron microscopy (FE-SEM, S-5200) at an operation voltage of 5 kV. The microstructural characterization of GaN nanorods was carried out by transmission electron microscopy (TEM, JEM-2100F) operated at 200 kV. The convergent-beam electron diffraction (CBED) patterns were recorded in CBD mode while controlling the condenser aperture and electron-beam angle.[19] To prepare TEM specimens for the electron incidence condition of $[1\bar{1}00]$ zone-axis, the GaN nanorods were thinned using a focused ion beam system (FIB, SII Xvision 200DB) which includes a FE-SEM. The photoluminescence (PL) measurements of the GaN nanorod

arrays were carried out at room-temperature using a He-Cd laser operating at 325 nm.

3.3 Growth of GaN nanorod arrays by pulsed-mode MOCVD procedure

3.3.1 Effect of initial growth (filling process)

In the case of pulsed-mode MOCVD approach, the source modulation injection technique, including the source interruption duration, appears to be a critical factor in GaN nanorod arrays growth. This will be discussed later in this paper. However, the nucleation layer dependence of the GaN nanorod morphology or shape development requires further research because the effect of nucleation is still unclear in GaN nanorod arrays growth. To investigate this effect, we prepared experiments involving a filling process and non-involving. According to Hersee's original process,[1] the filling process is inserted before pulsed-mode growth procedure for brief intervals. During the filling process, TMGa and NH_3 were introduced simultaneously into the reactor as the III, and V precursors, respectively, and the objective of the filling process was to initiate uniform GaN growth inside all the growth mask apertures. Fig. 3.2 (a) shows only the nanosize hole pattern on the GaN template with the SiO_2 growth mask. In contrast, Fig. 3.2 (e) shows the slightly filled hole pattern after the filling process. The number of pulsed-mode growth cycles was applied to investigate the effect of the filling process. After the cycles of pulsed-mode growth, the surface morphology was completely different. A pyramidal structure emerged as the dominant shape after a few pulsed growth cycles in the case of no filling process, as shown in Figs. 3.2 (b) – (c). However, when the filling process was carried out, the $\{1\bar{1}00\}$ m-plane sidewalls based hexagonal rod structure emerged with small (0001) c-plane area on top of the GaN nanorods as shown in Figs. 3.2 (f) – (g). The dominance of the semipolar planes in the initial stage for each sample has normally been ascribed to the slow growth rate of the $\{1\bar{1}01\}$ semipolar

planes resulting from the hydrogen passivation effect. Li *et al*. reported about this phenomenon with the results discussed.[20]
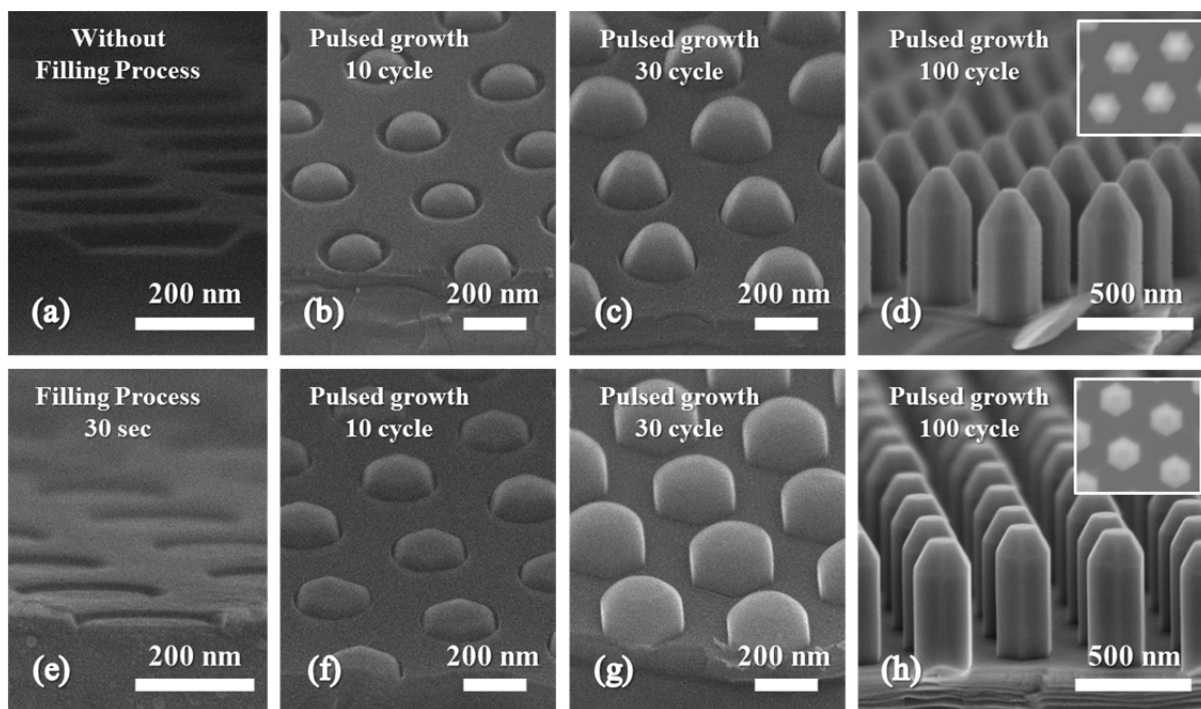
Figure 3.2. Cross-sectional SEM images of GaN nanorod arrays samples at each stage. (a) − (d) results of pulsed-mode growth without filling process. (e) − (h) results of pulsed-mode growth including 30 sec filling process.

After the pulsed-mode growth process, each GaN nanorod had a perfectly defined symmetric hexagonal rod structure comprising six nonpolar *m*-planes. However, the topmost shape in the two arrays is clearly different. This indicates that the nucleation layer in the initial stage has a strong effect on the shape at the top of the GaN nanorods. The pulsed-mode growth procedure increases the growth rate along the (0001) direction but suppress the growth rate in the *m*-plane direction. Therefore, the shape of the top of the GaN nanorods depends on the initial shape of the nucleate and can have different morphologies after pulsed-mode growth as shown in Fig. 3.3. However, we believe that the filling process isn't the decided factor

determining success or failure of GaN nanorod arrays growth. We consider that the shape of the top of the GaN nanorods can affect the light emission after $In_xGa_{1-x}N/GaN$ MQWs growth in core-shell structure. This will be discussed in a next chapter.
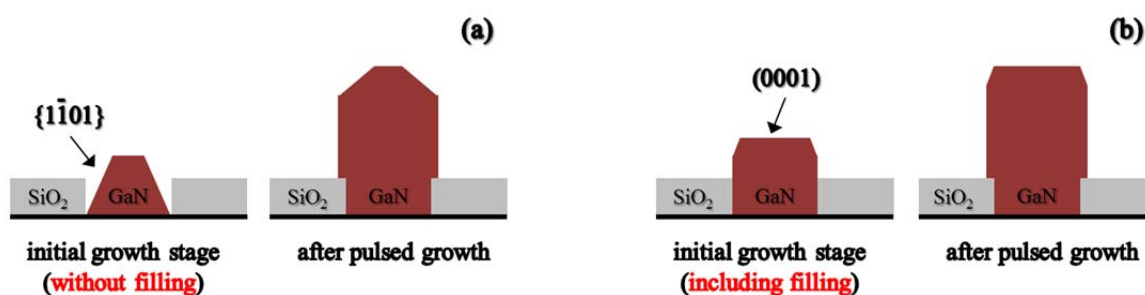
Figure 3.3 Schematic diagram for pulsed-mode growth of GaN nanorod (a) involving and (b) not involving a filling process.

3.3.2 Effect of growth temperature

The growth temperature can be considered to be a crucial factor in the growth of GaN nanorod arrays. To determine the effects of the N and Ga kinetics and precursor diffusion behavior, we prepared GaN nanorod arrays at growth temperatures from 900 to 1025 °C (thermocouple reading in the susceptor) at intervals of 25 °C, with the TMGa and NH_3 flow rates kept at 15 sccm and 5 slm, respectively, without the filling process.

The graph in Fig. 3.4 (a) shows the height and width of the nanorods as functions of the growth temperature. At the low temperature of 900 °C, the surface morphology had an almost continuous merged structure. However, the surface morphology markedly changed from 950 °C as shown in Figs. 3.4 (c) – (e). In other words, a higher growth temperature led to a higher vertical-to-lateral aspect ratio of the GaN nanorods, i.e., the height increased, while the width decreased. Li *et al*. reported that a higher growth temperature leads to the enhanced
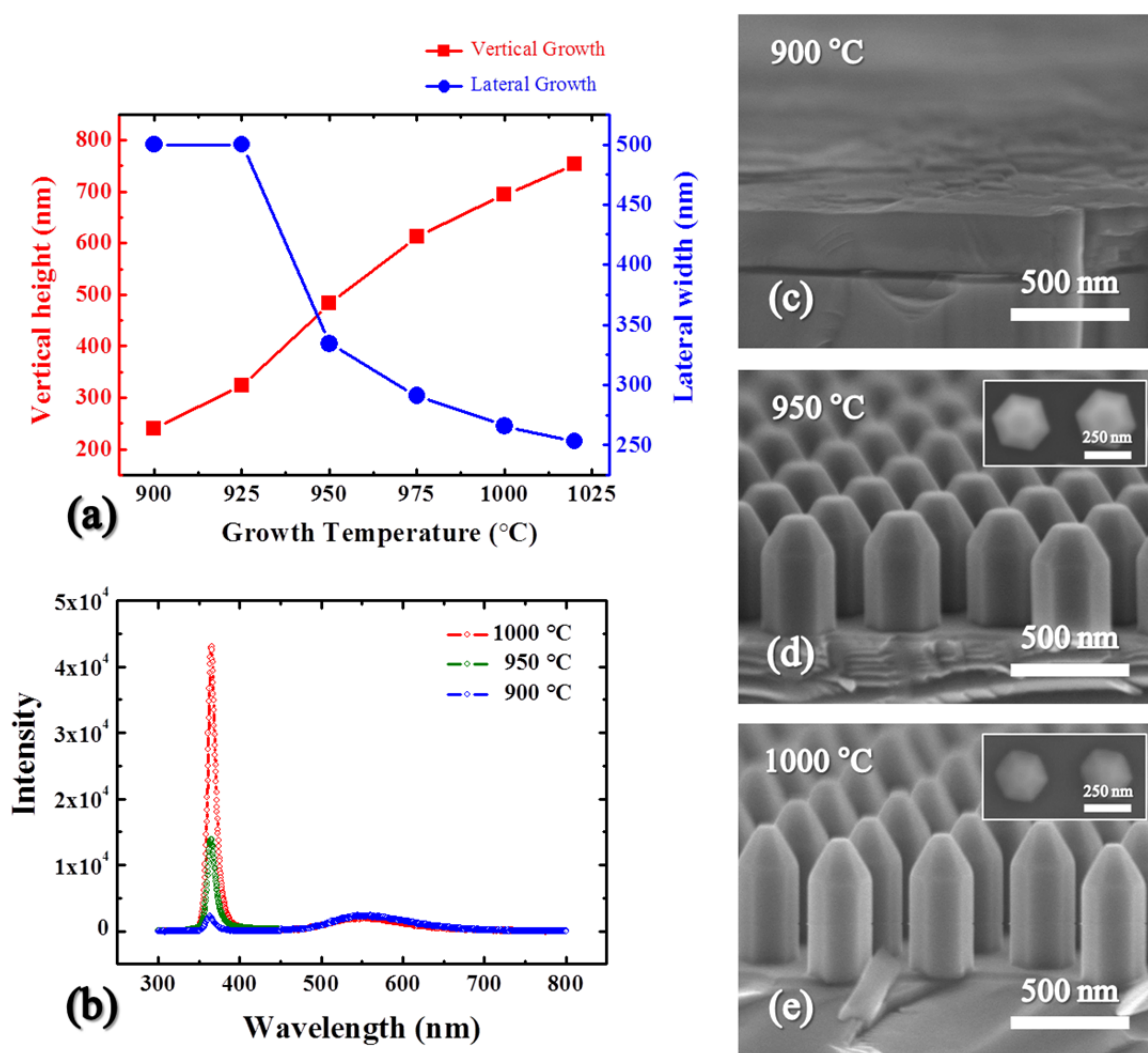
Figure 3.4 (a) Graph showing height (*c*-plane) and width (*m*-plane) of GaN nanorods as functions of the growth temperature. (b) the room temperature PL spectra of the GaN nanorod arrays according to different growth temperatures. Cross-sectional SEM images showing morphology of GaN nanorod arrays grown at temperatures of (c) 900 °C, (d) 950 °C, and (e) 1000 °C. The insets of (d) and (e) are plan-view SEM images of GaN nanorod arrays.

surface diffusion of Ga adatoms, which leads to the increased height and aspect ratio of the nanorods.[17] And also, according to a previous result, the Ga desorption rates have different value from *c*- and *m*-plane of GaN.[21] According to their results, the desorption rate of Ga adatoms from the *c*-plane is four times lower than that from the *m*-plane. When the growth

temperature was increased, the desorption rate of Ga adatoms from both the *m*- and *c*-planes was also increased, resulting in the accelerated desorption of Ga adatoms. However, the sticking coefficient of Ga adatoms on the *c*-plane is typically higher (> 0.77) than that on the *m*-plane (< 0.77).[22] The diffused Ga adatoms from the *m*-plane to the *c*-plane dwell on *c*-plane for a longer time. Hence, the Ga adatoms on the *c*-plane can surmount the effect of the increased desorption rate. Consequently, the vertical growth is enhanced and the lateral growth is suppressed.

The optical properties of the GaN nanorod arrays under various growth temperatures were investigated by PL spectroscopy at room temperature as shown in Fig. 3.4 (b). Irrespective of the growth temperature, a strong near-band-edge (NBE) emission is observed at around 364 nm from GaN nanorod arrays. According to growth temperature, much of the UV emission intensity increase is undoubtedly due to the geometry of a GaN nanorod arrays, indicating high optical quality and crystallinity of the GaN nanorods. And also, we consistently observe visible yellow emission in the GaN nanorod arrays samples. Many hypotheses have proposed about the origin of yellow emission.[23-25] However, we consider that the yellow emission comes from the GaN basal template in the case of GaN nanorods.[1]

3.3.3 Confirmation of polarity

GaN layer grown via MOCVD generally displays polarity along the c-axis direction due to the lack of inversion symmetry in III-N wurtzite lattice. The polarity has various developments on the chemical and physical characteristics of the respective orientation. Especially, it can influence the surface chemical reactivity during GaN growth such as dopant or impurity incorporation.[26, 27] To determine the polarity of GaN nanorods, we performed CBED analysis under [1$\bar{1}$00] zone-axis. Theoretical CBED patterns were calculated using a

many-beam dynamical calculations and least-squares fitting (MBFIT) program based on the Bloch-wave dynamical theory of electron diffraction.[28] Bright-field TEM image of sectioned GaN nanorods is shown in Fig. 3.5 (a).
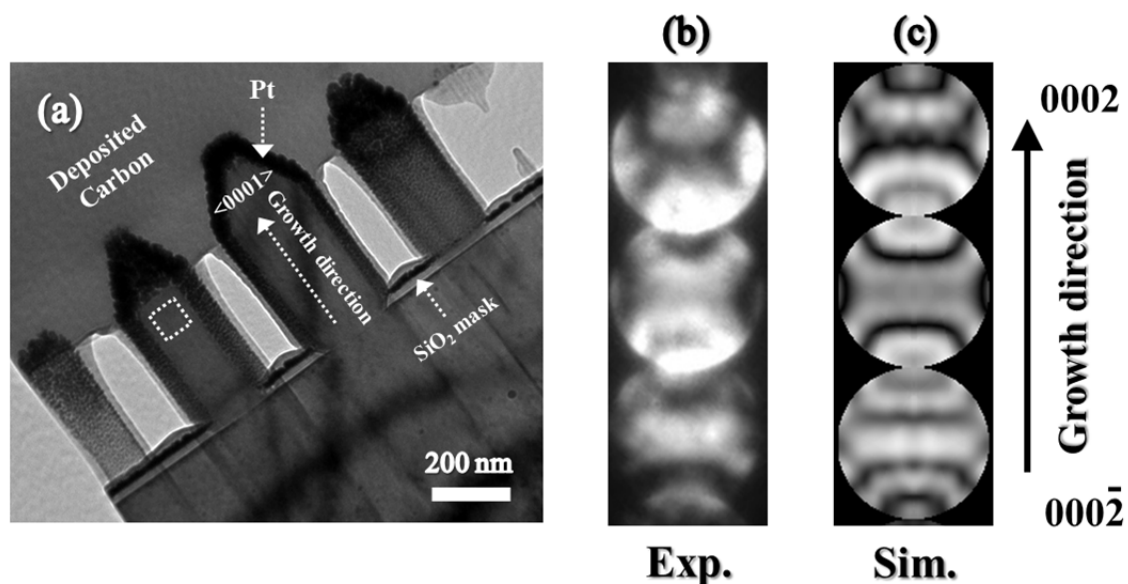
Figure 3.5 (a) Cross-sectional TEM images of the GaN nanorods used to obtain the CBED patterns for polarity determination. (Color online) [1$\bar{1}$00] zone-axis CBED. (b) experimental and (c) simulated patterns of GaN nanorods (d = 95 nm thick).

The surfaces of the GaN nanorods were covered with a Pt/carbon layer to protect them from damage by the FIB. Fig. 3.5 (b) shows experimentally observed CBED patterns of GaN nanorod with 95-nm-thick detection region. On the center of images, a dark band was shown in 0002 disk, while a white band was observed between two dark bands in the 000$\bar{2}$ disk. These patterns really confirm the Ga-polarity along the growth direction from base to top in GaN nanorod.[29] More vivid CBED patterns were obtained using the Bloch-wave simulations for the same thickness of experimentally detected region, as shown in Fig. 3.5 (c), indicating well matched patterns with experiments.

3.3.4 Effect of TMGa injection and interruption durations

The TMGa injection time was found to be another important parameter in GaN nanorod arrays growth, because if the TMGa injection time is changed, the growth rate of various facets is also changed under pulsed-mode MOCVD growth. To investigate the change in the GaN nanorod arrays morphology with the TMGa injection time, an experiment was performed at 975 °C with various TMGa injection times without the filling process. The results are shown in Fig. 3.6 for injection times of (a) 5 sec, (b) 10 sec, and (c) 20 sec. The NH_3 injection time was maintained at 10 sec, and the Ga and N interruption times were kept at 1 sec. It can be seen that, the surface structure showed the typical nanorod arrays morphology and the value of PMGR is maintained at 2 under the optimized TMGa injection time. When the TMGa injection time was increased from 5 to 10 sec, strong lateral growth occurred along the *m*-planes and the value of PMGR is reduced to as 1. When the TMGa injection time was further increased to 20 sec, the nanorod morphology was markedly changed from nanorods to a thin film and the value of PMGR is reduced to as 0.5 again. This result is similar to pulsed lateral overgrown (PLOG) GaN behavior.[30] In our pulsed-mode MOCVD, we consider that the migration of Ga adatoms primarily controls the growth rate of each facet and the GaN nanorod volume in each aperture. According to previous result, a high density of Ga species in the mask region leads to a higher rate of growth in the lateral direction under pulsed-mode growth.[30] Under a Ga-rich "injection or interruption" condition, Ga diffuses from the surface to the growth mask region. If the TMGa injection time increases, the number of migrated Ga species in the growth mask region is also increased. Thus, this allows a higher growth rate along the lateral direction. To achieve the nanorod morphology and prevent growth in the lateral direction, it is necessary for the value of PMGR to be maintained above 1 by adjustment of TMGa injection time in pulsed-mode MOCVD procedure.
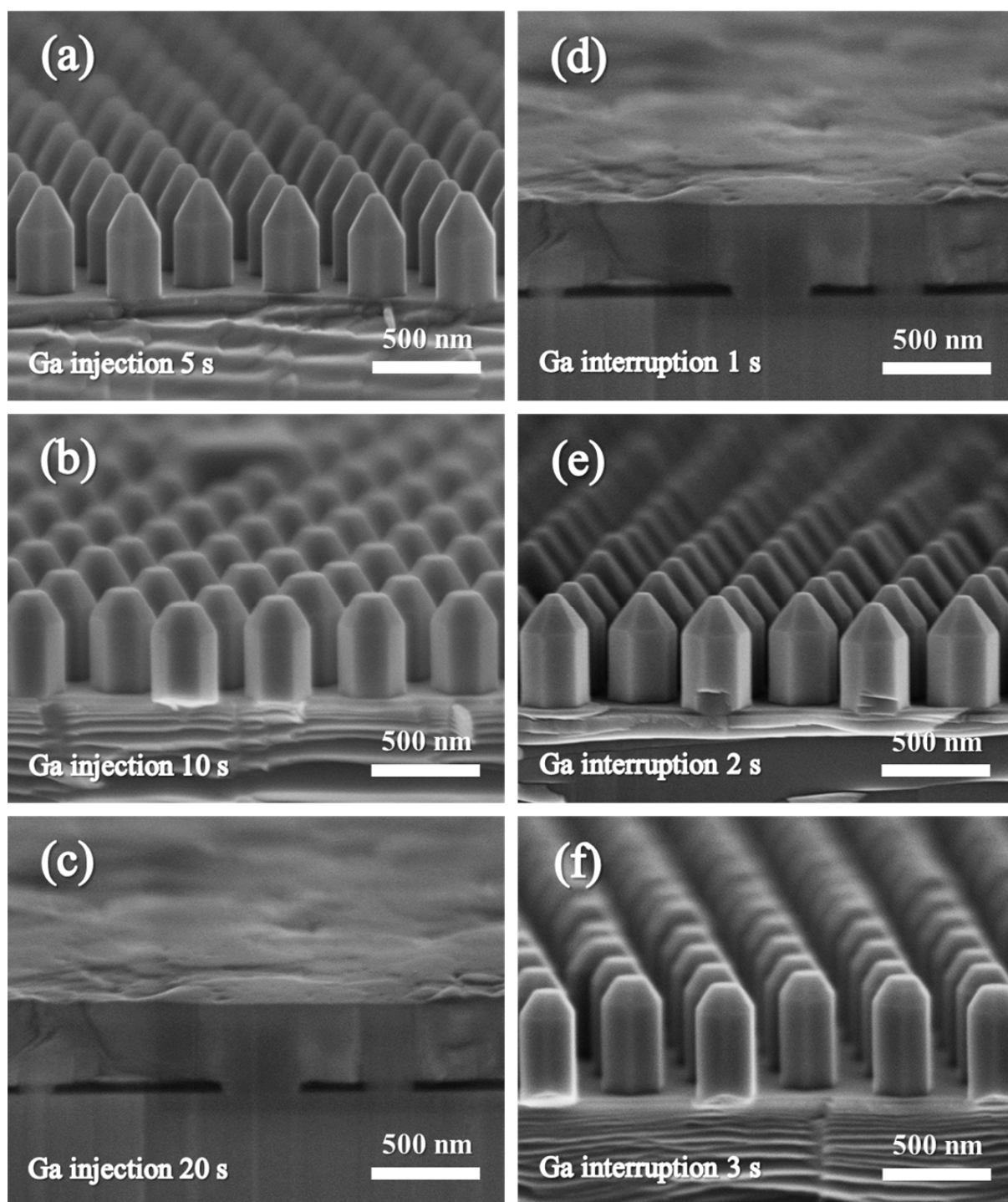
Figure 3.6 Cross-sectional SEM images of GaN nanorod arrays with TMGa injection times of (a) 5 s, (b) 10 s, and (c) 20 s. Effect of TMGa interruption time on the morphology of GaN nanorod arrays: (d) 1 s, (e) 2 s, and (f) 3 s.
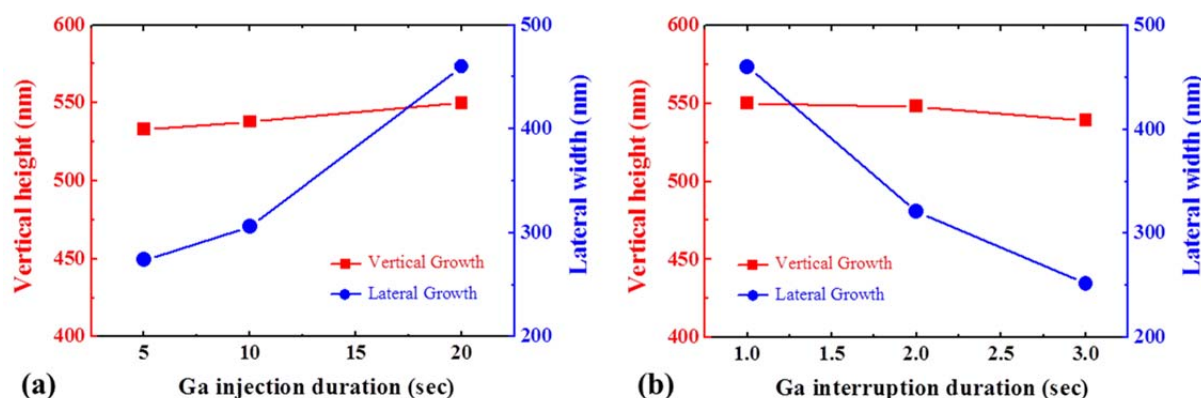
Figure 3.7 Vertical and lateral growth as function of Ga injection and interruption duration

We carried out one more experiment to determine the effect of the Ga interruption time. In this experiment, only the TMGa interruption time was varied from 1 to 3 sec. The NH_3 and TMGa injection times were maintained at 10 sec and 20 sec, respectively, and the N interruption time was kept at 1 sec. As seen in Figs. 3.6 (d) – (f), in the case of the longer TMGa injection duration as 20 sec, the GaN nanorod arrays were formed by adjustment of TMGa interruption time and the value of PMGR is maintained at 1, and 1.5, respectively. It means that if the PMGR has a value above 1, the surface morphology has nanorod geometry as the dominant shape. Also, hydrogen thermal etching appeared to occur on top of the GaN nanorods for an even longer interruption duration (not shown). The change in the surface morphology from a thin film to nanorods is evidence of an increase in the desorption rate of Ga adatoms on the *m*-plane.[31] If TMGa interruption time is increased, Ga on the surface can be redistributed during the TMGa interruption period. In our case, during the longer TMGa interruption period, the desorption of Ga adatoms began to occur on both the *m*- and *c*-planes. The desorption rate on the *m*-plane was higher than that from the *c*-plane owing to the lower sticking coefficient of Ga on the *m*-plane. This led to the prevention of growth in the lateral direction. However, the desorption of Ga adatoms on the *c*-plane can overcome the increased desorption rate owing to the higher sticking coefficient. In addition, Ga adatoms can be

resupplied to the surfaces by residual TMGa in the reactor from the previous injection cycle, which leads to the maintenance of the vertical growth rate. As a result, the net vertical growth rate is preserved and the lateral growth rate is suppressed. Therefore, the optimal interruption time is necessary for maintaining the value of PMGR above 1 and achieving a nanorod morphology under longer TMGa injection duration because the nanorod arrays morphology is mainly determined by the adsorption/desorption behavior of Ga adatoms on each facet.

3.3.5 Effect of NH$_3$ injection and interruption durations

The following experiment was carried out to investigate the effects of the N injection and interruption times on the surface morphology of GaN nanorod arrays. To study the transition of GaN nanorod arrays, GaN nanorods were grown at 975 °C with various NH$_3$ injection times from 10 to 40 sec without the filling process. The morphologies of the GaN nanorod arrays are shown in Fig. 3.8 for N injection durations of (a) 10 sec, (b) 20 sec, and (c) 40 sec. The TMGa injection time was maintained at 5 sec and the G and N interruption times were maintained at 1 sec. To investigate the effect of the N injection time, we increased the NH$_3$ injection time from 10 to 20 sec. As the NH$_3$ injection time increased, growth along the [1$\bar{1}$01] direction was slightly suppressed while growth on the *m*-plane direction was little enhanced. However, the morphology of the nanorod arrays still maintained their dominant structure. When the NH$_3$ injection time was longer than 20 sec, the morphology of the nanorod arrays markedly evolved from nanorods to pyramidal shapes and the value of PMGR is changed to as 8. It is similar to the typical morphology obtained by constant-mode growth of GaN SAG.[18] This experiment indicated that an appropriate NH$_3$ injection duration is an important factor in obtaining GaN nanorod arrays under pulsed-mode growth. If the NH$_3$ injection time is increased without changing the interruption time, the result of pulsed-mode
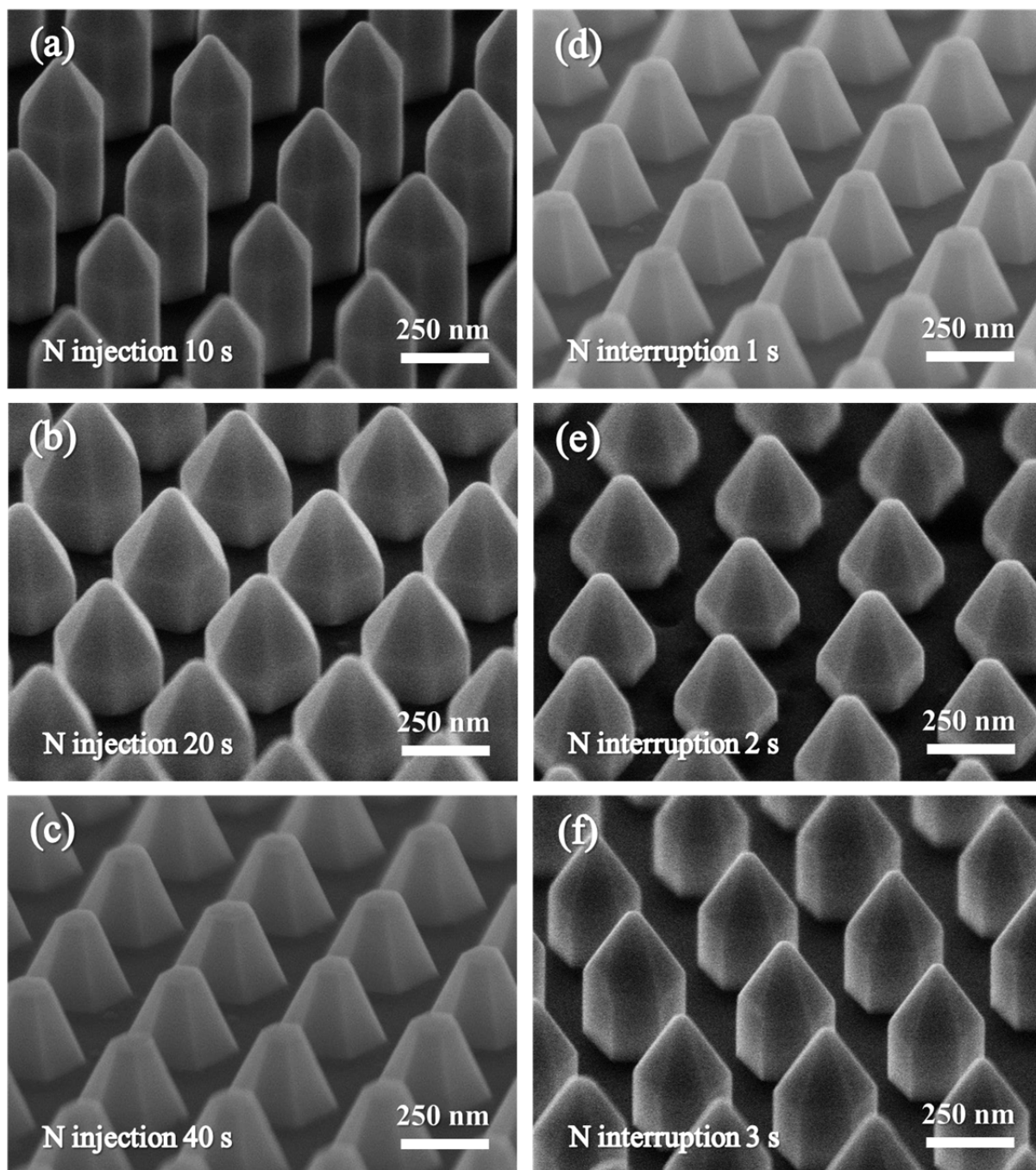
Figure 3.8 Cross-sectional SEM images of GaN nanorod arrays with NH_3 injection times of (a) 10 s, (b) 20 s, and (c) 40 s. Effect of NH_3 interruption time on the morphology of GaN nanorod arrays: (d) 1 s, (e) 2 s, and (f) 3 s.

growth changes as if constant-mode growth does owing to overlap of Ga and N adatoms. Generally, the pyramidal structure is related to the low growth rate of the $\{1\bar{1}01\}$ semipolar plane. Chen *et al.* previously reported that the growth rate of possible low index planes can be represented by a kinetic Wulff plot.[32] The plot indicates that the $\{1\bar{1}01\}$ semipolar planes of GaN have the slowest growth rate under constant-mode growth, which leads to the growth of hexagonal pyramids due to the hydrogen passivation effect.[20] Also, according to the Wulff growth theory,[33] the low-growth-rate planes remain after growth, which leads to the pyramidal structure. In the MOCVD growth ambient, there are a large number of hydrogen atoms obtaining from the decomposition of NH_3, the carrier gas, and other sources. If the NH_3 injection time is increased, the number of hydrogen atoms from the decomposed NH_3 also increases. Thus, we consider that if hydrogen is abundant during growth, the N-terminated facets of $\{1\bar{1}01\}$ are passivated by hydrogen, leading to stable $\{1\bar{1}01\}$ planes.[34] Hence, these $\{1\bar{1}01\}$ planes have very low growth rates during Ga-polar GaN nanorod growth. Consequently, the GaN nanorods have the pyramidal shape as the dominant morphology.
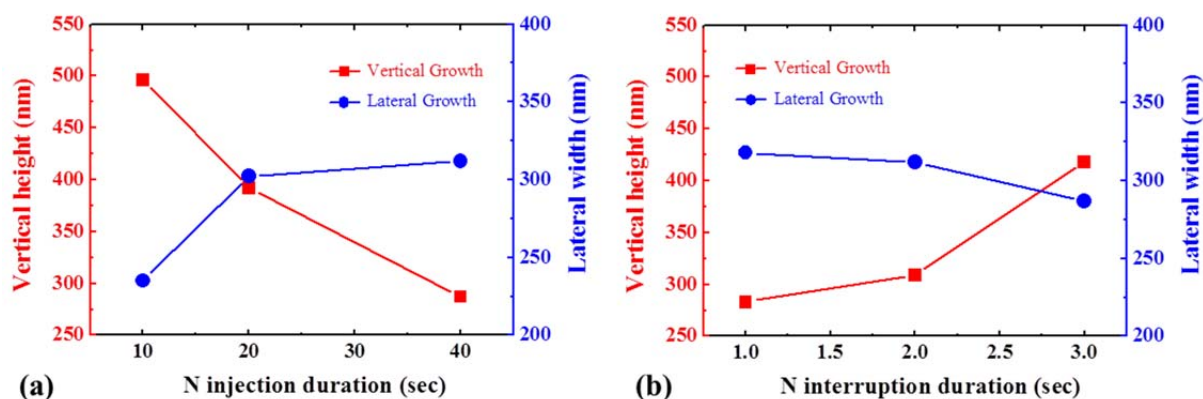
Figure 3.9 Vertical and lateral growth as function of N injection and interruption duration

To determine the effect of the N interruption time, we performed another experiment in which the NH_3 interruption time was varied from 1 to 3 sec. The NH_3 and TMGa injection times were maintained at 40 sec and 5 sec, respectively, and the Ga interruption time was kept at 1 sec. As seen in Figs. 3.8 (d) – (f), the GaN nanorod arrays were changed by control of NH_3 interruption time under longer NH_3 injection duration as 40 sec. The value of PMGR is maintained at 4, and 2.6, respectively, by NH_3 interruption time. It means that if the PMGR has a value below 4, the surface morphology has nanorod geometry as the dominant shape. Hydrogen thermal etching was also observed on top of the GaN nanorods for an even longer interruption duration similar to the case of a longer TMGa interruption duration (not shown). It is well known that H_2 carrier gas can etch GaN structures via N-H and Ga-H formation at high temperatures.[35, 36] Thus, the optimal interruption time is essential to prevent hydrogen thermal etching. In addition, the change in the surface morphology from pyramidal structure to nanorods indicates that the role of N interruption is to prevent the overlapping supply of Ga and N through the removal of residual N atoms.[31] Excepting the hydrogen thermal etching effect, if the pulsed-mode growth does not have a sufficient interruption duration in the case of the oversupply of NH_3 injection duration, the growth results of pulsed-mode growth will be changed as constant-mode growth owing to the overlap with N and Ga adatoms.[31] Actually, the key concept of pulsed-mode growth is to enhance the diffusion of group III species by reducing the V/III ratio. Ideally, during pulsed-mode growth, the V/III ratio is maintained at 0 under a Ga-rich condition (injection and interruption). In contrast, under a N-rich condition (injection and interruption), the V/III ratio should be kept at infinity. To maintain these V/III ratios, the precursors must be completely separated during each step. Therefore, to prevent the overlap of precursors and maintain the value of PMGR below 4, the optimal N interruption duration is required under pulsed-mode growth.

3.4 Growth model of GaN nanorod arrays by pulsed-mode MOCVD procedure

3.4.1 Growth model of GaN nanorods following TMGa steps

In the Ga injection step, TMGa is injected inside the reactor. The atomic Ga formed from the homogeneous decomposition of TMGa diffuses from the surface to the growth mask region,[37] then is adsorbed on all the exposed planes during this step. If the TMGa injection time exceeds the optimal value (it means that the value of PMGR is reduced below 1), lateral growth will be non-negligible owing to the high density of Ga adatoms in the growth mask region as shown in Fig. 3.10 (a). Consequently, an appropriate injection duration (it means that the PMGR should have a value above 1) can suppress growth along the m-plane direction.
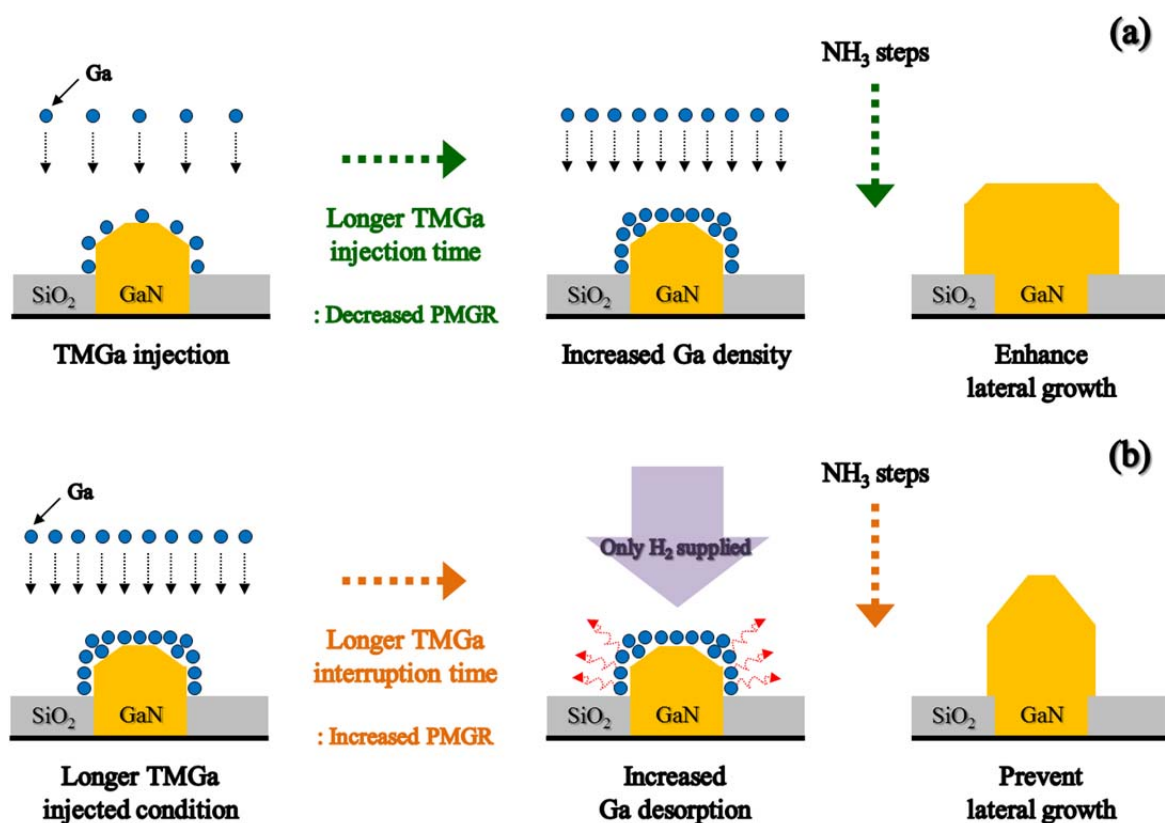
Figure 3.10. Schematic growth model of GaN nanorod following TMGa steps. (a) Longer TMGa injection period. (b) Longer TMGa interruption duration under prolonged TMGa injection duration.

During the Ga interruption step, Ga adatoms already absorbed on the *m*-plane from the previous TMGa injection step can desorb from the *m*-plane, but the Ga adatoms on the *c*-plane have a longer lifetime during the interruption step, which is related to the different sticking coefficients on various GaN facets.[38] Also, the Ga adatoms are expected to be resupplied to the surface by residual TMGa in the reactor. If a suitable TMGa interruption duration is applied (it means that the PMGR should have a value above 1) under longer TMGa injection duration, lateral growth can be prevented by the selective desorption of Ga adatoms on the *m*-plane as shown in Fig. 3.10 (b). To achieve the nanorod shape, the Ga interruption period should be applied with suitable value depending on the Ga injection time.

3.4.2 Growth model of GaN nanorods following NH_3 steps

In the N injection step, NH_3 is thought to decompose heterogeneously on the surface or to reactor walls to yield atomic nitrogen or nitrogen-containing radicals.[39] The N atoms arrive at the Ga adatoms remaining on the surface from the previous step. This N injection step induces the growth of GaN. If the NH_3 injection time is too long (it means that the value of PMGR is increased to 8), the injected precursors can be overlap during each source injection step due to residual N atoms as shown in Fig. 3.11 (a). In the case of a longer NH_3 injection time, pulsed-mode growth is changed as constant-mode growth. Hence, the pulsed-mode growth characteristics are lost. If an appropriate NH_3 injection duration is applied (if the PMGR has a value below 4), the surface can avoid the result similar to constant mode growth. As a result, the GaN nanorods can achieve the nanorod geometry.

During the N interruption period, the residual N is washed or evacuated from the surface by the carrier gas.[31] Depending on the NH_3 injection time, the surface morphology can be changed between nanorods and pyramidal shapes. Under a longer NH_3 injection period, the high partial pressure of NH_3 can lead to typical GaN crystal growth. If a suitable N
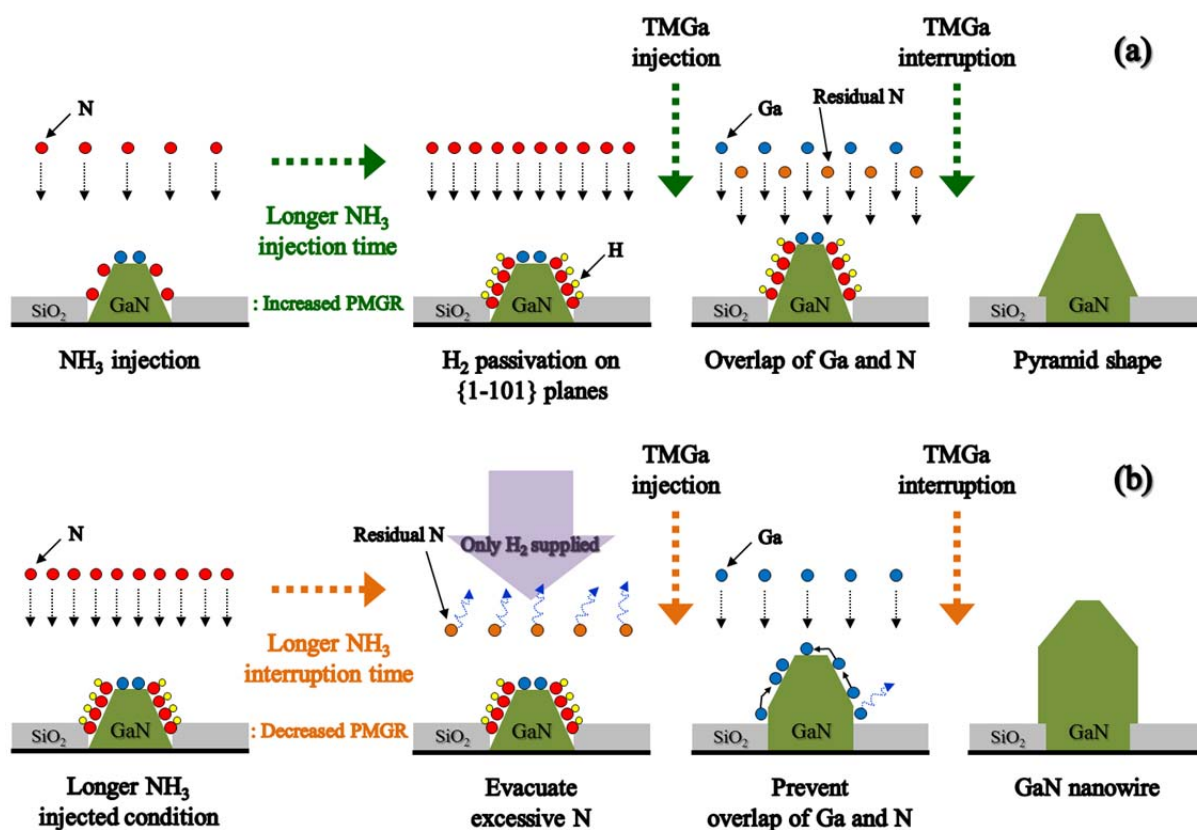
Figure 3.11 Schematic growth model of GaN nanorod following NH_3 steps. (a) Longer NH_3 injection period. (b) Longer NH_3 interruption duration under prolonged NH_3 injection duration.

interruption duration is applied following NH_3 injection time (if the value of PMGR is decreased less than 4), it can prevent from change that pulsed-mode growth is turned as constant-mode growth. Therefore, an appropriate N interruption time is required to flush out the N remaining in the reactor from the previous injection step to achieve GaN nanorod arrays growth as shown in Fig. 3.11 (b).

3.5.Summary

● In this chapter, a scalable process was investigated for the synthesis of selectively grown GaN nanorod arrays under pulsed-mode MOCVD growth. Each experiment indicated the formation mechanism of GaN nanorod arrays by showing the dependence of the behavior of Ga and N adatoms on different growth parameters.

● The different shapes of the initial nucleation layers depending on whether or not a filling process was carried out affected the shape of the top of the GaN nanorods after pulsed-mode growth.

● The GaN morphology was controlled by the growth temperature, and the precursor injection and interruption durations. The maintenance of the vertical growth rate and the suppression of the lateral growth rate are necessary for the growth of GaN nanorod arrays.

● A higher growth temperature affects the surface reaction of Ga adatoms, indicating that the growth of GaN nanorod arrays is mainly determined by the kinetic behavior of Ga adatoms.

● A longer TMGa injection duration allows a higher growth rate along the lateral direction. In addition, a longer NH_3 injection period leads to hexagonal pyramidal shape due to overlap with N and Ga adatoms.

● Nevertheless, the morphology of GaN nanorod arrays can be controlled by applying an appropriate interruption duration with longer precursor injection times. Consequently, the surface morphology has nanorod geometry as the dominant shape when the value of PMGR has between 1 and 4. To achieve the GaN nanorod morphology, suitable precursor injection and interruption periods must be applied in pulsed-mode MOCVD growth.

● The realization of GaN nanorod arrays promises to be beneficial for the fabrication of large-scale integrated optoelectronic devices using nanomaterials.

3.6 References

1)   S. D. Hersee, X. Sun, X. Wang; Nano Lett. **6**, 1808 (2006).

2)   A. I. Persson, M. W. Larsson, S. Stenström, B. J. Ohlsson, L. Samuelson, L. R. Wallenberg; Nat. Mater. **3**, 677 (2004).

3)   B. O. Jung, D. C. Kim, B. H. Kong, D. W. Kim, H. K. Cho; Sens. Actuators B **160**, 740 (2011).

4)   Y. J. Hong, C.-H. Lee, A. Yoon, M. Kim, H.-K. Seong, H. J. Chung, C. Sone, Y. J. Park, G.-C. Yi; Adv. Mater. **23**, 3284 (2011).

5)   J. C. Johnson, H. J. Choi, K. P. Knutsen, R. D. Schaller, P. D. Yang, R. J. Saykally; Nat. Mater. **1**, 106 (2002).

6)   J.-W. Lee, K.-J. Moon, M.-H. Ham, J.-M. Myoung; Solid State Commun. **148**, 194 (2008).

7)   C.-P. Chen, A. Ganguly, C.-Y. Lu, T.-Y. Chen, C.-C. Kuo, R.-S. Chen, W.-H. Tu, W. B. Fischer, K.-H. Chen, L.-C. Chen; Anal. Chem. **83**, 1938 (2011).

8)   Y. Huang, X. F. Duan, Y. Cui, C. M. Lieber; Nano Lett. **2**, 101 (2002).

9)   Y. Dong, B. Tian, T. J. Kempa, C. M. Lieber; Nano Lett. **9**, 2183 (2009).

10)   R. Colby, Z. Liang, I. H. Wildeson, D. A. Ewoldt, T. D. Sands, R. E. Garcia, E. A. Stach; Nano Lett. **10**, 1568 (2010).

11)   C.-F. Huang, T.-Y. Tang, J.-J. Huang, W.-Y. Shiao, C. C. Yang, C.-W. Hsu, L. C. Chen; Appl. Phys. Lett. **89**, 051913 (2006).

12)   C.-H. Liao, W.-M. Chang, H.-S. Chen, C.-Y. Chen, Y.-F. Yao, H.-T. Chen, C.-Y. Su, S.-Y. Ting, Y.-W. Kiang, C. Yang; Opt. Express **20**, 15859 (2012).

13)   T. Takeuchi, S. Sota, M. Katsuragawa, M. Komori, H. Takeuchi, H. Amano, I. Akasaki; Jpn. J. Appl. Phys. **36**, L382 (1997).

14)   M. C. Schmidt, K.-C. Kim, H. Sato, N. Fellows, H. Masui, S. Nakamura, S. P. DenBaars, J. S. Speck; Jpn. J. Appl. Phys. **46**, L126 (2007).

15)   H. Sekiguchi, K. Kishino, A. Kikuchi; Appl. Phys. Express **1**, 124002 (2008).

16)   F. Qian, Y. Li, S. Gradecak, D. L. Wang, C. J. Barrelet, C. M. Lieber; Nano Lett. **4**, 1975 (2004).

17)   S. Li, X. Wang, M. S. Mohajerani, S. Fuendling, M. Erenburg, J. Wei, H.-H. Wehmann, A. Waag, M. Mandl, W. Bergbauer, M. Strassburg; J. Cryst. Growth **364**, 149 (2013).

18)   S. Kitamura, K. Hiramatsu, N. Sawaki; Jpn. J. Appl. Phys. **34**, L1184 (1995).

19)   M. Imura, U. Gautam, K. Nakajima, Y. Koide, H. Amano, K. Tsuda; Jpn. J. Appl. Phys. **52**, 08JE15 (2013).

20)   S. F. Li, S. Fuendling, X. Wang, S. Merzsch, M. A. M. Al-Suleiman, J. D. Wei, H. H. Wehmann, A. Waag, W. Bergbauer, M. Strassburg; Cryst. Growth Des. **11**, 1573 (2011).

21)   S. Choi, T.-H. Kim, H. O. Everitt, A. Brown, M. Losurdo, G. Brun, A. Moto; J. Vac. Sci. Technol. B **25**, 969 (2007).

22)   A. Smith, R. Feenstra, D. Greve, J. Neugebauer, J. Northrup; Appl. Phys. A **66**, S947 (1998).

23)   D. M. Hofmann, D. Kovalev, G. Steude, B. K. Meyer, A. Hoffmann, L. Eckey, R. Heitz, T. Detchprom, H. Amano, I. Akasaki; Phys. Rev. B **52**, 16702 (1995).

24)   M. A. Reshchikov, H. Morkoc; J. Appl. Phys. **97**, 061301 (2005).

25)   J. Neugebauer, C. G. VandeWalle; Appl. Phys. Lett. **69**, 503 (1996).

26)   N. Fichtenbaum, T. Mates, S. Keller, S. DenBaars, U. Mishra; J. Cryst. Growth **310**, 1124 (2008).

27)   L. K. Li, M. Jurkovic, W. Wang, J. Van Hove, P. Chow; Appl. Phys. Lett. **76**, 1740 (2000).

28)   K. Tsuda, M. Tanaka; Acta Crystallographica Section A: Foundations of

Crystallography **51**, 7 (1995).

29)   A. Urban, J. Malindretos, J. Klein-Wiele, P. Simon, A. Rizzi; New J. Phys. **15**, 053045 (2013).

30)   R. Qhalid Fareed, J. Yang, J. Zhang, V. Adivarahan, V. Chaturvedi, M. Asif Khan; Appl. Phys. Lett. **77**, 2343 (2000).

31)   Y.-T. Lin, T.-W. Yeh, P. D. Dapkus; Nanotechnology **23**, 465601 (2012).

32)   X. J. Chen, G. Perillat-Merceroz, D. Sam-Giao, C. Durand, J. Eymery; Appl. Phys. Lett. **97**, 151909 (2010).

33)   A. A. Kelly, K. M. Knowles '*Crystallography and crystal defects'*, John Wiley & Sons, Inc.: 2nd Ed., (2012).

34)   J. E. Northrup, J. Neugebauer; Appl. Phys. Lett. **85**, 3429 (2004).

35)   A. Koukitu, M. Mayumi, Y. Kumagai; J. Cryst. Growth **246**, 230 (2002).

36)   E. Yakovlev, R. Talalaev, A. Segal, A. Lobanova, W. Lundin, E. Zavarin, M. Sinitsyn, A. Tsatsulnikov, A. Nikolaev; J. Cryst. Growth **310**, 4862 (2008).

37)   A. Thon, T. F. Kuech; Appl. Phys. Lett. **69**, 55 (1996).

38)   K. A. Bertness, A. Roshko, L. M. Mansfield, T. E. Harvey, N. A. Sanford; J. Cryst. Growth **300**, 94 (2007).

39)   D. Ehrentraut, E. Meissner, M. Bockowski '*Technology of gallium nitride crystal growth'*, Springer: 1st Ed., Vol. 133, (2010).

Chapter 4

Selective area growth (SAG) of GaN nanorod arrays under optimal growth conditions

4.1 Background

One-dimensional (1D) building blocks structure (including nanorods, nanowires, nanocolumns, and nanocylinders) of semiconductor nanowires are of great interest in the field of optoelectronic devices, particularly for their application to light-emitting diodes (LEDs), laser didoes (LDs), photovoltaics (PV), and electro-optical sensors.[1-4] Considerable effort is being made to improve the output performance of electro-optical devices based on such building blocks in the field of compound semiconductors III-nitride or functional oxide materials including homoepitaxial and heteroepitaxial growth. Several approaches have already achieved highly ordered and well-aligned arrays of nanoscale building blocks by metal-catalyst-based vapor-liquid-solid (VLS) growth, inductively coupled plasma (ICP) dry etching, and chemical vapor phase etching (CVE) technique.[5-7] Although, these approaches have the definite advantage of easily accessible for building architecture geometries however, the utilization of metal catalysts generally debased device the output gain. This is due to the low crystallinity resulting from contaminants, which can also lead to the undesirable doping of semiconductor nanowires and thermally activated nonradiative recombination centers.[8] In addition, the top-down etching also has some problems such as surface damage, undefined crystal planes, the impossibility of position control, crystal quality, uniformity, and contamination. To realize precise position-controlled, vertically well-defined, and easily synthesized building block architecture arrays, the catalyst-free scalable process combined with bottom-up selective area growth (SAG) technique under optimal growth conditions is

absolutely necessary. This will lead to improved device performance in the field of optoelectronic applications.[1, 3] Here, this chapter will report the accurate position-controlled SAG of highly ordered, vertically defined gallium nitride (GaN) building block arrays by catalyst-free metalorganic chemical vapor deposition (MOCVD).

Typically, catalyst-free MOCVD has been performed for the SAG of GaN nanorod arrays as well as two-dimensional (2D) GaN planar structures with outstanding crystallinity and optical properties. Furthermore, catalyst-free selective-area-grown GaN nanorod arrays have indicated possibility of realization for many nanoscale-based optoelectronic device applications with distinctive characteristics. Hong *et al.* have realized on embedded nano-LED with an InGaN/GaN multiple-quantum-well (MQW) core-shell structure based on GaN nanorod arrays with various color emission properties.[1] In addition, Durand *et al.* have demonstrated a GaN-nanorod-based InAlN/GaN MQW structure with GaN $\{1\bar{1}00\}$ *m*-plane sidewalls and high-efficiency ultraviolet (UV) emission.[9] Thus, many studies are proving that GaN nanorod arrays have numerous advantages and can be used in powerful optoelectronic devices. However, these superior properties based on GaN nanorods can only be realized under optimized growth conditions. First of all, irrespective of the growth conditions, in the SAG of the MOCVD GaN nanorod arrays and is based on MQWs coaxial structures, the most common way is conventional growth technique so-called 'constant-mode'. Many studies have introduced various growth techniques for the catalyst-free, bottom-up growth of GaN nanorods. For example, an extremely low ammonia (NH$_3$) flow rate is required to synthesize of Ga-polar GaN nanowire arrays.[10] In addition, a carrier gas comprising a mixture of hydrogen (H$_2$) and nitrogen (N$_2$) with an appropriate ratio combined with a nitridation technique is desireable for the growth of N-polar GaN nanowire arrays.[11, 12] In the other interesting growth technique, there is precursor modulation MOCVD growth

procedure so-called 'pulsed-mode'.[13] The most important factors in the case of pulsed MOCVD are the injection and interruption durations of the group III and V precursors. Depending on the injection and interruption steps, the surface morphology can be changed from a three-dimensional (3D) geometry to a 2D planar structure with different exposed crystal facets of wurtzite GaN.[14, 15] Regardless of growth technique, previous research reported the effect of growth parameters for self-assembled synthesization of GaN nanowires.[16] Although many studies have demonstrated the growth of GaN nanorod arrays, a correlation of growth parameters with suitable guideline for perspective of optimizing growth condition is still far from complete, particularly in the case of pulsed MOCVD procedure. Furthermore, the influence of individual or independent growth parameters, such as temperature, reactor pressure, V/III ratio, and others have been studied for catalyst-free MOCVD growth. However the compositive influence of the growth parameters for GaN nanorod arrays has still not been reported as representative research or guideline; example of such parameters are intimate relation between the temperatures and the reactants density on the surface, the duration of precursors injection and V/III ratio, the influence of the design of dielectric growth mask, and dominant transfer mechanism of vapor phase or surface migration. Moreover, the variation of the structural and optical properties with the growth variables has not yet been reported.

Table 4.1 Details of experimental sets I, II, III, and IV.

Exp. Set	Temp. [°C]	Pattern pitch [nm]	TMGa flow [μmol/min]	NH$_3$ [slm]	Growth cycles	NH$_3$ injection [sec]	Controlled parameters
I	800 - 900	460	7.5 - 26		100	20	TMGa flow rate & temp.
II	950 - 1030	460 - 1380	78	5	150	10	Design of pattern
III	1000	460	78		50 - 300	10	Pulsed-growth cycles
IV	1030	920	78		300	10 - 20	NH$_3$ injection duration

Therefore, this chapter is investigated position-controlled, well-defined, and selectively grown GaN nanorod arrays under various conditions by pulsed-mode MOCVD procedure to establish the optimal growth conditions for GaN nanorod arrays. The strategies employed in this chapter are shown in Table 4.1.

4.2 Experimental section

4.2.1 Process of position control

We used a 2.0-μm-thick (0002) prefer entirely oriented Si-doped GaN epilayer on a 1.0-μm-thickness undoped GaN epitaxial structure with a low temperature buffer layer on a *c*-plane sapphire substrate.[17, 18] For SAG, a 30-nm-thick SiO_2 dielectric layer was deposited on a thick GaN template by radio frequency (RF) magnetron sputtering as a growth mask. A nanoscale array of apertures with a hexagonal arrangement was formed by thermal nanoimprint lithography (T-NIL) technique. In the sets of experiments Table 4.1, the aperture pitch was varied from 460 to 1380 nm with a 230 nm pitch. Then, the patterned SiO_2 was etched by CF_4-based reactive-ion etching (RIE) process to define the positions of the GaN nanorod arrays. After the dry etching process, the template was treated by an organic solvent to completely eliminate the residual NIL polymer on the surface.

4.2.2 MOCVD epitaxial growth procedure

For the SAG of GaN nanorod arrays, the patterned template was transferred into a showerhead-type MOCVD reactor (EpiQuest, SH4001-HTA). Trimethylgallium (TMGa) and NH_3 were utilized as the growth reactants with H_2 as the carrier gas. We carried out pulsed MOCVD growth procedure under optimized growth conditions that enable the position-controlled, selective, and uniform growth of GaN nanorod arrays. The pulsed-mode procedure is composed of (1) Ga injection, (2) Ga interruption, (3) N injection, and (4) N

interruption steps with suitable timing. The single pulsed-growth cycle is made up of these four pulsed steps. Details of this pulsed-mode procedure have already been given previous chapter.[15] Appropriate initial Ga and N flow rates are those for c-plane GaN synthesis under typical conditions. However, the TMGa flow rate was varied from 7.5 to 78 μmol/min to vary the V/III ratio, and the growth temperature was also controlled between 800 and 1030 °C under a reactor pressure of 200 Torr pressure for the optimization of the GaN nanorod growth conditions. The mentioned V/III ratio for pulsed MOCVD procedure in this chapter was defined as the N/Ga molar ratio within a single pulsed-growth cycle. The NH_3 flow rate was fixed at 223.21 mmol/min in all experiments. The number of pulsed-growth cycles was 50 to 300 depending on the experimental set. To establish optimal growth conditions for the synthesis of GaN nanorod arrays, the growth parameters investigated in the experimental sets are shown in Table 4.1.

4.2.3 Structural and optical characterizations

Field-emission scanning electron microscopy (FE-SEM, S-5200) was employed to examine the surface evolution of GaN nanorod arrays The microstructural characterization of the GaN nanorods was performed by high-resolution (HR) imaging, and bright-field (BF) imaging, and crystallographic analysis was performed by convergent-beam electron diffraction (CBED). Selected-area diffraction patterns (SADPs) of GaN nanorods were ontained by Cs-corrected scanning transmission electron microscopy (Cs-corrected STEM, JEM-ARM200F) with different zone-axis at an acceleration voltage of 200 kV. For TEM investigation, samples were milled by a dual-beam focused ion beam (DB-FIB, NOVA200) operated in the range of 5–30 kV. The optical properties of GaN nanorod arrays, especially their yellow luminescence (YL) were obtained by room-temperature photoluminescence (PL) measurement using a He-Cd laser operating at 325 nm.

4.3 Growth of GaN nanorod arrays with various growth conditions

4.3.1 Influence of low growth temperature with TMGa flow rate

Experimental set I was devised to optimize the growth conditions at a relatively low temperature by varying the TMGa flow rate in the SAG of GaN nanorods since suitable temperature and TMGa flow rate may be essential factors determining the 3D geometry of GaN nanorods. Figure 4.1 displays FE-SEM images of GaN nanorods grown with different temperatures and TMGa flow rates.
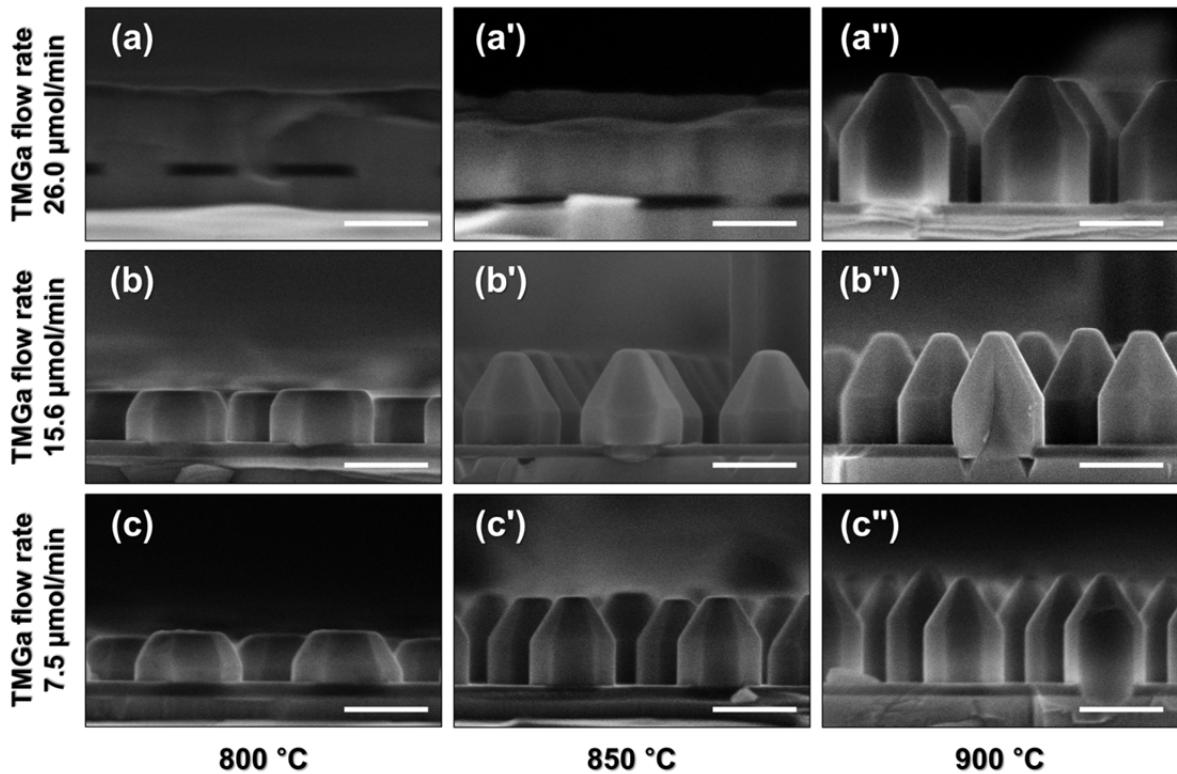
Figure 4.1. Cross-sectional FE-SEM images of selective-area-grown GaN nanorods fabricated by pulsed-mode MOCVD procedure with different growth temperatures and TMGa flow rates. (a) – (a") GaN nanorods grown with high TMGa flow rate. (b) – (b") GaN nanorods grown with medium TMGa flow rate. (c) – (c") GaN nanorods grown with low TMGa flow rate. The scale bars are 500 nm in all the FE-SEM imges.
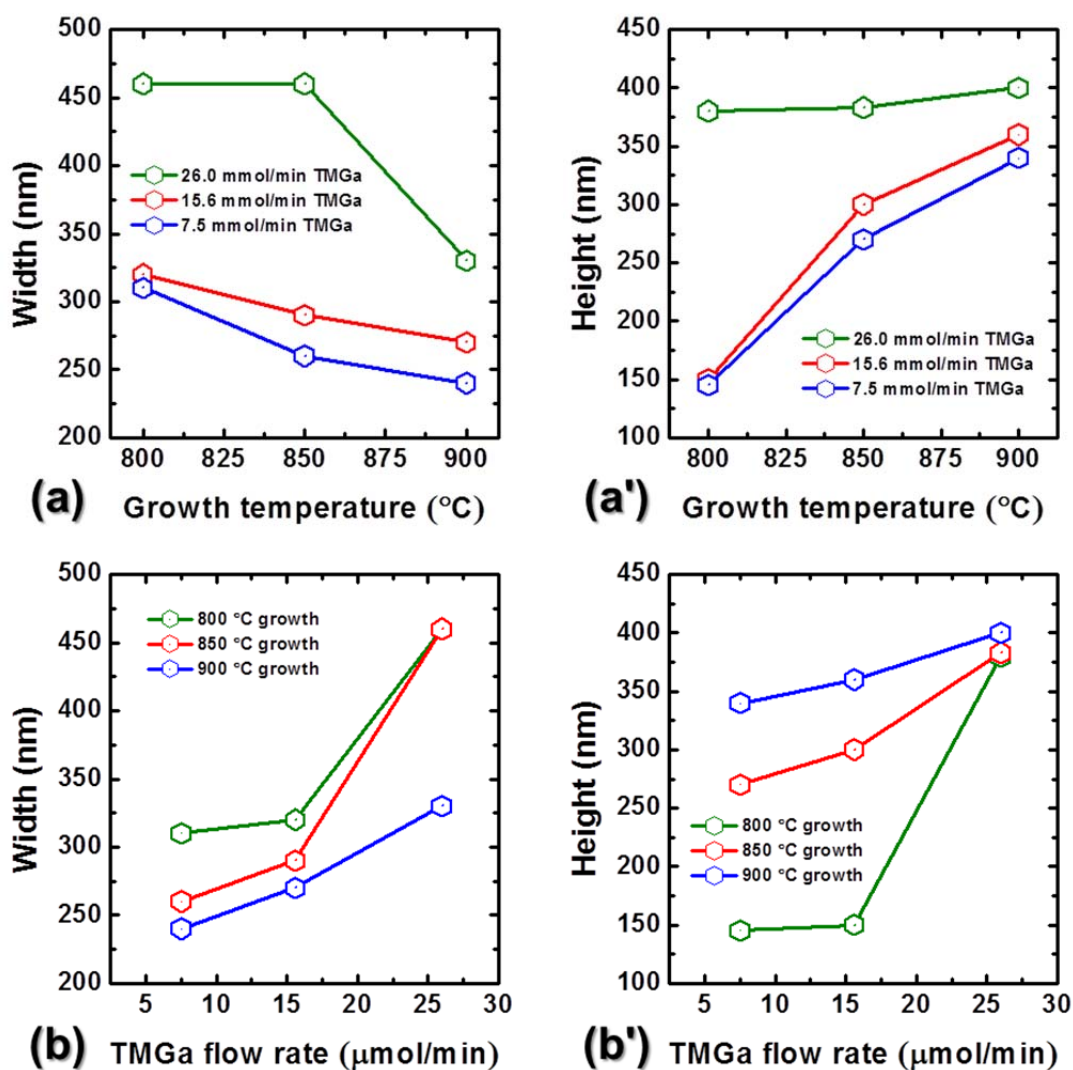
Figure 4.2. Statistical plot of height and diameter of GaN nanorods against growth temperautre and TMGa flow rate. (a) and (a') Width and height as functions of growth temperature for various TMGa flow rates, respectively. (b) and (b') Width and height as functions of TMGa flow rate for various growth temperatures, respectively.

Under these growth conditions, the shape of the GaN structure was substantial changed from a thin-film to rod shape. With increasing growth temperature, vertical growth appears to be prompted and lateral growth is suppressed, regardless of the TMGa flow rate. On the other hand, both the vertical and lateral growth rates are enhanced by increasing the TMGa flow

rate at all growth temperature range. To investigate the growth phenomena of GaN nanorods, we plotted the lateral width and vertical height of the nanorods as functions of temperature and TMGa flow rate as shown in Fig. 4.2. The height markedly increases with the growth rate at relatively low TMGa flow rates (7.5 − 15.6 µmol/min) by increasing growth temperature but, the variation of the height at a high TMGa flow rate (26.0 µmol/min) is not substantial as shown in Fig. 4.2 (a'). On the other hand, the lateral width shows the opposite trend with increasing growth temperature as shown in Fig. 4.2 (a). In addition, a gradual change in the lateral and vertical growth behaviors can be confirmed by controlling the TMGa flow rate as shown in Fig. 4.2 (b) and (b'). Overall, the TMGa flow rate and growth temperature appear to produce similar influences on the vertical growth rate of GaN nanorod. However, a different phenomenon was observed for lateral growth within range of growth variable with a forming of sixfold hexagonal rod shape. Consequently, the variation of the aspect ratio of the grown GaN nanorods shows similar but not identical behaviors as functions of the temperature and TMGa flow rate. We consider that the growth of GaN nanorods may be affected by the combined effects of adsorption, desorption, growth ambient, V/III ratio, and the density of reactants on surface.[19, 20] We will discuss these phenomena from the perspective of the optimum growth conditions at the discussion section of this chapter.

4.3.2 Influence of high growth temperature with design of growth mask

We successfully demonstrated the optimal growth conditions of GaN nanorods within low temperature range in previous section. Even so, it is an undeniable fact that a relatively high temperature (GaN crystal growth is typically carried out at approximately 1000 °C) is better than a low temperature for all aspects such as crystallinity and optical quality. In addition, we consider that a high temperature makes it easier to optimize the TMGa flow rate owing to the effective suppression of the lateral growth as shown in Fig. 4.3 FE-SEM images.
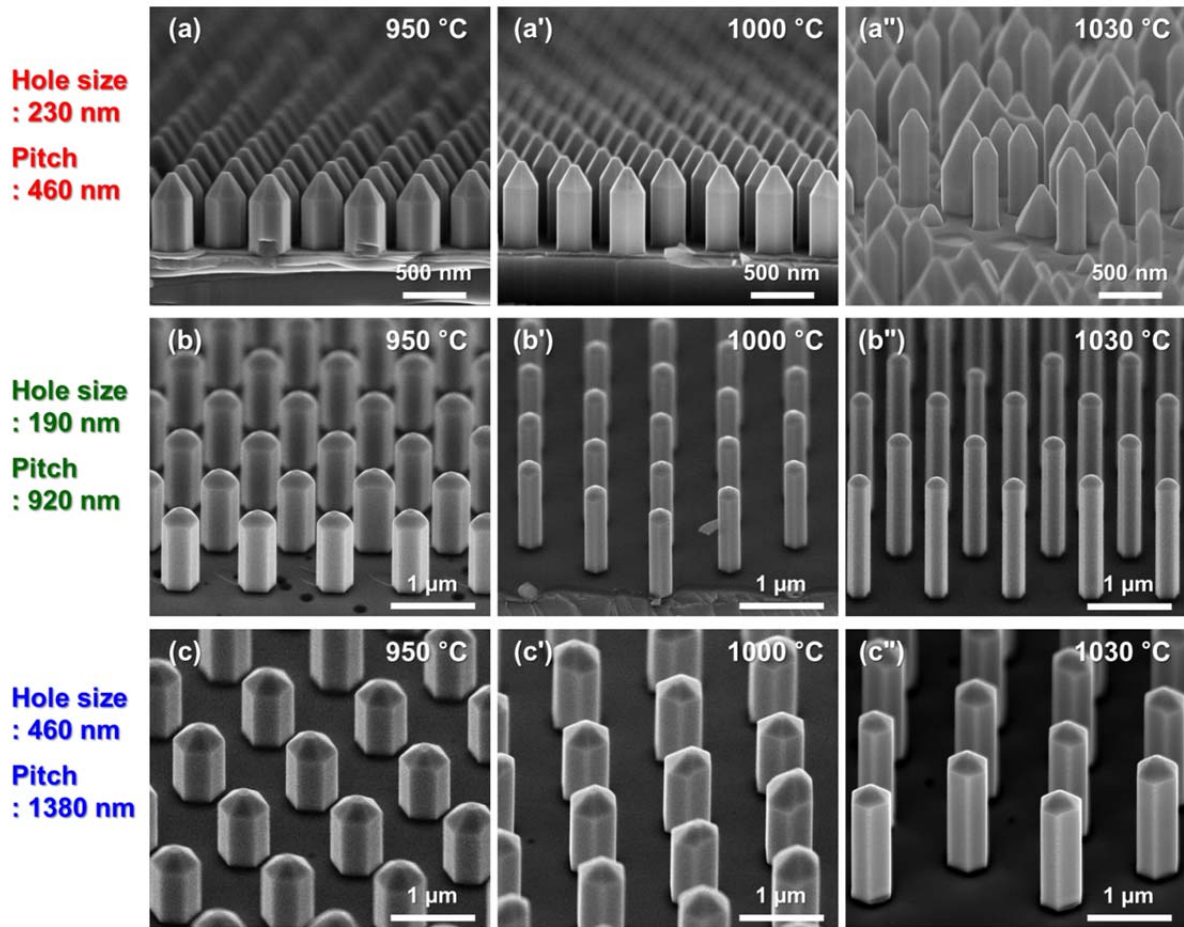
Figure 4.3 Cross-sectional FE-SEM images of selective-area-grown GaN nanorod arrays fabricated by pulsed-mode MOCVD procedure with different designs of the growth mask and growth temperatures. (a) − (a") Aperture size of 230 nm and pitch of 460 nm. (b) − (b") Aperture size of 190 nm and pitch of 920 nm. (c) − (c") Aperture size of 460 nm and pitch of 1380 nm.

However, the growth of the GaN nanorod arrays was found to depend on the design of the growth mask even under optimized growth conditions; hence, we suspect that the design of the growth mask may be an important factor determining the success or failure of the selective growth of GaN nanorod arrays as well as the growth conditions. Also, in the case of pulsed MOCVD, the correlation between the growth condition for SAG and the design of the

growth mask has not yet been fully clarified to the best of our knowledge. For this reason, experimental set II was performed to optimize the growth conditions. The FE-SEM images in Fig. 4.3 show the results of SAG by pulsed MOCVD for different designs of the growth mask, i.e., different aperture sizes and pitches. Every sample shows the typical lateral and vertical growth behavior depending on the growth temperature, regardless of the design of the growth mask. However, an interesting observation was made for the uniformity of the grown GaN nanorod arrays as shown in Fig. 4.3 (a"). In the case of a dense aperture pitch more irregular shapes were observed than in the case of a longer pitch. We consider that this behavior is related to the migration regions on the surface, which we refer to as the ' Ga collection areas'.[21, 22] The samples in (a"), (b"), and (c") may have exactly same the Ga collection area of circular shape with single aperture as its center caused by Ga migration length on the surface owing to the identical growth temperature. However, the Ga collection areas centered around the apertures may partially overlap in the case of short aperture distance. This assumption about Ga collection areas has already been reported in papers on the SAG of GaN nanorods by both MOCVD and molecular beam epitaxy (MBE).[21, 22] Therefore, the appropriate balance between the adsorption and desorption of Ga flux seems to be disturbed by overlapping Ga collection areas from the initial growth stages. Further study is required to investigate the reasons for this, which is beyond the scope of this study. However, in terms of optimizing the growth conditions, the SAG of GaN nanorod arrays was not successful for some mask designs despite the optimized growth conditions as shown in Fig. 4.3 (a"). This means that the growth conditions should be considered more carefully in the case of a dense aperture owing to the combination of effects such as reactants migration, density, adsorption, and desorption, which depend on the growth temperature. Although the growth of GaN nanorods has maintained complex mutuality caused by growth parameters, our results indicate that it is easier to optimize the growth conditions in the case of a longer aperture

distance, for which there may be less effect from neighboring apertures as well as no lateral coalescence.

4.3.3 Influence of number of pulsed-growth cycles

Many studies have determined for the optimum growth conditions of GaN nanorods by the source modulation technique, carrier gas, growth parameters, and other factors.[11-14] However, the effect of dominant diffusion process on the growth of nanorods is still incompletely understood to the best of our knowledge. This is due to the two different phase diffusion processes caused by pulsed MOCVD. If we can investigate the predominant diffusion process, it should be possible to more easily optimize the growth conditions for the SAG of GaN nanorod arrays. For this reason, experimental set III was performed with various numbers of pulsed-growth cycles. The FE-SEM images in Fig. 4.4 (a) – (d) show GaN nanorod arrays grown with different number of pulsed-growth cycles. The vertical length along the (0001) direction increased with the number of pulsed-growth cycles, whereas the lateral width remained almost constant diameter. These images clearly show the distinct features of pulsed MOCVD procedure of enhanced vertical growth and the suppression of lateral growth under optimized growth conditions. However, it is noteworthy that the growth rate per single pulsed-growth cycle gradually decreased, then saturated with increasing number of cycles. The Fig. 4.5 graph shows the vertical height and growth rate as functions of the number of pulsed-growth cycles. According to Hersee's original research, the key concept of pulsed growth procedure is to reduce the V/III ratio by rotating the injected precursor, which leads to the enhanced diffusion of the group III reactant.[13] However, the saturation of the growth rate indicates that the surface diffusion can have a limited effect on enhancing the vertical growth rate. Therefore, we consider that this behavior of Fig. 4.5 is involved in both the vapor phase and the surface diffusion process.
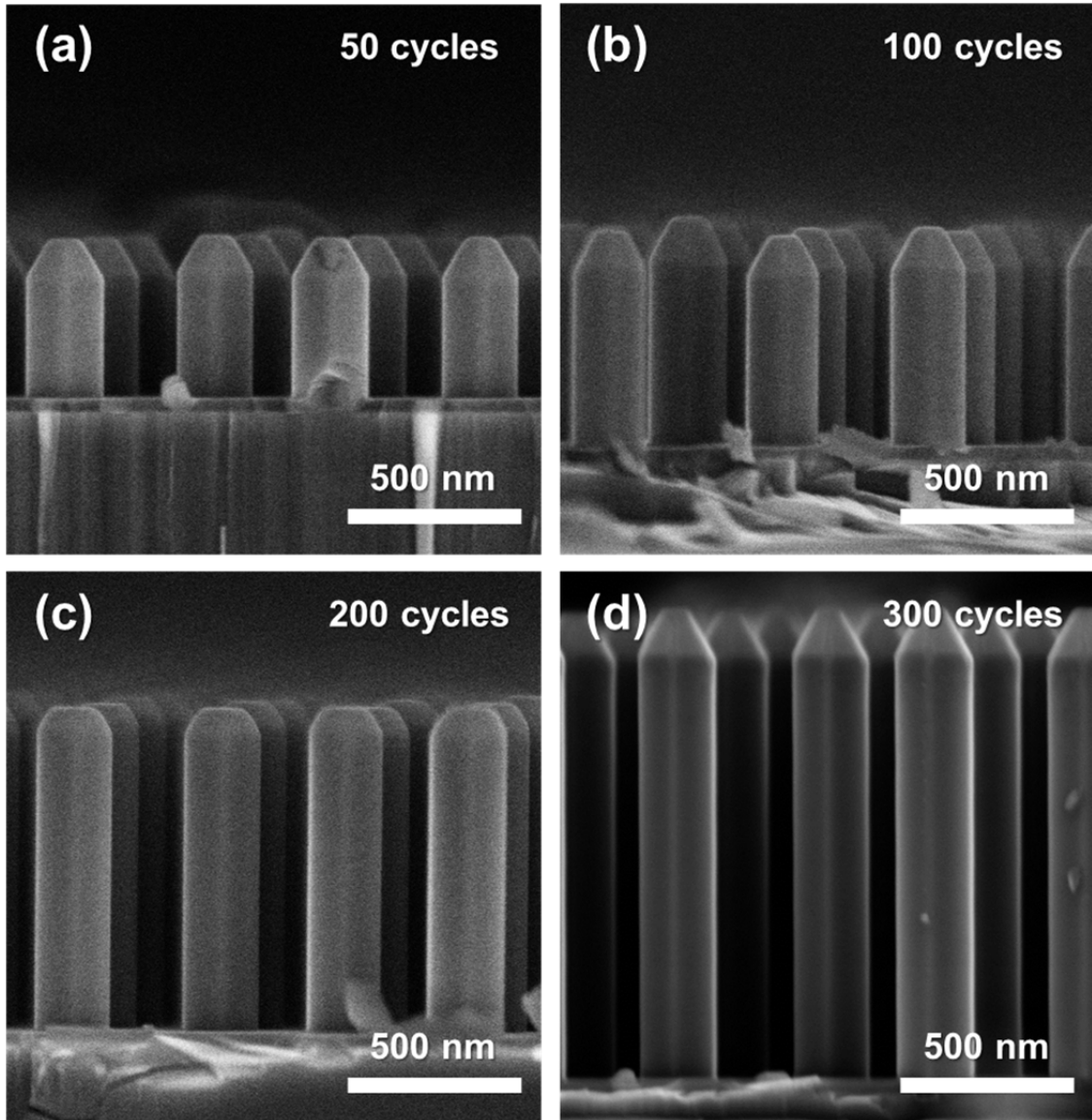
Figure 4.4 Cross-sectional FE-SEM images of selective-area-grown GaN nanorod arrays for various numbers of pulsed-growth cycles: (a) 50, (b) 100, (c) 200, and (d) 300 cycles.

We can consider three different processes (direct impingement, surface migration, and inter-plane diffusion from the *m*-plane to the *c*-plane) that occur in vertical growth. During the initial growth stage including the nucleation step, the growth of GaN is usually attributed to direct impingement into the window area by vapor phase state and the migration of the growth reactant from the dielectric making area if the reactants can be captured within the window area. However, from the decrease in growth rate shown in Fig. 4.5, the vertical

growth seems to be escaping gradually from influence of surface diffusion with increasing number of pulsed-growth cycles owing to lengthened height of GaN nanorod. There have been many studies on the length of Ga surface migration, which varies with the growth condition and the GaN crystal facets despite same growth condition.[21, 23] Even so, the length of Ga surface migration has a limited range. Therefore, if the height of the grown GaN nanorod is greater than the length of Ga migration from the masking area to the *m*-plane of the sidewalls along the (0001) direction, surface migration has a negligible effect on vertical growth. Consequently, the vertical growth of GaN nanorods is mainly affected by the direct impingement of the vapor phase on their apex because Ga atoms can take the place of hydrogen atoms on a $\{1\bar{1}01\}$ semipolar plane under Ga-rich growth conditions.[14, 24] For these reasons, the vertical growth rate of the GaN nanorods seems to remain almost constant even though the average growth rate is lower than the growth rate in the early stage. Additionally, we examined the effect of the vapor phase for GaN nanorods comparing with the planar structure. When we applied 300 pulsed-growth cycles to a *c*-plane planar epilayer, the average growth rate was 3.9 nm/cycle. Although the average growth rate per single pulsed-growth cycle for the GaN nanorod (4.46 nm/cycle) is slightly higher than that for the GaN planar epilayer, this is attributed to the enhanced growth rate from the early growth stage caused by surface diffusion. Actually, the number of pulsed-growth cycles has the same effect as the growth time in terms of optimizing the growth conditions. However, we consider that the enhancement of the vertical growth rate is limited unless the growth conditions are also varied. The control of the vertical growth rate can also enhance the efficiency of growth for a given growth time. Moreover, many different approaches are expected to be required to increase the vertical growth rate, because the length of the grown nanorods is still attractive factor for improving the device performance by extending the active area region.[10, 25]
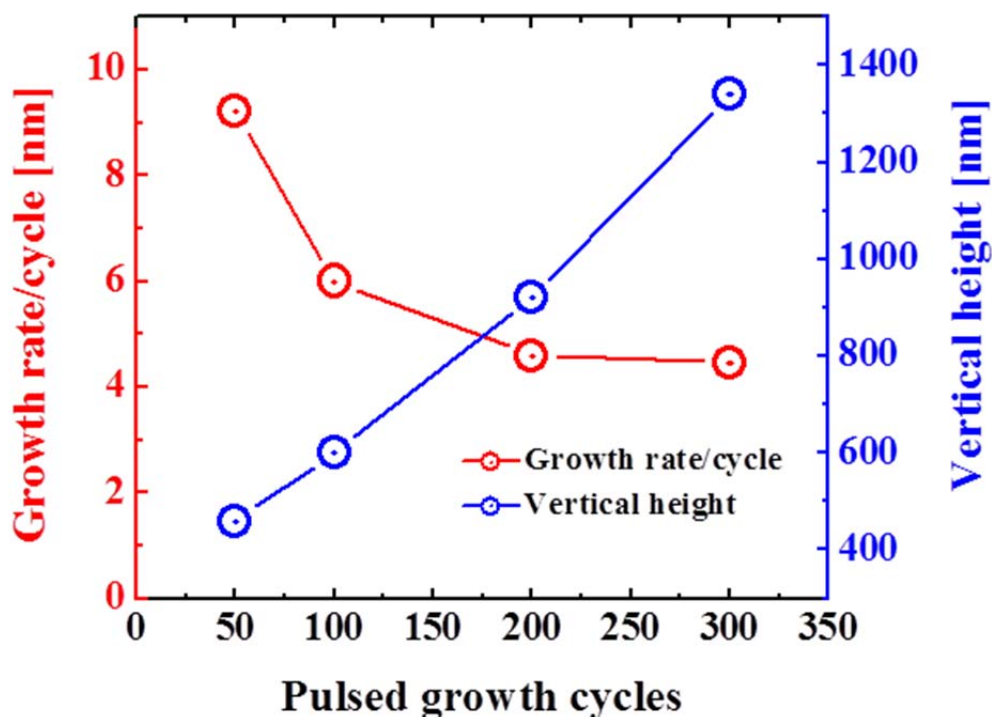
Figure 4.5 Average vertical growth rate per pulsed-growth cycle and vertical height as functions of number of pulsed-growth cycles.

4.3.4 Influence of NH₃ injection duration and luminescence properties

We carried out the experimental set IV to optimize the growth conditions for GaN nanorod arrays from the perspective of NH_3 injection duration. The growth of GaN nanorod arrays was found to be similar for different NH_3 injection durations as shown in Fig. 4.6 (a) – (c). We consider that this is related to the suitable pulsed-mode growth ratio (PMGR) as reported previously.[15] Actually, if the PMGR is within a suitable range, the SAG of GaN nanorod arrays is successful regardless of the NH_3 injection time, as reported in detail previous chapter.[15, 26] Although a negligible difference was observed among the grown GaN nanorod arrays, the optical properties, especially the YL, vary with the NH_3 injection duration as shown in the PL spectra in Fig. 4.7. We examined the optical properties of GaN nanorod arrays by room temperature PL measurement.
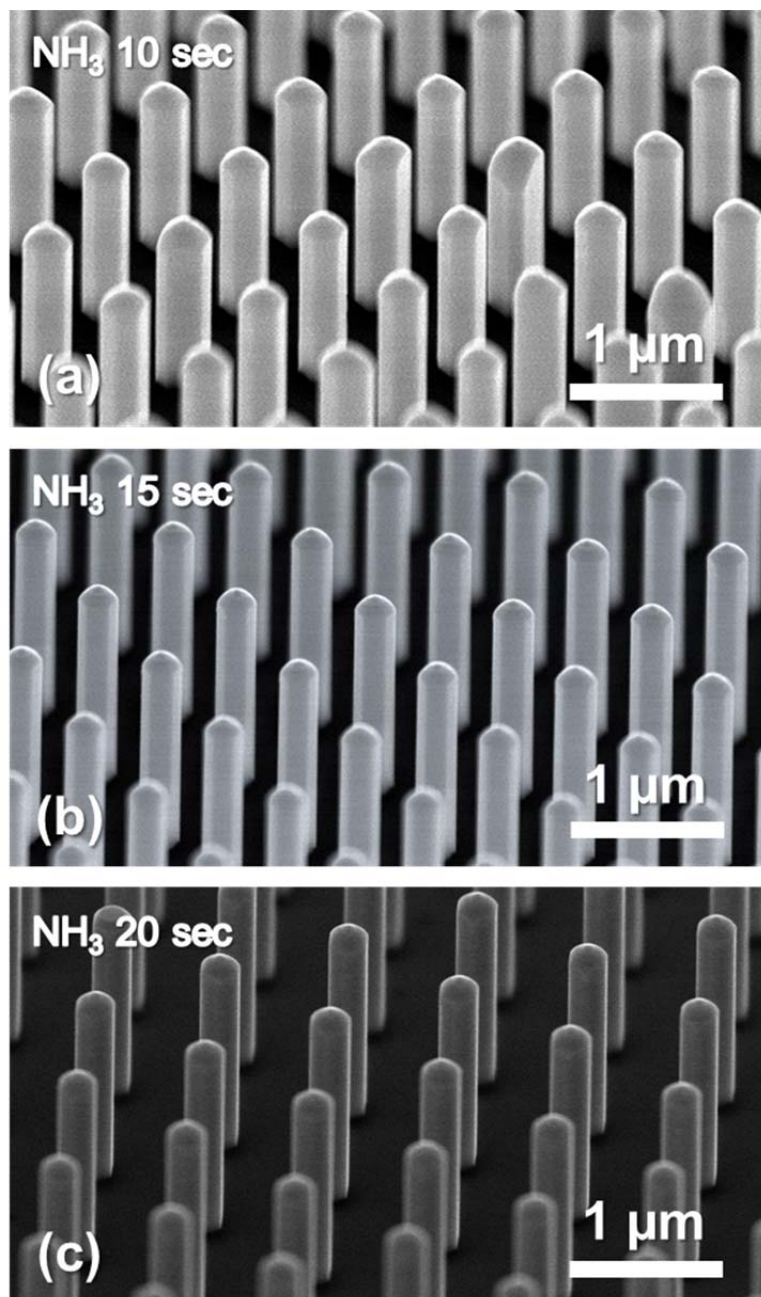
Figure 4.6 (a) – (c) images showing surface morphology of GaN nanorods for NH_3 injection durations of (a) 10, (b) 15, and (c) 20 s.

Hardly any peak shift of the near band edge (NBE) emission at approximately 365 nm was observed upon varying the NH_3 injection duration. On the other hand, it can be seen that the YL intensity changed with the NH_3 injection duration as shown in Fig. 4.7. It has been
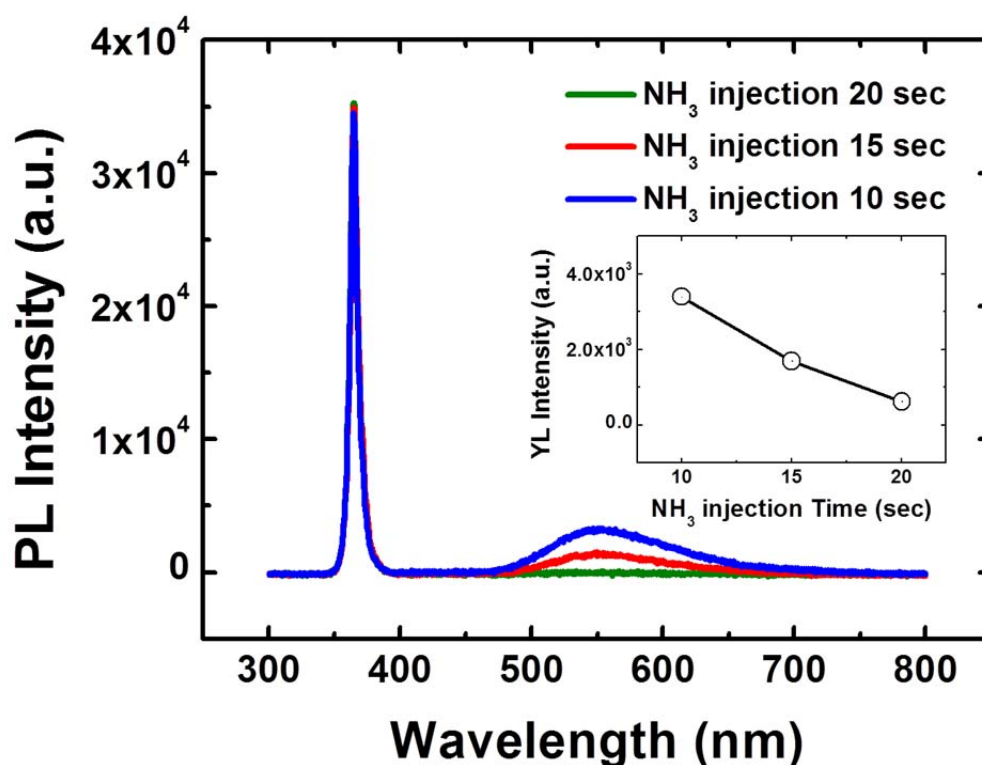
Figure 4.7 Room-temperature PL spectra of GaN nanorod arrays grown with different NH_3 injection times. The inset shows the intensity of YL as a function of the NH_3 injection time.

supposed in many studies that during the NH_3 injection, the YL of GaN nanorod arrays is generated from the thick GaN underlayer.[12, 13] However, these PL spectra indicate that the YL can arise from GaN nanorod arrays regardless of their origins.[27, 28] Despite this, we consider that the luminescence observed in this study originates from native defects. According to previous research, the YL intensity can be decreased by increasing the V/III ratio in conventional MOCVD GaN crystal growth, which decreases the number of generated defect impurity complexes such as V_{Ga}-O_N, even if the concentration of Ga-vacancy complex trapping sites increases.[10, 29, 30] As we mentioned in the experimental section 4.2, the V/III ratio can be changed by varying the NH_3 injection duration in spite of the constant NH_3 flow rate. We consider that a long NH_3 injection time will lead to a relative increase in V/III ratio compared with a short NH_3 injection time owing to the increased quantity of nitrogen atoms

inside the reactor. This leads to an increase in V/III ratio caused by the N-rich condition. For this reason, the YL properties can be suppressed under a N-rich growth condition. However, it is still possible that carbon induced the phenomenon of impurity incorporation.[31, 32] More research is necessary to obtain a deeper understanding of the origin of the YL properties of GaN nanorods grown by pulsed MOCVD. We will discuss this in the near future on the basis of detailed experimental results and analysis. In terms of only optimizing the growth conditions, we expect that the N-rich growth condition in pulsed MOCVD can lead to the improved crystallinity and optical quality of the GaN nanorod arrays. From the TEM investigation, we can confirm the high crystallinity of the grown GaN nanorods, as discussed in the next section.

4.4 Structural characteristics of the selective-area-grown GaN nanorods

To investigate the structural characteristics, the grown GaN nanorods (experimental set IV with 20 sec NH$_3$ injection duration) were examined by STEM. A cross-sectional BF TEM image of the GaN nanorods is shown in Fig. 4.8 (a), which was captured under [1$\bar{1}$20] zone-axis. Although the thick GaN underlayer has many dislocations, as can be seen in Fig. 4.8 (a), threading dislocations that penetrated into the GaN nanorod arrays were seldom observed. Most of the threading dislocations in the thick GaN layer were probably filtered out by the layer of the growth mask, resulting in the high crystallinity of the grown GaN nanorod arrays. The defect-free form can be attributed to the filtering of the crystal defects caused by nanoscale epitaxial growth.[33] In addition, typical structural defects such as twins and stacking faults could not be found in the GaN nanorods. The SADP and HR images in Figs. 4.8 (b) – (c), respectively, clearly indicate the strain-free and single-crystalline nature of the GaN nanorods. Furthermore, the polarity of GaN nanorod was also inspected by CBED

analysis at [1$\bar{1}$00] zone-axis. The two CBED patterns (experimental and simulated) were in good agreement as shown in Fig. 4.8 (d), indicating that the selective-area-grown GaN nanorods have Ga-face polarity.
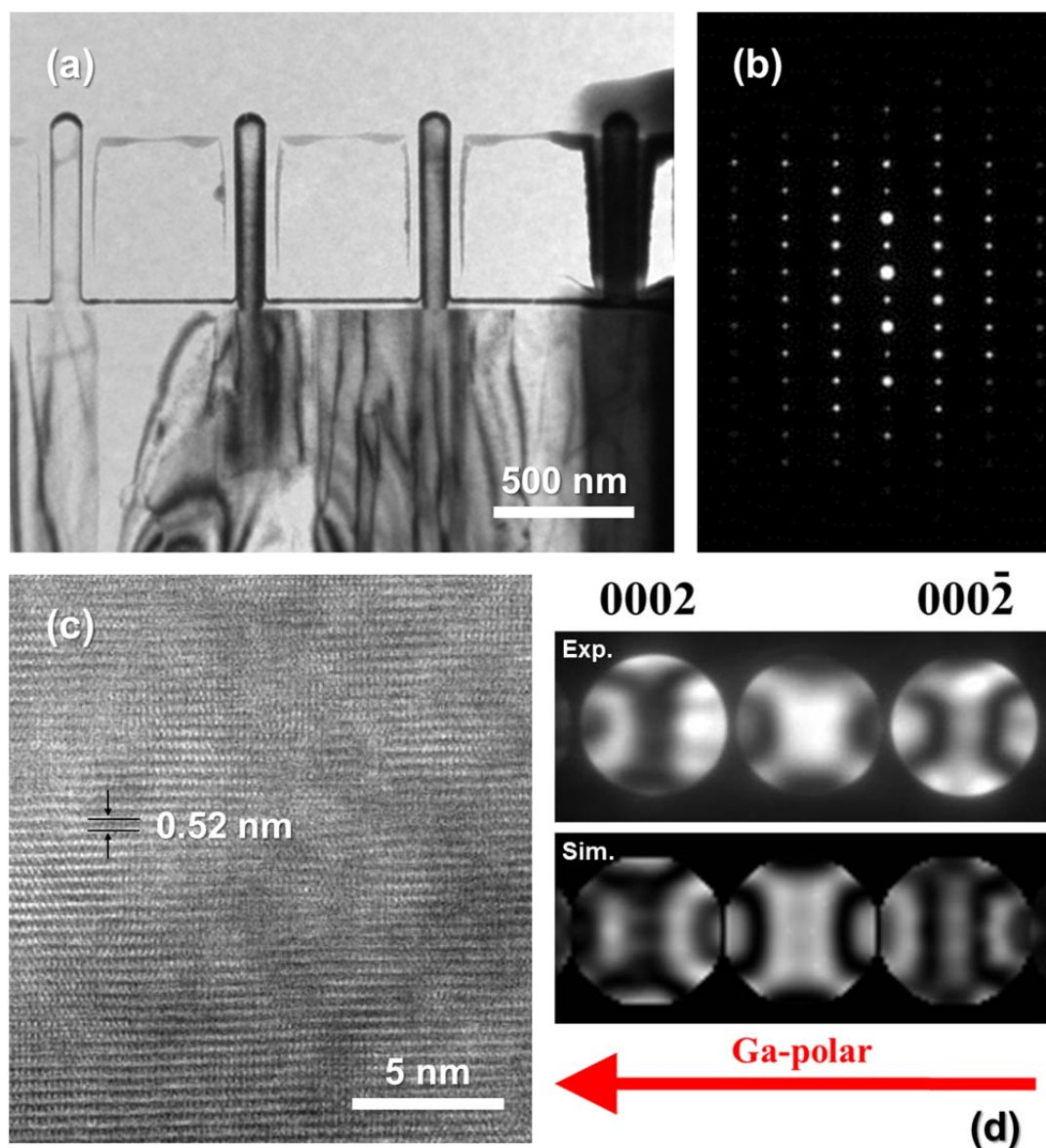


Figure 4.8 (a) Cross-sectional bright-field STEM image showing the vertically well-defined GaN nanorods with the filtering of dislocations from the thick GaN underlayer. (b) Selected area diffraction pattern indicating the wurtzite structure of GaN. (c) HR-TEM image of single-crystalline GaN nanorod. (d) The experimental (upper) and simulated (lower) CBED patterns ($d = 95$ nm thickness).

4.5 Discussion on optimization of growth conditions

From the perspective of optimizing the growth condition, the most important factor is how to enhance of the vertical growth rate while preventing lateral growth through the modification of, the growth temperature, the flow rates of the reactants, or other factors. As clarified by experimental sets I and II, the suppression of the lateral growth by increasing the growth temperature can be described in terms of the desorption rate of Ga adatoms from the m-plane sidewalls. Generally, the Ga desorption rate increases with the growth temperature regardless of the GaN crystal planes.[14, 34] In addition, according to Koleske's previous research, the desorption behavior of Ga adatoms is easily enhanced, particularly under an insufficient NH_3 growth condition, in GaN crystal growth by MOCVD.[19] The growth of GaN nanorods by pulsed MOCVD procedure can lead to insufficient NH_3 state owing to the repetition of Ga-related and N-interruption steps (NH_3 is not injected into the reactor during these steps). For these reasons, the lateral growth rate was suppressed by the desorption of Ga adatoms on m-plane sidewalls in conjunction with the increasing growth temperature. Furthermore, the vertical growth phenomenon is closely related to the Ga desorption rate on the m-plane sidewalls. Lin. *et al.* proposed the possibility of inter-plane migration from the m-plane to the c-plane for Ga adatoms desorbed from the m-plane in the case of pulsed MOCVD growth with different Ga sticking coefficients.[14] In addition, the desorption of Ga adatoms was enhanced by increasing the growth temperature, which may have enhanced the migration of Ga adatoms from the m-plane to the c-plane compared with that at a low growth temperature relatively. Consequently, the net vertical growth rate may have been enhanced through a change in the desorption rate owing to the possibility of the enhanced inter-facet migration of Ga adatoms caused by increasing the growth temperature, regardless of the TMGa flow rate. On the other hand, we consider that the effect of the TMGa flow rate for achieving rod shape can be approached from different viewpoints. Our observation of the

prompted vertical and lateral growth of GaN nanorods can be explained by the reduced V/III ratio and self-limiting mechanism, respectively.[35, 36] Generally, reducing the V/III ratio (increasing the TMGa flow rate or decreasing the NH_3 flow rate) will prompt vertical growth. Although it is difficult to accurately compute the V/III ratio in the case of pulsed MOCVD procedure owing to the alternating precursor injection step, if the TMGa flow rate is enhanced without changing the NH_3 condition (injection or flow rate), the V/III ratio within one pulsed-growth cycle will decrease. As a result, net vertical growth rate is induced by the effective reduction in V/III ratio caused by the enhanced TMGa flow rate. The enhancement of the lateral growth with increasing TMGa flow rate, as shown in Figs. 4.1 (a) and (a') can be explained by the additional supply of Ga reactants. The increased lateral supply of Ga reactants (both from the vapor phase and surface diffusion) by enhancing the TMGa flow rate can lead to excess Ga.[20, 35] As a result, a higher lateral growth seems to occur from the initial growth stage, particularly at a relatively low growth temperature, together with a low Ga desorption rate. In particular, the density of Ga adatoms available for SAG on the surface near the window region can play an important role in determining the growth rate and volume of selective-area-grown GaN. This consideration can be found in previous studies on SAG GaN on a stripe pattern with NH_3 modulation by MOCVD.[20, 35] A large correlation is observed among the variables for the SAG of GaN nanorod arrays in terms of only optimizing the growth conditions, and the low growth temperature reacts sensitively to the variation of TMGa flow rate and the lateral growth behavior appears strong with increasing TMGa flow rate. This is probably due to the low desorption rate of Ga adatoms on the *m*-plane sidewalls combined with the high Ga flow rate. In other words, a relatively high temperature makes it easier to growth of GaN nanorods owing to the reduced effect of the TMGa flow and Ga desorption rates as shown in Figs. 4.1 (a" – c") and 4.3., and discussed in section 4.3.2. The grown GaN nanorod arrays have a reasonably uniform geometry despite

the high TMGa flow rate (78 μmol/min) at a high temperature. Also, if we consider the crystallinity and optical quality as well as the GaN nanorod shape, a high growth temperature is better than a low growth temperature.[37] Nonetheless, the design of the growth mask for use at high temperatures requires careful consideration owing to the Ga collection areas. We believe that independent Ga collection areas are required for the uniform and selective growth of GaN nanorod arrays. The independence of Ga collection areas can be ensured by employing a suitable growth temperature and mask design. A long aperture pitch makes it easier to optimize the growth conditions than a short aperture pitch for the growth of uniform GaN nanorod arrays. However, the density of the aperture is closely related to surface area of the nonpolar m-plane required for the efficient growth of the $In_xGa_{1-x}N$/GaN MQW active layers.[25] Therefore, the design of the growth mask should be carefully controlled by considering the growth temperature.

4.6 Summary

● In this chapter, we reported the growth of position-controlled and vertically well-defined GaN nanorod arrays within a wide range of growth temperatures and different V/III ratios by pulsed MOCVD procedure, and we discussed the growth phenomenon from the perspective of optimizing the growth conditions.

● The vertical growth was enhanced and the lateral growth was suppressed by increasing growth temperature, regardless of the TMGa flow rate. On the other hand, both the vertical and lateral growth rates were increased by increasing the TMGa flow rate, independent the of growth temperature. We consider that the different behaviors for different growth parameters are related to the variation of surface adsorption, desorption, and diffusion, particularly that of Ga atoms, under different growth conditions.

● We also investigated the effect of the design of the growth mask on the SAG of GaN nanorod arrays. SAG using a mask with a longer aperture pitch was found to be less affected by the growth conditions owing to the existence of independent Ga collection areas.

● In addition, the dominant diffusion process was studied by investigating the effect of the number of pulsed-growth cycles. Both the vapor phase and surface migration affected the synthesis of GaN nanorod arrays during the early growth stage. However, the vapor phase had an increasingly major effect on the vertical growth rate with increasing number of pulsed-growth cycles.

● Furthermore, the YL characteristic of the selectively grown GaN nanorod arrays changed with the NH_3 injection duration. This may have resulted from the reduction in defect-related luminescence owing to the effective increase in V/III ratio with increasing NH_3 injection duration.

● On the basis of the various results of this study obtained from different experimental sets,

we expect that our reported outcomes for SAG GaN nanorod arrays will be established as the suitable guidelines for synthesis of III-N nanomaterials under optimized growth conditions. It is likely that the GaN nanorod structure can be adopted for nanotechnology-based functional optoelectronic application fields in the near future.

4.7 References

1) Y. J. Hong, C. H. Lee, A. Yoon, M. Kim, H. K. Seong, H. J. Chung, C. Sone, Y. J. Park, G. C. Yi; Adv. Mater. **23**, 3284 (2011).

2) J. C. Johnson, H.-J. Choi, K. P. Knutsen, R. D. Schaller, P. Yang, R. J. Saykally; Nat. Mater. **1**, 106 (2002).

3) E. C. Garnett, M. L. Brongersma, Y. Cui, M. D. McGehee; Annu. Rev. Mater. Res. **41**, 269 (2011).

4) B. O. Jung, D. C. Kim, B. H. Kong, D.-W. Kim, H. K. Cho; Sens. Actuators B **160**, 740 (2011).

5) D. Tham, C. Y. Nam, J. E. Fischer; Adv. Funct. Mater. **16**, 1197 (2006).

6) E. Le Boulbar, I. Girgel, C. Lewins, P. Edwards, R. Martin, A. Šatka, D. Allsopp, P. Shields; J. Appl. Phys. **114**, 094302 (2013).

7) J.-H. Kim, C.-S. Oh, Y.-H. Ko, S.-M. Ko, K.-Y. Park, M. Jeong, J. Y. Lee, Y.-H. Cho; Cryst. Growth Des. **12**, 1292 (2012).

8) J. H. Lee, D. C. Kim, J. Y. Lee, H. K. Cho; Cryst. Growth Des. **10**, 5205 (2010).

9) C. Durand, C. Bougerol, J.-F. Carlin, G. Rossbach, F. Godel, J. Eymery, P.-H. Jouneau, A. Mukhtarova, R. Butté, N. Grandjean; ACS photonics **1**, 38 (2013).

10) X. Wang, S. Li, M. S. Mohajerani, J. Ledig, H.-H. Wehmann, M. Mandl, M. Strassburg, U. Steegmüller, U. Jahn, J. Lähnemann; Cryst. Growth Des. **13**, 3475 (2013).

11) W. Bergbauer, M. Strassburg, C. Koelper, N. Linder, C. Roder, J. Laehnemann, A. Trampert, S. Fuendling, S. F. Li, H. H. Wehmann, A. Waag; Nanotechnology **21**, 305201 (2010).

12) S. Li, X. Wang, M. S. Mohajerani, S. Fuendling, M. Erenburg, J. Wei, H.-H. Wehmann, A. Waag, M. Mandl, W. Bergbauer, M. Strassburg; J. Cryst. Growth **364**, 149 (2013).

13)   S. D. Hersee, X. Sun, X. Wang; Nano Lett. **6**, 1808 (2006).

14)   Y.-T. Lin, T.-W. Yeh, P. D. Dapkus; Nanotechnology **23**, 465601 (2012).

15)   B. O. Jung, S.-Y. Bae, Y. Kato, M. Imura, D.-S. Lee, Y. Honda, H. Amano; CrystEngComm **16**, 2273 (2014).

16)   R. Koester, J.-S. Hwang, C. Durand, D. L. S. Dang, J. Eymery; Nanotechnology **21**, 015602 (2010).

17)   H. Amano, N. Sawaki, I. Akasaki, Y. Toyoda; Appl. Phys. Lett. **48**, 353 (1986).

18)   I. Akasaki, H. Amano, Y. Koide, K. Hiramatsu, N. Sawaki; J. Cryst. Growth **98**, 209 (1989).

19)   D. Koleske, A. Wickenden, R. Henry, W. DeSisto, R. Gorman; J. Appl. Phys. **84**, 1998 (1998).

20)   R. Q. Fareed, J. Yang, J. Zhang, V. Adivarahan, V. Chaturvedi, M. A. Khan; Appl. Phys. Lett. **77**, 2343 (2000).

21)   X. Wang, J. Hartmann, M. Mandl, M. S. Mohajerani, H.-H. Wehmann, M. Strassburg, A. Waag; J. Appl. Phys. **115**, 163104 (2014).

22)   T. Gotschke, T. Schumann, F. Limbach, T. Stoica, R. Calarco; Appl. Phys. Lett. **98**, 103102 (2011).

23)   L. Lymperakis, J. Neugebauer; Phys. Rev. B **79**, 241308 (2009).

24)   R. M. Feenstra, Y. Dong, C. Lee, J. Northrup; J. Vac. Sci. Technol. B **23**, 1174 (2005).

25)   B. O. Jung, S.-Y. Bae, S. Y. Kim, S. Lee, J. Y. Lee, D.-S. Lee, Y. Kato, Y. Honda, H. Amano; Nano Energy **11**, 294 (2015).

26)   A. K. Rishinaramangalam, S. M. U. Masabih, M. N. Fairchild, J. B. Wright, D. M. Shima, G. Balakrishnan, I. Brener, S. Brueck, D. F. Feezell; J. Electron. Mater. **44**, 1255 (2015).

27)   D. Hofmann, D. Kovalev, G. Steude, B. Meyer, A. Hoffmann, L. Eckey, R. Heitz, T.

Detchprom, H. Amano, I. Akasaki; Phys. Rev. B **52**, 16702 (1995).

28) M. A. Reshchikov, H. Morkoç; J. Appl. Phys. **97**, 061301 (2005).

29) S. Suresh, S. Lourdudoss, G. Landgren, K. Baskar; J. Cryst. Growth **312**, 3151 (2010).

30) K. Saarinen, P. Seppälä, J. Oila, P. Hautojärvi, C. Corbel, O. Briot, R. Aulombard; Appl. Phys. Lett. **73**, 3253 (1998).

31) R. Zhang, T. F. Kuech; Appl. Phys. Lett. **72**, 1611 (1998).

32) C. G. Van de Walle, J. Neugebauer; J. Appl. Phys. **95**, 3851 (2004).

33) R. Colby, Z. Liang, I. H. Wildeson, D. A. Ewoldt, T. D. Sands, R. E. García, E. A. Stach; Nano Lett. **10**, 1568 (2010).

34) S. Choi, T.-H. Kim, H. O. Everitt, A. Brown, M. Losurdo, G. Bruno, A. Moto; J. Vac. Sci. Technol. B **25**, 969 (2007).

35) X. Zhang, P. Dapkus, D. Rich; Appl. Phys. Lett. **77**, 1496 (2000).

36) N. Kobayashi, T. Makimoto, Y. Horikoshi; Jpn. J. Appl. Phys. **24**, L962 (1985).

37) Y. T. Lin, T. W. Yeh, Y. Nakajima, P. D. Dapkus; Adv. Funct. Mater. **24**, 3162 (2014).

Chapter 5

In$_x$Ga$_{1-x}$N/GaN MQW core-shell nanoarchitecture arrays

5.1 Background

III-nitride-based materials such as GaN, AlN, InN, AlGaN, and InGaN have received a lot of attention as an important system for manufacturing visible light-emitting diodes (LEDs) and laser diodes (LDs) for over 30 years.[1-5] In particular, LEDs have been used in mobile devices, display, and lighting source. LEDs have mainly been fabricated using *c*-plane polar GaN materials on sapphire substrates. This heteroepitaxial growth technique provides a satisfactory compromise between performance and cost in LED production. However, sapphire substrates still account for a large proportion of the production in the LED lighting market. Therefore, several types of material have been investigated as replacements for sapphire substrates, including silicon, glass, and plastic substrate.[6-8] Unfortunately, these various studies attempt\ing to overcome the current problems of LEDs are either in the early stages of technical development or require very complicated fabrication methods. Furthermore, there is still the unsolved problem caused by the spontaneous and piezoelectric polarization of *c*-plane LEDs regardless of the materials used as the substrate.[9, 10] In particular, the internal piezoelectric field within the multiple-quantum-well (MQW) active layer leads to spatial separation between the electron and hole wave functions. As a result, the polarization inside LEDs induces a large change in device properties such as reduced internal quantum efficiency (IQE), redshifted emission, and an increase in efficiency droop.[9-11] Therefore, to suppress these problems, a thin quantum-well (QW) structure of approximately 2-3 nm thickness should be applied to enhance the radiative recombination efficiency. However, a thin QW leads to high carrier concentrations and weak electron capture at the applying bias that will generate the Auger recombination. Owing to these detrimental effects,

it is difficult to avoid the "efficiency droop" of the LEDs on *c*-plane GaN.[11, 12] One of the most common ways of preventing polarization, increasing the QW thickness, and improving the radiative recombination efficiency is to grow a nonpolar GaN thin film such as one with a $(11\bar{2}0)$ *a*-plane or $(1\bar{1}00)$ *m*-plane orientation.[13, 14] Assuming that a nonpolar GaN bulk substrate with an isotropic crystal direction can be applied, such a substrate might be the best choice since it has low defect density as well as exact lattice matching. Typically only small GaN bulk substrates can be obtained using by hydride vapor phase epitaxy (HVPE) or the ammonothermal growth technique.[15, 16] However, although bulk nonpolar GaN substrates have low defect densities, their extremely limited sizes and very high cost preclude their widespread use.[14] Realistically, the large-scale and low-cost fabrication of nonpolar GaN thin film based LEDs can only be achieved by the heteroepitaxy of GaN on foreign substrates such as *r*-plane sapphire or SiC.[17, 18] Unfortunately, this also results in high structural defect densities such as partial dislocations (PDs), and prismatic and basal stacking faults (PSFs and BSFs) in the case of a typical two-dimensional (2D) planar structure.[17-19]

One-dimensional (1D) semiconductor materials have been attracting attention in many research fields as a means of overcoming various problems. In particular, GaN nanostructures are expected to be a good substitute for the nonpolar GaN-based LED structure owing to their desirable and interesting properties such as a large surface-area-to-volume ratio,[20] low defect density,[21] the possibility of higher indium incorporation,[22] and the exposure of various facets.[23] For example, nonpolar $\{1\bar{1}00\}$ *m*-plane sidewalls can be utilized as basal templates for the heteroepitaxial growth of InGaN/GaN MQWs. The nonpolar $\{1\bar{1}00\}$ *m*-plane sidewalls are expected to lead to an improved radiative carrier recombination rate, the opportunity to control the effective QW thickness, and the prevention of efficiency droop. Generally, GaN nanostructures can be fabricated by various synthetic methods: a top-down

etching approach,[24] vapor-liquid-solid (VLS) growth,[25] molecular beam epitaxy (MBE),[26] and selective area growth (SAG) by metalorganic vapor phase epitaxy (MOVPE).[23, 27] As a result of advances in nanowire growth, optoelectronic devices with novel structures have been demonstrated with uniaxial or core-shell nanoarchitectures. However, in numerous instances, their output performance (electroluminescence or light emission efficiency) remained at the single-nanowire scale.[28, 29] Therefore, the realization of highly ordered coaxial nanoarchitecture arrays over a large area is necessary to improve their performance.
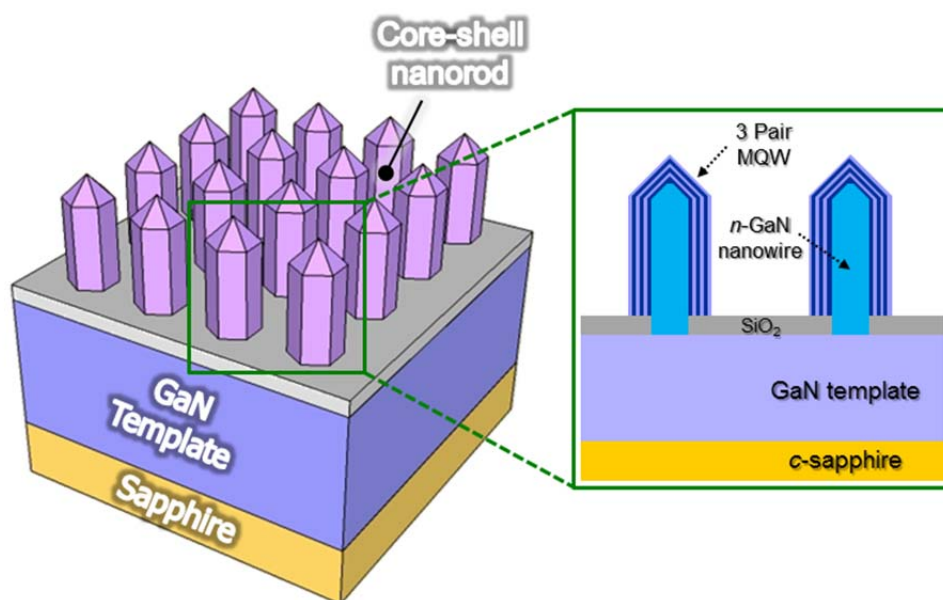
Figure 5.1 Schematic sketch of a GaN-nanorod-based InGaN/GaN MQWs core-shell nanoarchitecture array. The expanded schematic shows the formation of a layer comprising three pairs of MQWs on *n*-GaN nanorod core.

Here, we investigate the synthesis of GaN nanorod based InGaN/GaN MQW core-shell architecture arrays with a large area. The basic strategy for the large-scale fabrication of vertically well-aligned GaN nanorod based MQW coaxial arrays involves (i) adopting catalyst-free MOCVD as the growth technique including a pulsed (for GaN nanorod arrays)

or constant growth mode (for InGaN/GaN MQWs), (ii) utilizing the nonpolar $\{1\bar{1}00\}$ *m*-plane sidewalls of GaN nanorods as a basal template to avoid the formation of piezoelectric fields and improve radiative recombination efficiency, and (iii) employing an extended $\{1\bar{1}00\}$ *m*-plane sidewall area to enhanced light output power. Sidewalls enlarged in the vertical direction can also contribute to improving light extraction efficiency owing to their three-dimensional (3D) arrangement. In order to clarify our approach, the GaN nanorod based InGaN/GaN MQWs coaxial nanoarchitecture arrays are shown schematically in Fig. 5.1.

5.2 Experimental section

5.2.1 Preparation of substrate

A GaN epilayer with a (0002) plane preferential orientation was used as a basal template for GaN nanorod array synthesis by MOCVD. First, a thin dielectric SiO_2 layer was deposited by RF magnetron sputtering as a growth mask on a 3-µm-thick Si-doped *n*-GaN epitaxial layer with high crystalline quality. Then, the patterns of nanoscale circular hexagonal were formed by thermal nanoimprint lithography. After the nanoimprint process, the SiO_2/*n*-GaN template was transferred to a reactor for CF_4-based reactive-ion etching (RIE) to etch the SiO_2 selectively. Finally, the template was cleaned using an O_2 plasma treatment process for 10 min to completely eliminate any residual nanoimprint resin remaining on the surface.

5.2.2 Growth procedure

For the growth of GaN nanorod arrays, the SiO_2/GaN/sapphire template was loaded into a showerhead-type MOCVD reactor. The synthesis of highly ordered GaN nanorod arrays was carried out at 1020 °C and a pressure of 200 Torr using trimethylgallium (TMGa) and ammonia (NH_3) as precursor sources by employing a TMGa and NH_3 modulation growth

technique called "pulsed-mode MOCVD growth" with pure hydrogen (H_2) as the carrier gas. The TMGa and NH_3 flow rates were maintained at 15 sccm (78 μmol/min) and 5 slm (223.21 mmol/min), respectively. The modulation growth technique consists of (1) an NH_3 injection step, (2) an NH_3 interruption step, (3) a TMGa injection step, and (4) a TMGa interruption step. Details of this pulsed-mode process have been introduced in chapter 3 of this thesis.[23] Subsequently, the three periods of InGaN/GaN MQWs were formed on the GaN nanorod by conventional constant-mode growth. For the InGaN/GaN MQW coaxial nanostructure arrays, trimethylindium (TMI), triethylgallium (TEG), and NH_3 were used as the QW and quantum-barrier (QB) precursor sources under pure nitrogen (N_2) ambient. The flow rates of TEG and TMI were maintained at 100 sccm (29.92 μmol/min) and 400 sccm (40.29 μmol/min), respectively, during the growth of the three period InGaN (QW) and GaN (QB) at a reactor pressure of 200 Torr. The $In_xGa_{1-x}N$ QWs were grown at temperatures from 700 to 800 °C and the GaN QBs were grown at the same temperature. In order to investigate the light emission properties of the MQWs on nonpolar $\{1\bar{1}00\}$ *m*-plane sidewalls, the number of pulsed-growth cycles was varied between 100 and 300 depending on the experiment types.

5.2.3 Characterizations

The surface morphology and microstructural characterization of GaN nanorods and $In_xGa_{1-x}N$/GaN coaxial nanoarchitecture arrays were carried out by field-emission scanning electron microscopy (FE-SEM, S-5200) and Cs-corrected scanning transmission electron microscopy (Cs-corrected STEM, JEM-ARM200F), respectively. Before being subjected to TEM analysis to obtain bright-field (BF) images, high-resolution (HR) images, and electron diffraction pattern, the samples were milled using a dual-beam focused ion beam (DB-FIB, NOVA200) operated in the range of 5-30 kV. The room-temperature photoluminescence (PL)

was investigated using a He-Cd laser operating at 325 nm with different excitation power to determine the optical properties of the GaN nanorods and $In_xGa_{1-x}N$/GaN MQW core-shell arrays. The local emission from the coaxial structure of the MQWs was investigated by cathodoluminescence (CL) measurements (Carl Zeiss Ultra 55 FE-SEM with a Gatan's MonoCL3 system).

5.3 InGaN/GaN MQW core-shell nanoarchitecture arrays

5.3.1 Shape control and optical properties of GaN nanorod arrays

Figures 5.2 (a) – (c) show tilted-view FE-SEM images of GaN nanorod arrays grown by position-controlled SAG. Highly ordered and vertically well-aligned GaN nanorods with reasonably uniform dimensions such as length and diameter were obtained over a wide area as shown in Fig. 5.2 (d) inset image. The diameter of the GaN nanorods was 220±5 nm and the length could be controlled from 300 nm to more than 1.5 μm. According to a previous result, in the growth of GaN nanostructures by pulsed-mode MOCVD, the variation of the GaN nanorod length is mainly caused by the pulsed-mode growth cycle and the diameter of GaN nanorods primarily depends on the size of the window in the mask used for dielectric layer.[23] The average growth rate of the GaN nanorods was 900 nm/h under our experimental conditions. Six-fold symmetric nonpolar $\{1\bar{1}00\}$ *m*-plane sidewalls clearly were formed on the predominant geometry without any particles, which are considered essential for obtaining high-quality coaxial MQW structures. Another important point is the shape of the tops of the GaN nanorods. The Ga-polar GaN nanorods typically show three different facets: a (0002) polar facet of the topmost, nonpolar $\{1\bar{1}00\}$ facet sidewalls, and semipolar $\{1\bar{1}01\}$ slanted facets regardless of the area of the planes. This feature may be highly advantageous for LEDs with multicolor emission.[30]
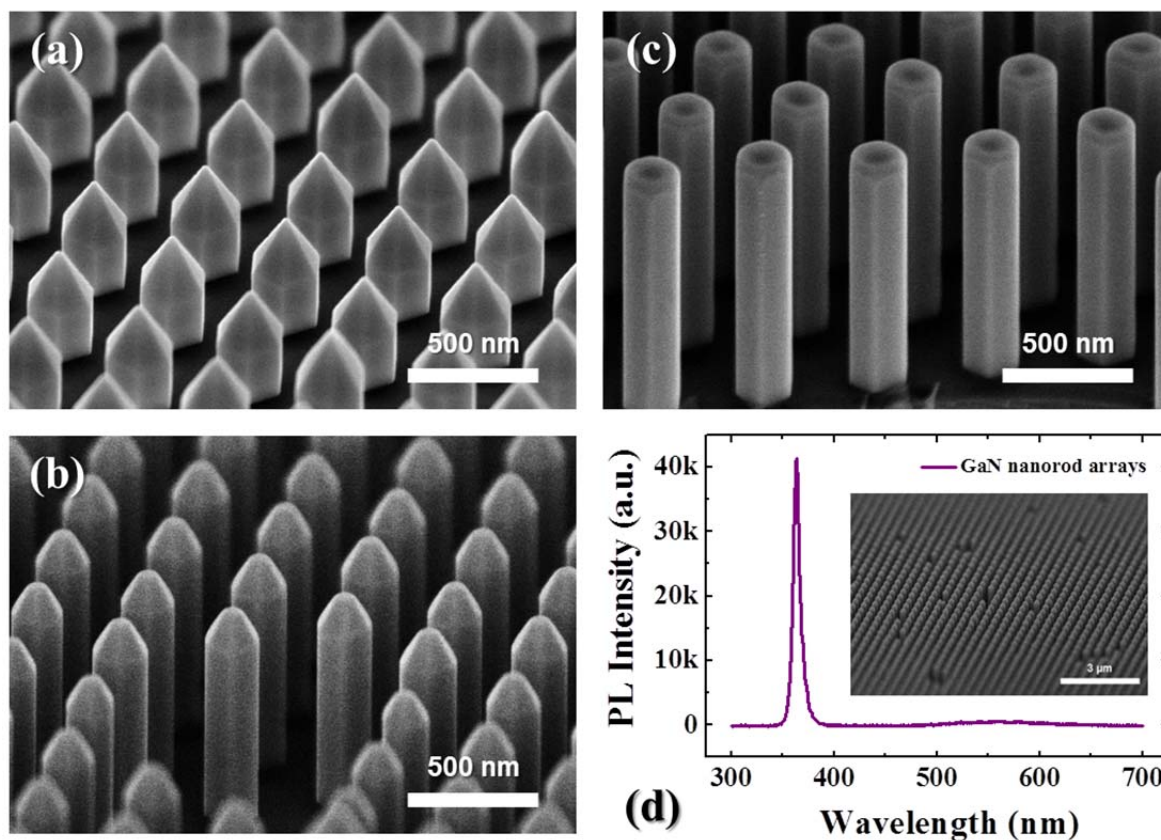
Figure 5.2 Cross-sectional SEM images of GaN nanorod array showing (a) morphology of the tops of the GaN nanorods without the *c*-plane. (b) two different crystal planes (*c*-plane and semipolar facets) on the upper region of the GaN nanorod. (c) *c*-plane terminated tops of the GaN nanorod. (d) Room-temperature PL spectrum of the basal GaN nanorod array. The inset SEM image is highly-ordered selective-area-grown GaN nanorod array with large area scan.

However, the three different facets may be disadvantageous for obtaining monochromatic spectral emission owing to the different amounts of indium incorporation. Therefore, the control of GaN nanorod crystal planes at their apex may be an important requirement for pure-color emission. To minimize the *c*-plane region of GaN nanorods, we applied a non-involving filling process growth technique, which is described at previous chapter in detailed procedure.[23] As shown in Fig. 5.2 (a), the *c*-plane surface was barely distinguishable

compared with in Figs. 5.2 (b) and (c) and the GaN nanorod apex exhibited a very sharp morphology. To determine the crystal quality and optical characteristics of the GaN nanorod arrays, we carried out room-temperature PL measurement. An intense ultraviolet (UV) emission peak centered at approximately 365 nm was observed as shown in Fig. 5.2 (d). This UV emission peak is attributed to the recombination of free excitons, i.e., the near-band-edge (NBE) emission of GaN nanorods. Yellow luminescence (YL) emission at longer wavelength was hardly observed, indicating the high crystalline and optical quality of the GaN nanorods. Many arguments have suggested for the origin of the yellow emission such as native isolated defects and other impurities.[31]

5.3.2 Surface morphology and optical properties of InGaN/GaN MQW core-shell nanoarchitecture arrays

Figures 5.3 (a) − (c) show tilted-view SEM images of the InGaN/GaN MQWs coaxial structure nanoarrays with various magnifications. After the growth of MQWs on the GaN nanorods, their structure remained highly ordered with a vertically well-aligned geometry as ever. The highly ordered coaxial arrays have high uniformity, with an average diameter of 285±5 nm and length of 1.5±0.02 μm. In addition, we determine the optical properties of InGaN/GaN coaxial array with different core-sell apexes (with and without the *c*-plane) as shown in Fig. 5.3 (d). Their PL spectra exhibit slightly different behaviors. Both PL spectra have a dominant emission peak at approximately 430 nm. However, the core-shell structure including the *c*-plane has a relatively weak emission peak at approximately 500 nm, corresponding to the near-green region. Moreover, the emission spectrum is also broader than that for the coaxial structure without the *c*-plane. As mentioned before, the GaN nanostructure must have different crystal planes for at least two facets.[23, 32] In particular, the *c*-plane must have a higher indium incorporation rate than the other planes, which can be
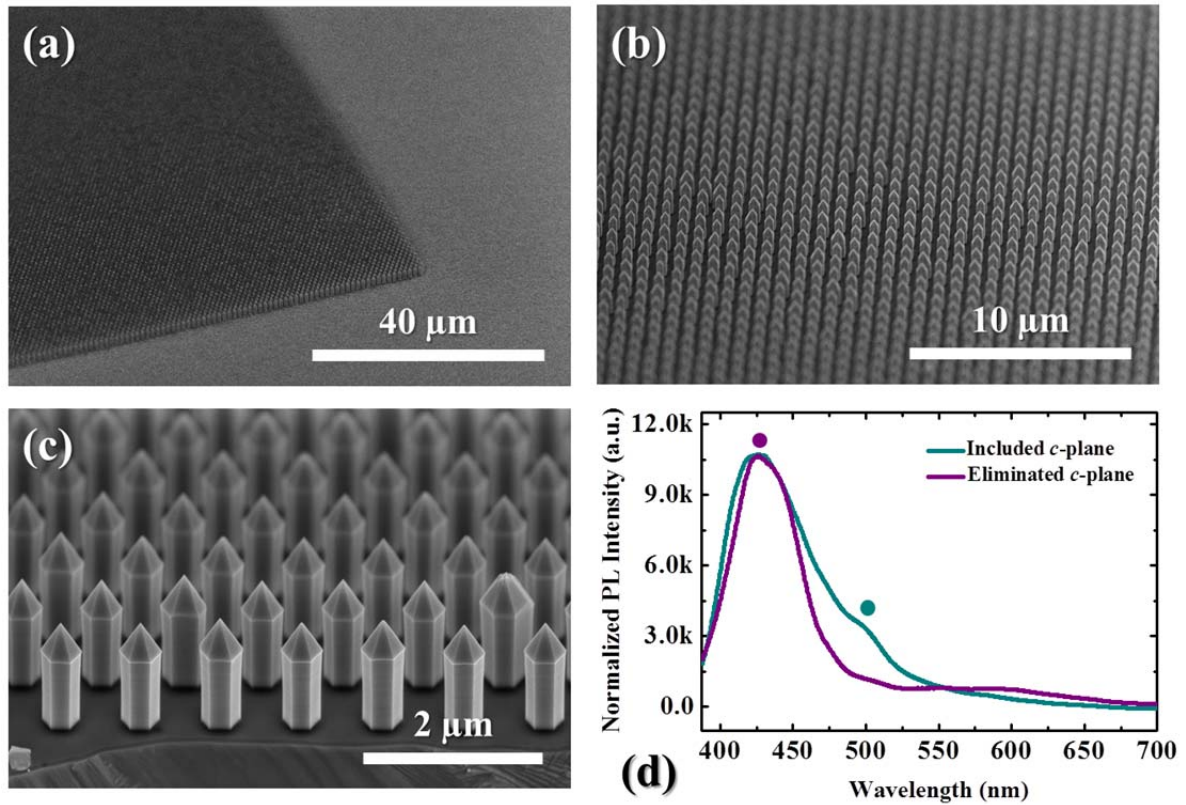
Figure 5.3. (a) – (c) Tilted-view SEM images of the GaN nanorod based $In_xGa_{1-x}N$/GaN MQWs coaxial nanoarchitecture arrays with different magnifications. (d) Normalized PL spectra of three pairs of InGaN/GaN coaxial arrays with and without *c*-plane in GaN nanorods. The dots indicate the respective PL peak positions.

disadvantageous for monochromatic light emission. Also, MQWs on the *c*-plane can prevent efficient radiative recombination owing to the significant spatial separation of the hole and electron wave functions caused by the considerably thicker QW and QB layers than on the other planes. For these reasons, we consider that to obtain monochromatic emission spectra, it is better to minimize the area of the *c*-plane instead of multiple crystal facets. The *c*-plane could be hardly observed in the GaN nanorods shown in Fig. 5.1 (a). This can lead to nearly monochromatic light emission by preventing the formation of MQWs owing to the undefined crystal orientation caused by the limited *c*-plane area. This will be discussed in detail next in

this chapter. To investigate the emission properties of the eliminated *c*-plane InGaN/GaN core-shell structure array, we measured the excitation power-dependences of the PL spectra with different power-density as shown in Fig. 5.4. The maximum power-density was defined as an I_0 ($I_0 = 763.95$ W/cm^2). The dominant emission peak of the InGaN/GaN coaxial structure was observed at approximately 430 nm under lowest excitation power-density of 7.64 W/cm^2. In addition, the spectra show that the intensity of light emission from the InGaN/GaN coaxial structure was consecutively increased with excitation power up to I_0 without any remarkable shift in their wavelengths. Furthermore, we could not discover any satellite peak at longer wavelengths region corresponding to the MQW of (0002) and {1$\bar{1}$01} planes as shown in inset spectra of Fig. 5.4. This investigation indicates that the light emission mainly originates from MQWs on nonpolar {1$\bar{1}$00} *m*-plane sidewalls, this is decisive evidence that the light emission from MQWs on *m*-plane dominated the luminescence characteristic of InGaN/GaN core-shell structure arrays.
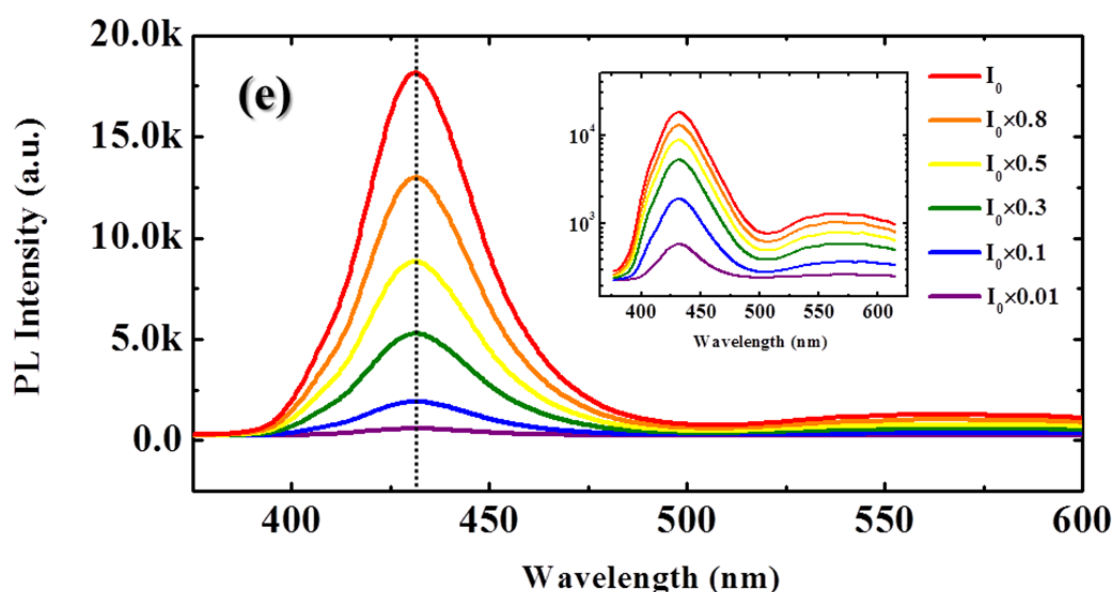
Figure 5.4 Excitation power-dependent PL spectra of the InGaN/GaN core-shell structure array without *c*-plane in GaN nanorod at 300 K. The inset is PL spectra of log scale.

5.3.3 Structural investigation of *n*-GaN nanorod inner core
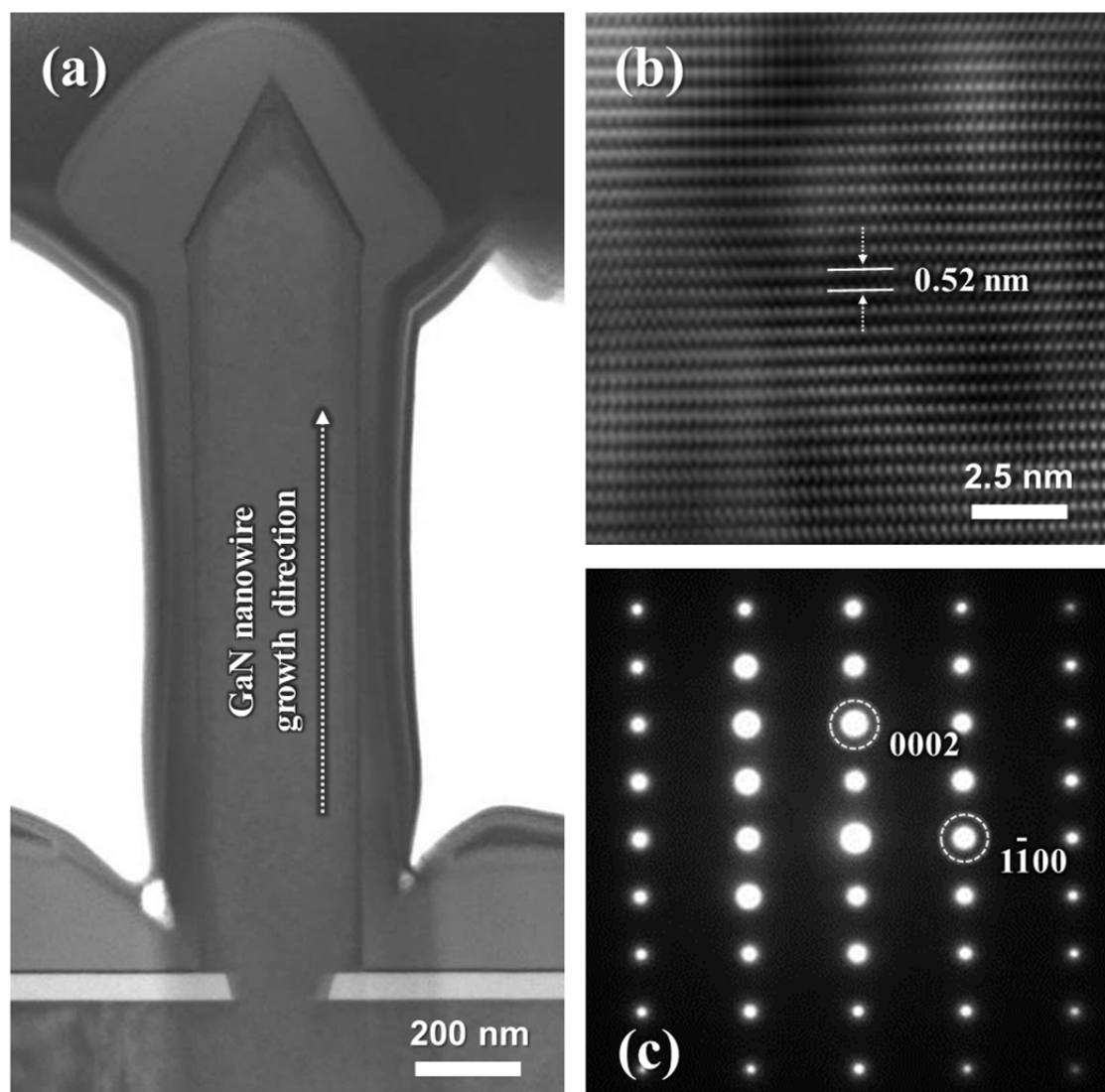
Figure 5.5 (a) Low-magnification cross-sectional STEM image of single InGaN/GaN MQWs coaxial structure. (b) HR-TEM image of the single-crystalline *n*-GaN nanorod core. (c) Selected-area electron diffraction pattern measured from [11$\bar{2}$0] zone-axis.

The low magnification BF TEM image in Fig. 5.5 (a) was captured from a single coaxial nanorod. Relatively dark layers can be observed on the outside of GaN nanorod. Figure 5.5 (b) shows a HR image obtained from the *n*-GaN nanorod core. The lattice distance between adjacent facets was estimated to be ≈ 5.2 Å, indicating the strain-free characteristic of the *n*-

GaN inner core. From the electron diffraction pattern in Fig. 5.5 (c), we can confirm the single-crystalline nature of the GaN nanorod. In addition, we could not observe any typical GaN defects in the GaN nanorod core such as stacking faults or dislocations. This may be related to the filtering effect of crystal defects caused by nanoscale epitaxial growth.[21]

5.3.4 Optical properties and fill-factor (FF) computation of InGaN/GaN MQW core-shell nanorod

The optical characteristics of the InGaN/GaN MQW core-shell structure arrays were inspected by measuring the CL spectrum. Figure 5.6 (a) shows cross-sectional CL spectra of InGaN/GaN coaxial structure arrays with different GaN nanorod *m*-plane surface areas. Generally, the *m*-plane area of GaN nanorod sidewalls can be controlled using pulsed growth cycles. Irrespective of the dominant peak intensity, InGaN/GaN MQW emission is observed from the coaxial structure at approximately 430 nm.
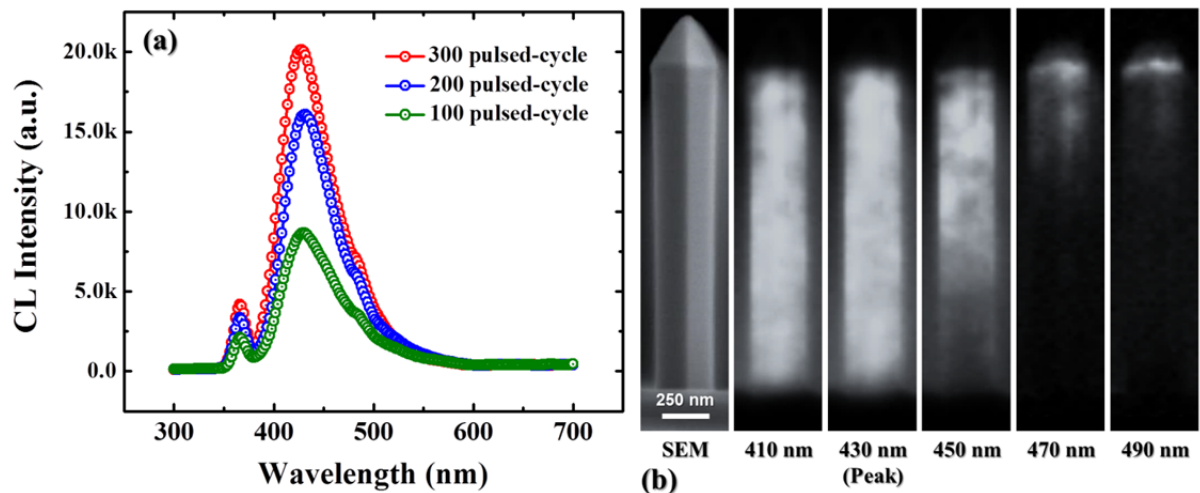

Figure 5.6. (a) CL spectra of InGaN/GaN coaxial nanowires depending on different basal *m*-plane area. (b) Monochromatic CL mapping images of MQW coaxial nanowires based on 300 pulsed growth cycles observed at wavelengths of 410, 430, 450, 470, and 490 nm.

Figure 5.6 (b) shows the monochromatic CL images recorded at wavelengths of 410, 430, 450, 470, and 490 nm. The images clearly show bright emission from the *m*-plane sidewall of core-shell structure. Also, weak emission was observed at longer wavelengths that originated from the edges between the $\{1\bar{1}00\}$ *m*-plane and the $\{1\bar{1}01\}$ semipolar plane, as shown in the monochromatic CL images recorded at 470 and 490 nm. The slight shoulder at the longer wavelength is attributed to this emission from the edge regions. The dominant emission peak at 430 nm clearly originates from MQWs grown on the six-fold *m*-plane sidewall of the GaN nanorods. The dominant emission peak intensity has different behavior depending on the *m*-plane basal area of the GaN nanorod as shown in Fig. 5.6 (a). Varying the *m*-plane area may affect the intensity of light emission. In many optoelectronic devices such solar cells, optical sensors, and photodetectors, output gain is improved by expanding the junction or active area region.[33-35] In particular, the large surface-area-to- volume ratio is one of the most distinct characteristics in advantages of nanoarchitecture arrays. Typically, high power or high efficiency GaN-based LEDs have a large chip size, which extends the active area region. Also, a large chip can generally have a higher driving current than a smaller chip, indicating that a higher applied bias leads to higher optical output power. To increase the light output power, we must extend the active area to obtain a high driving current. In order to investigate the feasibility of extending the surface area of a core-shell nanorod, we calculated the fill factor (FF) of the effective active region per unit cell area, where the FF was defined as follows equation (1).

$$Fill\ Factor\ (FF) = \left[\frac{(Total\ area\ of\ m-plane\ sidewalls\ inside\ unit\ cell)}{(Total\ area\ of\ unit\ cell)} \right] \times 100\ (\%) \quad (1)$$

Here the unit cell was defined as the hexagonal planar surface. In other words, an FF of 100 %

means that the total sidewall area of the nanowire inside a unit cell is equal to the total area of the unit cell. The *m*-plane height of the GaN nanorod mainly depends on the number of pulsed growth cycles as shown in Fig. 5.7.
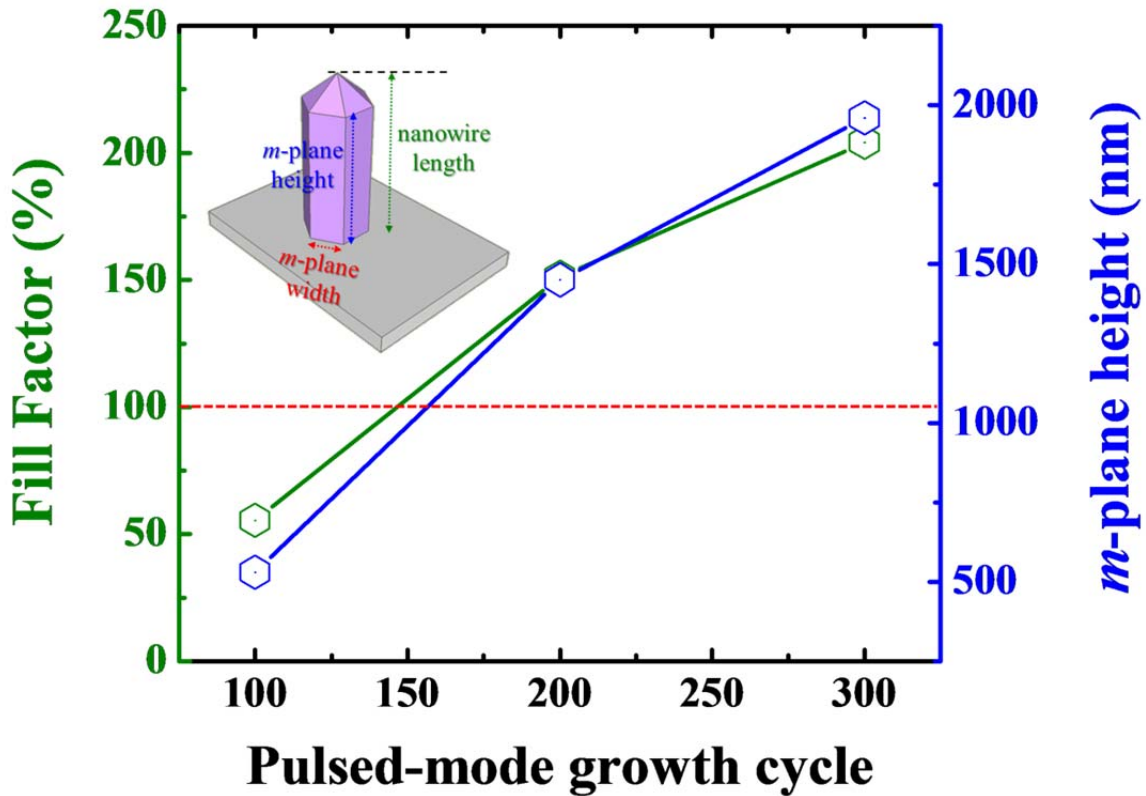
Figure 5.7. Fill factor and *m*-plane height of GaN nanorod as a function of number of pulsed growth cycles (the red dotted line indicates a fill factor of 100% depends on *m*-plane height). Schematic image of inset defines the GaN nanorod length, *m*-plane height, and width.

The height of *m*-plane, width, and length of GaN nanorod was indicated within inset of Fig. 5.7. The area of a single *m*-plane, the total area of the *m*-plane sidewalls of the single GaN nanorod, and statistical data for the whole *m*-plane area of GaN nanorods inside the unit cell of a regular hexagon are summarized in Table 5.1.

Table 5.1 Computation results of single, six-fold, and total *m*-plane area and FF nomalized by unit cell area.

	Single *m*-plane area of nanorod [μm^2]	Six-fold *m*-plane area of nanorod [μm^2]	Total *m*-plane area per unit cell [μm^2]	Unit cell area (regular hexagon) [μm^2]	Normalized FF
Pulsed 100 cycles	0.080	0.48	1.44		0.554
Pulsed 200 cycles	0.218	1.31	3.93	2.6	1.512
Pulsed 300 cycles	0.295	1.77	5.31		2.042

(* *m*-plane width = 150 nm)

(* pattern spacing on unit cell = 1 μm)

In the case of 100 pulsed growth cycles, the FF was calculated to be about 55.4%. This indicates that the surface area was reduced by 44.6% through the shorter nanorod length in comparison with the planar unit cell. On the other hand, in the case of 200 and 300 pulsed growth cycles, the FF is markedly increased from 55.4 to 151.2 and 204.2%, respectively, as shown in Fig. 5.7, according to the *m*-plane height of the GaN nanorod. This indicates that if we increase the vertical to lateral aspect ratio of the GaN nanorods, the basal area of the *m*-plane can also be increased to extend the size of the MQW active region. The 3D nanorod structure leads to an expanded active area, with a greater degree of integration than typical 2D planar structures on the same substrate size owing to 3D geometry. Consequently, we call this phenomenon the "large-junction-area effect". Even though we do not consider the degree of light extraction (or absorption) in this study, the need for this effect is apparent, particularly for the applications based on light absorption such as solar cells and optoelectronic sensors.[35, 36]

5.3.5 Structural investigation of InGaN/GaN MQW core-shell nanorod

In order to investigate structural characteristics, the GaN nanorod based coaxial structure

was inspected using by scanning of a cross-sectional HR-TEM. We found that MQWs were clearly formed on the GaN nanorod sidewall and on slanted facets corresponding to the $\{1\bar{1}00\}$ and $\{1\bar{1}01\}$ planes of wurtzite GaN, as shown in Fig. 5.8 (a). The high-resolution TEM images shown in Figs. 5.8 (b) – (e) clearly indicated that MQWs formed on the three different oriented facets of GaN nanorods. As shown in Fig. 5.8 (b), the MQW layer acted as a quantum-dot-like structure along the *c*-direction. Ko *et al.* reported similar results for the features of 1D, 2D, and 3D MQWs structure on a nanopyramid GaN array.[37] We consider that the feature of 1D MQW is attributed to dotlike existence of (0002) *c*-plane in GaN nanorod as shown in Fig. 5.2 (a). According to previous results, MQW properties such as crystal orientation, thickness, and composition are determined by the surface energy of the basal GaN crystal planes.[30, 38] Because of the indistinct crystal orientation of the topmost facets of the GaN nanorods, the group III species appear to agglomerate with the adjacent boundary layer on the apex of the GaN nanorod. Figure 5.8 (c) shows the thickness of the MQWs on the *m*-plane GaN nanorod sidewall. From this TEM image, we can obviously confirm the existence of alternately stacked multiple layers. The QW and QB thicknesses were measured to be about 2 and 8 nm, respectively. This MQW on the GaN nanorod *m*-plane can ensure efficient radiative recombination in order to capture electrons and holes. On the other hand, the thickness of the MQW on the $\{1\bar{1}01\}$ plane is lessened considerably less than that of the $\{1\bar{1}00\}$ facet MQW as shown in Fig. 5.8 (d). The dark and bright layers of the MQWs on the $\{1\bar{1}01\}$ plane are very difficult to distinguish and we consider that this MQWs is too thin for effective light emission. This is due to the low growth rate of the $\{1\bar{1}01\}$ facets. Typically, the growth rate of the $\{1\bar{1}01\}$ facets was less than half that of the $\{1\bar{1}00\}$ plane.[30, 38] As mentioned before, this anisotropic growth rate of GaN may be a critical factor for
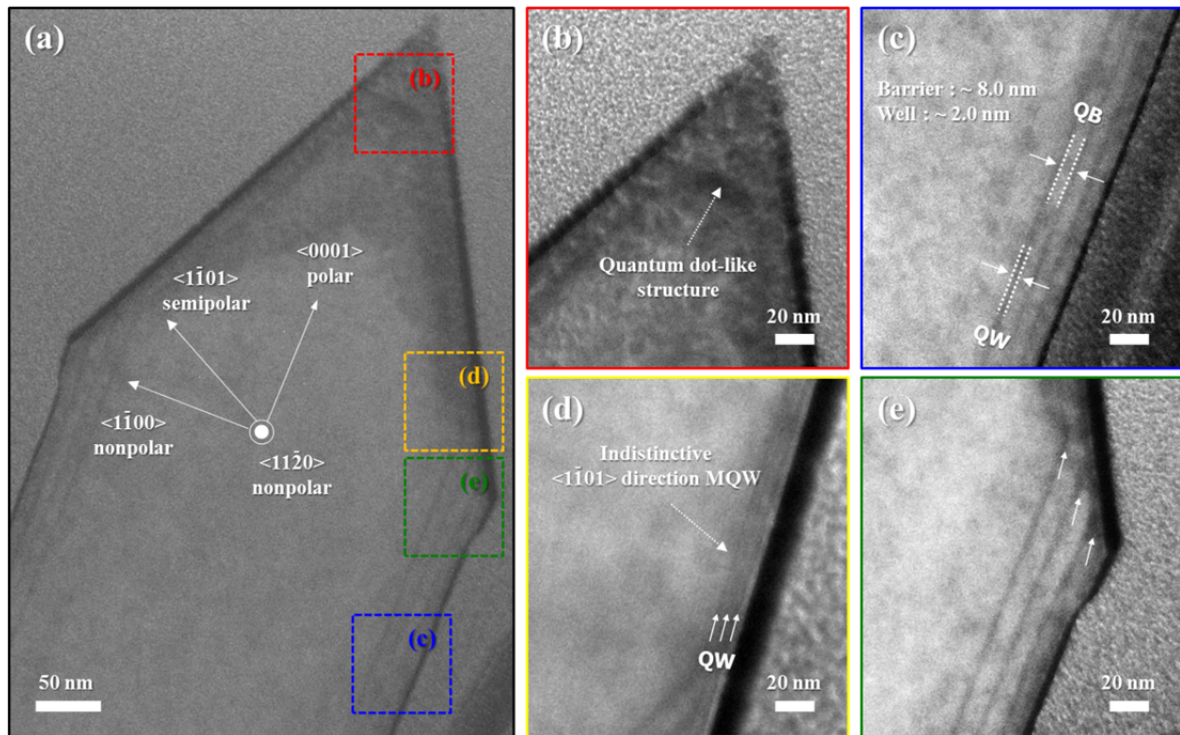
Figure 5.8. The TEM images of In$_x$Ga$_{1-x}$N/GaN MQWs on different facets of GaN nanorod. The bright contrast indicates the GaN QB layer, and the dark contrast signifies the InGaN QW layer. (a) High-magnification TEM image. The three arrows show the crystal orientation of the GaN nanorod. The squares indicates the regions from which enlarged TEM images were captured from different positions (b – e) of the coaxial nanorod. (b) TEM image exhibiting a quantum-dot-like structure on the (0001) c-plane. (c) Three periods of MQWs are clearly formed on the nonpolar m-plane sidewall. (d) Indistinct QW and QB layers are formed on the $\{1\bar{1}01\}$ semipolar plane. (e) The MQWs are formed on the edge region between the $\{1\bar{1}01\}$ semipolar and $\{1\bar{1}00\}$ nonpolar planes.

controlling the indium composition in the QW layer. Consequently, the formation of appropriate QW and QB thicknesses on both nonpolar and semipolar planes of GaN nanorod core for effective light emission from both $\{1\bar{1}00\}$ and $\{1\bar{1}01\}$ planes simultaneously is

expected to be difficult. Although, the semipolar plane can affect the device performance, the low growth rate caused by the stability of the $\{1\bar{1}01\}$ plane may be advantageous in terms of achieving monochromatic spectral emission. Also, we consider that the high aspect ratio of GaN nanorods can minimize or remove the effect of the semipolar plane because the *m*-plane light emission intensity is much higher than that of the semipolar plane. Figure 5.8 (e) shows the edge between the nonpolar $\{1\bar{1}00\}$ and semipolar $\{1\bar{1}01\}$ planes. As we discussed in Fig. 5.6 (b), the edge region of the nanorod has achieved relatively higher indium composition in comparison with *m*-plane. We consider that different indium incorporation rate at the edge region on the GaN nanorod may be dependent on the gas-phase diffusion process.[39] In addition, as shown in Figs. 5.8 (c) and (e), the edge place of the nanorod has relatively thicker QW and QB layers than the other region of the GaN nanorod *m*-plane. This phenomenon is probably due to the inter-plane diffusion of group III species between the semipolar and nonpolar facets. It can be found from the average lifetime of the atoms during epi-growth to mainly depend on their reaction behavior or growth rate on the surface.

5.4 Summary

● The Ga-polar GaN nanorod based InGaN/GaN MQW coaxial nanoarchitecture arrays were successfully grown by selective area MOCVD, and we investigated the structural and optical properties of MQW coaxial nanoarrays by TEM, PL, and CL measurements.

● According to the TEM cross-sectional investigation, the MQWs were formed anisotropically on GaN nanorods owing to the different growth rates of the oriented GaN planes. The average growth rate of the MQWs depended on the basal facet and decreased in the order (0001) polar > $\{1\bar{1}00\}$ nonpolar > $\{1\bar{1}01\}$ semipolar.

● The MQWs have a quantum-dot-like island structure on the *c*-plane caused by the dotlike (0002) plane at the GaN nanorod tip. In addition, the MQWs on the $\{1\bar{1}01\}$ semipolar plane could hardly be observed in the TEM images owing to the very low InGaN (QW) and GaN (QB) growth rates.

● The light emission was also hardly observed from the MQWs on polar and semipolar facets by CL mapping measurement. On the other hand, the MQWs mostly grew uniformly on the entire nonpolar $\{1\bar{1}00\}$ *m*-plane. The thicknesses of the QW and QB layer on the *m*-plane of the GaN nanorod sidewall were 2.0 and 8.0 nm, respectively.

● Furthermore, the light emission efficiency was improved by extending the area of the *m*-plane on the GaN nanorod. The results of CL mappings suggest that extending the $\{1\bar{1}00\}$ nonpolar *m*-plane can enhance the light emission properties by increasing the degree of integration on the substrate.

● We consider that GaN nanorod based InGaN/GaN MQWs coaxial nanoarchitecture arrays can play an important role in next-generation LEDs for energy saving such as to prevent efficiency droop, achieve high efficiency, and low power consumption.

5.5 References

1) F. A. Ponce, D. P. Bour; Nature **386**, 351 (1997).

2) H. Amano, N. Sawaki, I. Akasaki, Y. Toyoda; Appl. Phys. Lett. **48**, 353 (1986).

3) J. Wu, W. Walukiewicz, K. M. Yu, J. W. Ager, E. E. Haller, H. Lu, W. J. Schaff, Y. Saito, Y. Nanishi; Appl. Phys. Lett. **80**, 3967 (2002).

4) I. Akasaki, H. Amano; J. Electrochem. Soc. **141**, 2266 (1994).

5) I. Akasaki, H. Amano; Jpn. J. Appl. Phys. **36**, 5393 (1997).

6) H. Lahreche, P. Vennegues, O. Tottereau, M. Laugt, P. Lorenzini, M. Leroux, B. Beaumont, P. Gibart; J. Cryst. Growth **217**, 13 (2000).

7) J. H. Choi, A. Zoulkarneev, S. I. Kim, C. W. Baik, M. H. Yang, S. S. Park, H. Suh, U. J. Kim, H. B. Son, J. S. Lee; Nat. Photon. **5**, 763 (2011).

8) S. Y. Lee, K.-I. Park, C. Huh, M. Koo, H. G. Yoo, S. Kim, C. S. Ah, G. Y. Sung, K. J. Lee; Nano Energy **1**, 145 (2012).

9) F. Bernardini, V. Fiorentini, D. Vanderbilt; Phys. Rev. B **56**, 10024 (1997).

10) C. Wetzel, M. Zhu, J. Senawiratne, T. Detchprohm, P. D. Persans, L. Liu, E. A. Preble, D. Hanser; J. Cryst. Growth **310**, 3987 (2008).

11) M.-H. Kim, M. F. Schubert, Q. Dai, J. K. Kim, E. F. Schubert, J. Piprek, Y. Park; Appl. Phys. Lett. **91**, 183507 (2007).

12) K. J. Vampola, M. Iza, S. Keller, S. P. DenBaars, S. Nakamura; Appl. Phys. Lett. **94**, 061116 (2009).

13) B. H. Kong, B. O. Jung, H. K. Cho, G. Yoo, O. Nam; Thin Solid Films **544**, 244 (2013).

14) H. Amano; Jpn. J. Appl. Phys. **52**, 050001 (2013).

15) B. A. Haskell, A. Chakraborty, F. Wu, H. Sasano, P. T. Fini, S. P. Denbaars, J. S. Speck, S. Nakamura; J. Electron. Mater. **34**, 357 (2005).

16)   R. Kucharski, M. Rudzinski, M. Zajac, R. Doradzinski, J. Garczynski, L. Sierzputowski, R. Kudrawiec, J. Serafinczuk, W. Strupinski, R. Dwilinski; Appl. Phys. Lett. **95**, 131119 (2009).

17)   B. H. Kong, H. K. Cho, K. M. Song, D. H. Yoon; J. Cryst. Growth **313**, 8 (2010).

18)   Y. S. Cho, Q. Sun, I. H. Lee, T. S. Ko, C. D. Yerino, J. Han, B. H. Kong, H. K. Cho, S. Wang; Appl. Phys. Lett. **93**, 111904 (2008).

19)   Z. Liliental-Weber; J. Cryst. Growth **310**, 4011 (2008).

20)   C.-H. Lee, J. Yoo, Y. J. Hong, J. Cho, Y.-J. Kim, S.-R. Jeon, J. H. Baek, G.-C. Yi; Appl. Phys. Lett. **94**, 213101 (2009).

21)   R. Colby, Z. Liang, I. H. Wildeson, D. A. Ewoldt, T. D. Sands, R. E. García, E. A. Stach; Nano Lett. **10**, 1568 (2010).

22)   C. F. Huang, T. Y. Tang, J. J. Huang, W. Y. Shiao, C. C. Yang, C. W. Hsu, L. C. Chen; Appl. Phys. Lett. **89**, 051913 (2006).

23)   B. O. Jung, S.-Y. Bae, Y. Kato, M. Imura, D.-S. Lee, Y. Honda, H. Amano; CrystEngComm **16**, 2273 (2014).

24)   E. Le Boulbar, I. Girgel, C. Lewins, P. Edwards, R. Martin, A. Šatka, D. Allsopp, P. Shields; J. Appl. Phys. **114**, 094302 (2013).

25)   D. Tham, C. Y. Nam, J. E. Fischer; Adv. Funct. Mater. **16**, 1197 (2006).

26)   T. Gotschke, T. Schumann, F. Limbach, T. Stoica, R. Calarco; Appl. Phys. Lett. **98**, 103102 (2011).

27)   S. Y. Bae, J. Y. Lee, J. H. Min, D. S. Lee; Appl. Phys. Express **6**, 075501 (2013).

28)   G. Jacopin, A. D. L. Bugallo, P. Lavenus, L. Rigutti, F. H. Julien, L. F. Zagonel, M. Kociak, C. Durand, D. Salomon, X. J. Chen; Appl. Phys. Express **5**, 014101 (2012).

29)   Y.-H. Ra, R. Navamathavan, H.-I. Yoo, C.-R. Lee; Nano Lett. **14**, 1537 (2014).

30)   Y. J. Hong, C. H. Lee, A. Yoon, M. Kim, H. K. Seong, H. J. Chung, C. Sone, Y. J. Park,

G. C. Yi; Adv. Mater. **23**, 3284 (2011).

31)   M. A. Reshchikov, H. Morkoç; J. Appl. Phys. **97**, 061301 (2005).

32)   S. D. Hersee, X. Sun, X. Wang; Nano Lett. **6**, 1808 (2006).

33)   E. C. Garnett, P. Yang; J. Am. Chem. Soc. **130**, 9224 (2008).

34)   B. O. Jung, D. C. Kim, B. H. Kong, D.-W. Kim, H. K. Cho; Sens. Actuators B **160**, 740 (2011).

35)   C. Soci, A. Zhang, B. Xiang, S. A. Dayeh, D. Aplin, J. Park, X. Bao, Y.-H. Lo, D. Wang; Nano Lett. **7**, 1003 (2007).

36)   B. Tian, X. Zheng, T. J. Kempa, Y. Fang, N. Yu, G. Yu, J. Huang, C. M. Lieber; Nature **449**, 885 (2007).

37)   Y. H. Ko, J. H. Kim, L. H. Jin, S. M. Ko, B. J. Kwon, J. Kim, T. Kim, Y. H. Cho; Adv. Mater. **23**, 5364 (2011).

38)   C.-H. Liao, W.-M. Chang, H.-S. Chen, C.-Y. Chen, Y.-F. Yao, H.-T. Chen, C.-Y. Su, S.-Y. Ting, Y.-W. Kiang, C. C. Yang; Opt. Express **20**, 15859 (2012).

39)   H. Fang, Z. Yang, Y. Wang, T. Dai, L. Sang, L. Zhao, T. Yu, G. Zhang; J. Appl. Phys. **103**, 014908 (2008).

Chapter 6

Core-shell nanorods embedded 3D light-emitting diode (LED)

6.1 Background

III-Nitride based materials are promising as an energy-saving solid-state lighting source, particularly for light-emitting diodes (LEDs) to save energy for human life. There has been significant technological development in the field of nitride-based solid-state lighting over the past few decades since the discovery of the low temperature buffer growth technique and a method of magnesium activation.[1, 2] Although considerable improvements in the performance of LED devices have been demonstrated *c*-plane polar gallium nitride (GaN)-based LEDs still have unsolved problems that adversely affect their performance, which are caused by piezoelectric and spontaneous polarization.[3, 4] To resolve such problems, the different crystal planes, particularly nonpolar facets such as *m*- and *a*- planes, can be applied to the $In_xGa_{1-x}N$/GaN multiple-quantum-well (MQW) heteroepitaxial structure as basal facets.[3] LED structures based on nonpolar facets are expected to avoid the piezoelectric-field-related issue such as efficiency droop. However, in the case of using *m*-plane bulk substrate, this increases the cost of devices. Moreover, the nonpolar-plane-based heteroepilayer between *a*-plane GaN and *r*-plane sapphire still needs to prevent the formation of structural defects such as prismatic and basal stacking faults or partial dislocations to ensure sufficient crystal quality.[5, 6] In fact, the results of research based on GaN nanorods and nanowires have produced advances and interesting outcomes in a number of application fields.[7-9] Among them, the selective area growth (SAG) of GaN nanorods is a particularly promising alternative for producing nonpolar-based LED structures without increasing the production cost of devices or introducing structural defects owing to their unique characteristics. Although GaN-nanorod-based structures have a high potential for LED

development, only limited research can be accomplished towards the ultimate aim of realizing three-dimensional (3D) LED device. In other words, the reported light emission and electrical properties must still be improved to realize 3D-LED structures. In particular, the GaN-nanorod-based LED structure has three different crystal facets, in contrast to the GaN planar epi-structure. This means that the light emission behavior of core-shell nanorods can exhibit interesting properties in combination with the different light emission behaviors caused by MQWs on different GaN crystal facets. Therefore, we report the fabrication and characteristics of GaN-nanorod-based $In_xGa_{1-x}N/GaN$ MQW core-shell nanorod arrays embedded in a 3D-LED structure. To clarify the underlying physics of this core-shell structure, we investigate its structural properties, particularly the well and barrier thicknesses of the MQWs, by Cs-corrected scanning transmission electron microscopy (Cs-corrected STEM). We also performed measurements of temperature (T) and excitation power (P) dependences of the photoluminescence (PL) to reveal their optical properties by analyzing the behaviors of the emission energy, intensity, and linewidth. Additionally, light emission properties of the core-shell nanorods-embedded 3D-LED structure is also presented in detail.

6.2 Experimental section

6.2.1 Preparation of pattern

A 3-μm-thick GaN epi-layer with a (0002) preferential orientation dope with Si was utilized as a basal template for the SAG of GaN nanorods by metalorganic chemical vapor deposition (MOCVD). The RF magnetron sputtering was used to deposit of a 30-nm-thick dielectric SiO_2 growth masking layer. After SiO_2 deposition, nanoscale patterns (aperture size: 190 nm; center-to-center distance: 920 nm) were produced by thermal nanoimprinting procedure (T-NIP). Then, CF_4-based reactive-ion etching (RIE) was performed to open the SiO_2 selectively. Subsequently, the patterning template was cleaned with an organic solvent

(acetone) for 10 min to eliminate polymer-based residual nanoimprinting resin on the surface.

6.2.2 Synthetic process and 3D-LED fabrication

For the growth of GaN nanorod arrays, $In_xGa_{1-x}N$/GaN MQW core-shell nanorods, and the core-shell nanorods embedded 3D-LED structure, the SiO_2/GaN/sapphire template was loaded into a showerhead-type MOCVD chamber. Trimethylgallium (TMGa), ammonia (NH_3), and tetramethylsilane ((CH_3)$_4$Si) were used as the precursors and n-type doping sources with flow rates of 15 sccm (78 μmol/min), 5 slm (223.21 mmol/min), and 5 sccm (0.0105 μmol/min), respectively. The synthesis of well-defined GaN nanorod arrays was carried out in accordance with Hersee's original pulsed-mode growth procedure with our optimal growth condition under an ambient of pure hydrogen (H_2) as the carrier gas. Details of this pulsed-mode growth process have been given in previous chapter of this thesis.[10, 11] Subsequently, three pairs of $In_xGa_{1-x}N$/GaN MQWs were grown on the GaN nanorod arrays by in a conventional growth mode at temperatures from 760 to 790 °C depending on the experiment. For MQW growth, trimethylindium (TMI) and triethylgallium (TEG) were used as reactants with nitrogen (N_2) as the carrier gas. The reactant flow rates of TMI and TEG were fixed at 400 sccm (40.3 μmol/min) and 100 sccm (29.92 μmol/min), respectively, with a chamber pressure of 200 Torr. Finally, p-type GaN was grown with bis-ethylcyclopentadienyl magnesium (EtCp2Mg) as a precursor at a flow rate in the range of 150-250 sccm (0.24-0.4 μmol/min) for 90 min to ensure full coalescence. To form ohmic contacts, Ti/Au (150/50 nm) and Ni/Au (150/50 nm) bilayer metals were deposited by electron beam evaporation onto the n-GaN underlayer and p-GaN top surface layer, respectively. To decrease the resistance between the metal and the semiconductor (GaN), the metal contacts were treated by rapid thermal annealing (RTA) at 550 and 300 °C after the deposition of n-GaN and p-GaN bilayer metals, respectively. The detailed schematic of the 3D-LED structure was shown in Fig 6.1.
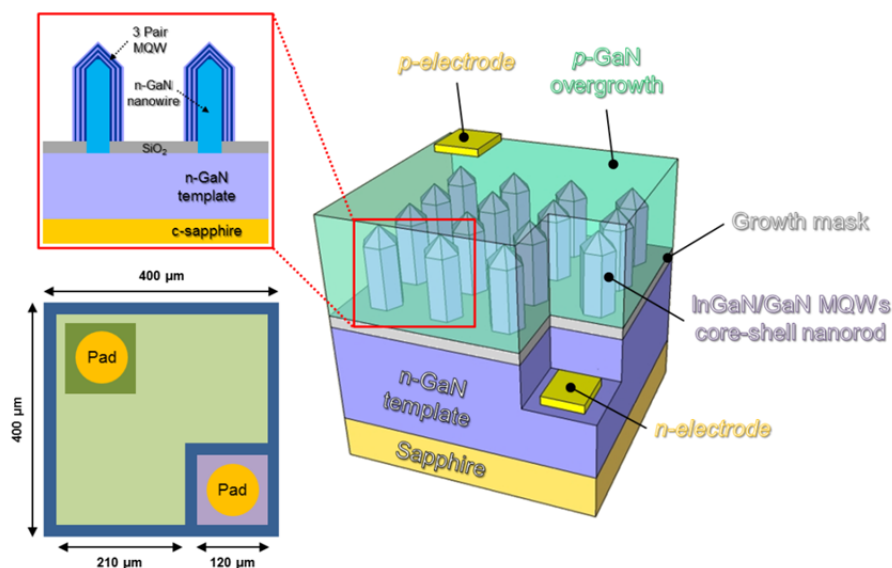
Figure 6.1 Schematics of the InGaN/GaN MQW core-shell nanorod embedded 3D-LED structure. The expanded schematic displays the detailed MQWs structure of InGaN/GaN core-shell nanorods.

6.2.3 Characterizations

Morphological and microstructural characterizations were carried out by field-emission scanning electron microscopy (FE-SEM, Hitachi S-5200) and Cs-corrected STEM (JEM-ARM200F) operated at 300 kV, respectively. The synthesized samples were milled using a dual-beam focused ion beam (DB-FIB, NOVA200) operating in the range of 5-30 kV before TEM investigation to obtain high-resolution (HR), bright-field (BF), and electron diffraction pattern (DP) images. To investigate the emission properties of the $In_xGa_{1-x}N$/GaN core-shell nanorod arrays, temperature dependence of the PL was measured as a function of temperature from 12 to 300 K in a closed cycle-helium cryostat. The excitation power dependence of the PL was measured in the power density range of 7.6-764 W/cm^2. For all the PL measurements, a 325 nm continuous-wave He-Cd laser (20 mW) was used as the excitation source, and the objective lens (x5) of a reflecting microscope was used to control the beam spot size (~20 μm) and simultaneously collect the signal. In this chapter, we define the maximum excitation

power density (= 764 W/cm^2) as 100%. Moreover, the characterizations of the electrical properties (*I-V* curve) and electroluminescence (EL) spectra of the 3D-LED were performed simultaneously.

6.3 Core-shell architecture embedded 3D-LED

6.3.1 Surface morphology and optical properties of GaN nanorod and its based InGaN/GaN MQW core-shell nanorods

Figure 6.2 shows the room-temperature PL spectra and each inset FE-SEM image indicates the surface morphology of selective-area-grown GaN nanorod arrays and three pairs In$_x$Ga$_{1-x}$N/GaN MQWs core-shell nanorods. The PL spectrum of the GaN nanorod arrays displays typical behaviors. A strongly dominant ultraviolet (UV) emission peak located at approximately 365 nm was observed as shown in Fig. 6.2 (a). This intense UV peak is closely related to the recombination of free excitons, i.e., the near-band-edge (NBE) emission of the GaN crystal.[1] Furthermore, we observed hardly any defect-related yellow luminescence (YL) at approximately 550 nm wavelength, indicating the high optical and crystal quality of the GaN nanorod array. After the heteroepitaxial growth of three pairs of In$_x$Ga$_{1-x}$N/GaN MQWs, the structural morphology of the coaxial nanorod arrays still maintained its verticality, selectivity, and uniformity as shown in the inset of Fig. 6.2 (b). The MQW light emission peak at approximately 445 nm dominates the optical characteristics of the PL spectrum in Fig. 6.2 (b). As before, no YL-related emission is generated, indicating high optical quality of the In$_x$Ga$_{1-x}$N/GaN MQWs core-shell nanorod arrays. From these results, we expect that the dominant light emission of nanorod arrays will mainly originate from the MQWs on nonpolar {1$\bar{1}$00} *m*-plane sidewalls. This will be discussed in the next section on the basis of detailed structural and optical analysis results.
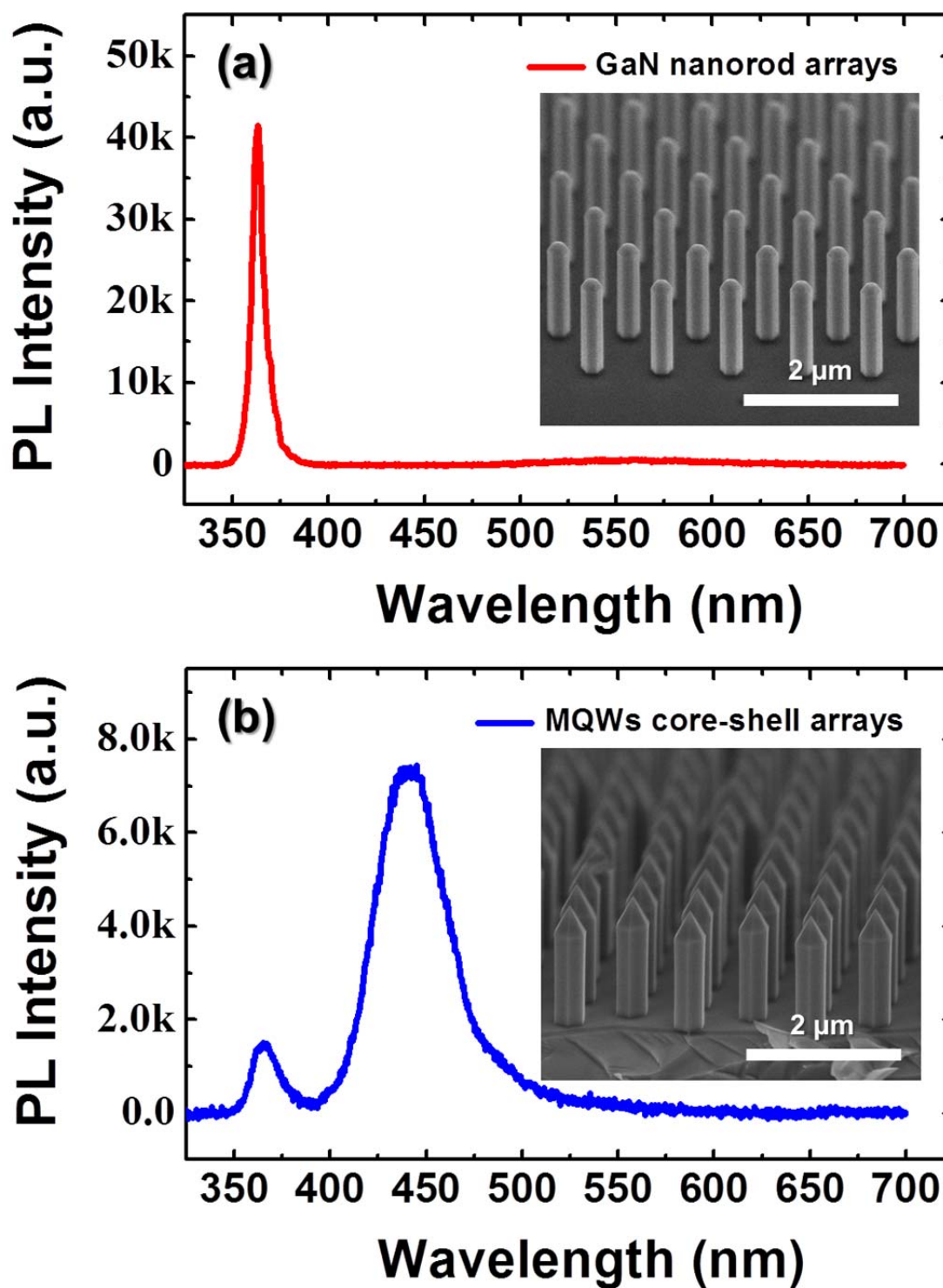
Figure 6.2 (a) Room-temperature PL spectrum and SEM image (inset) of selective-area-grown GaN nanorod array. (b) Room-temperature PL spectrum and SEM image (inset) of the core-shell nanorod array including the three pairs of InGaN/GaN MQWs.

6.3.2 TEM investigation
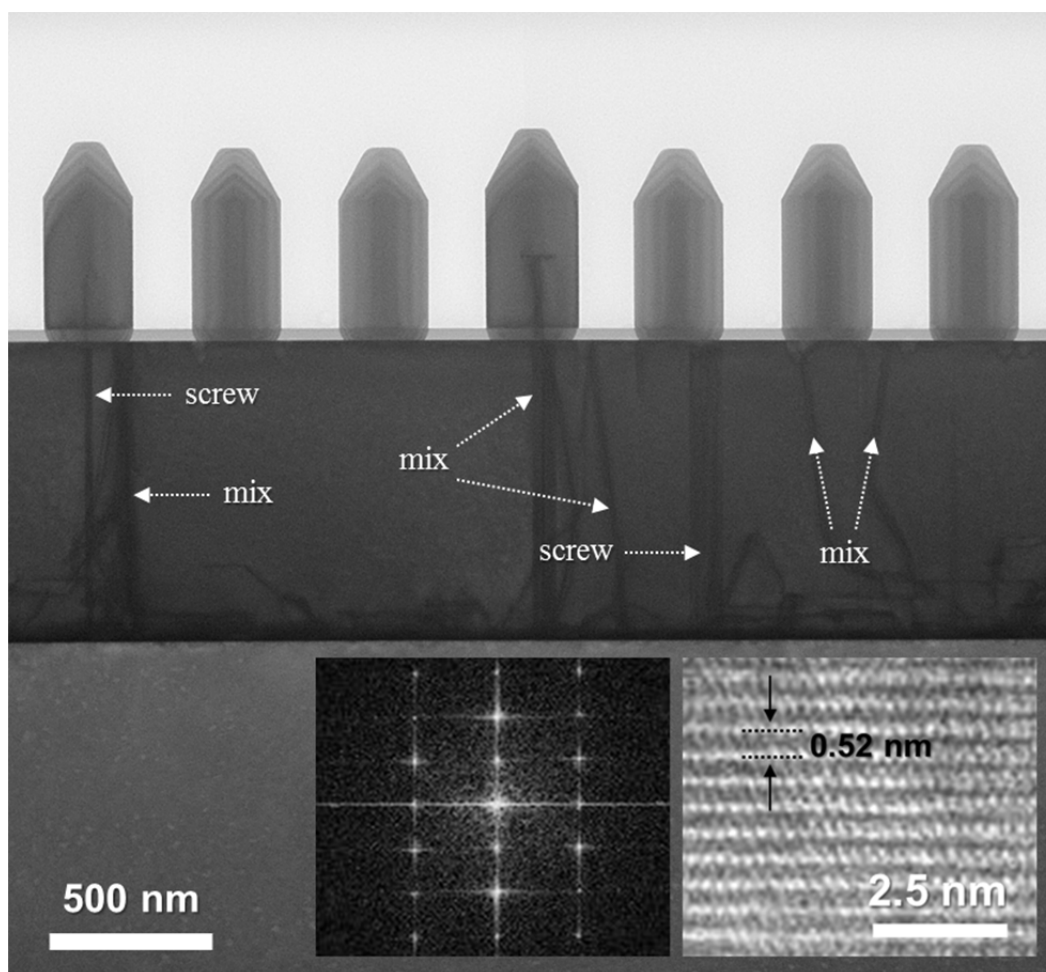
Figure 6.3 Cross-sectional STEM image of GaN nanorods showing the penetration and filtering of dislocation into the GaN nanorods. The HR image indicates the single-crystalline property of a GaN nanorod. The Fourier-filtered transformed (FFT) diffraction pattern (DP) was obtained from the HR image of a GaN nanorod.

Figure 6.3 shows various outcomes of the cross-sectional TEM investigation such as low and high-magnification BF, DP, and HR images of GaN nanorod arrays. This investigation shows a low-magnification cross-sectional STEM image of a selective-area-grown *n*-GaN nanorods on a thick GaN underlayer captured in the [11$\bar{2}$0] zone-axis. As shown in this figure, there are a few dislocations caused by the lattice mismatch between GaN underlayer and the

sapphire substrate such as screw and mixed dislocations. Nevertheless, we clearly observed that most dislocations were filtered by the SiO_2 masking, and very few dislocations penetrated the inner core of the *n*-GaN nanorods. This phenomenon leading to defect-free nanorods can be described by the filtered dislocation effect model of nanoscale epitaxy.[12] We also confirmed the single-crystalline wurzite properties of the *n*-GaN nanorods by DP and HR analyses, as shown in the inset of Fig. 6.3. Consequentially, we can expect the dislocation-free and highly crystalline of GaN nanorods.
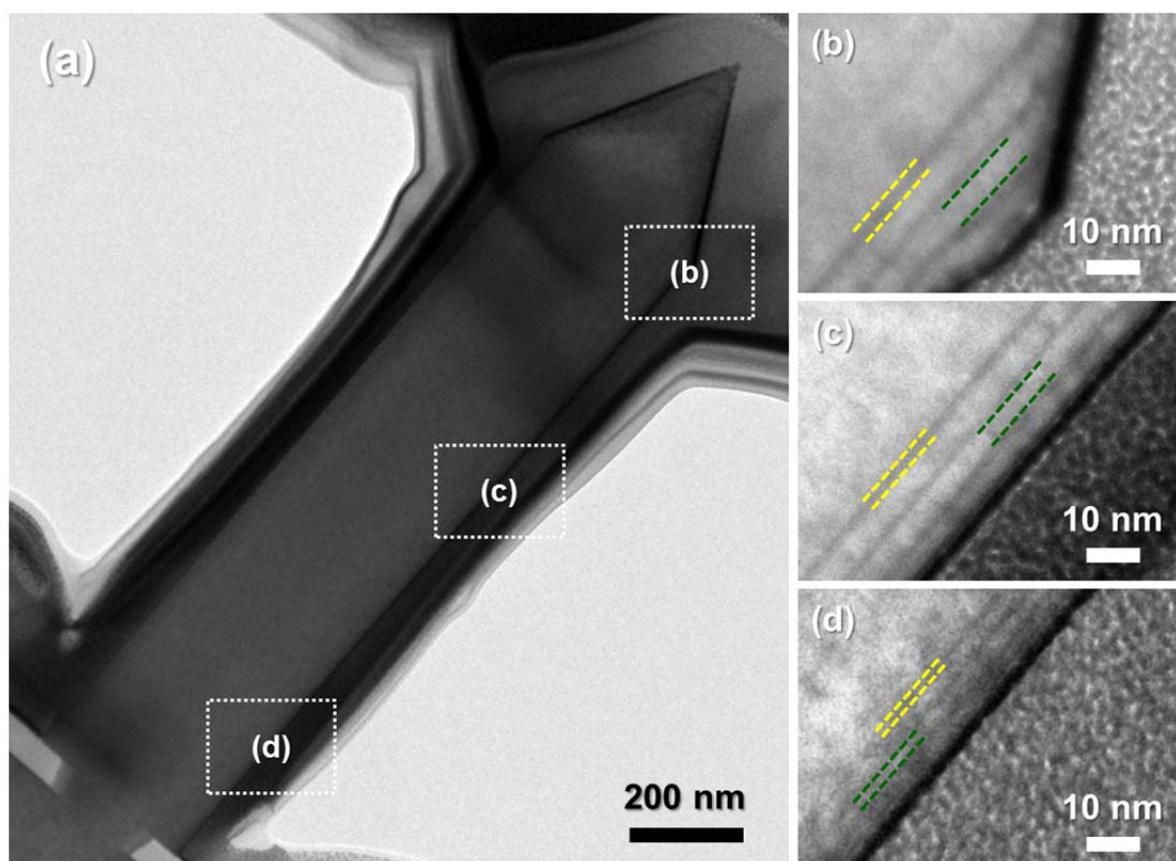

Figure 6.4 (a) Cross-sectional STEM image of the InGaN/GaN MQWs based single core-shell nanorod under low magnification. The squares display the regions from which enlarged STEM images were obtained. (b) – (d) Thicknesses of QWs and QBs at different positions of the core-shell nanorod.

The low-magnification STEM image in figure 6.4 (a) shows that the $In_xGa_{1-x}N$/GaN MQWs were coated uniformly on nonpolar $\{1\bar{1}00\}$ *m*-plane sidewalls of the outside of the *n*-GaN nanorod. Figs. 6 (b) − (d) show the high-magnification STEM images to examine the features of grown MQWs on *n*-GaN nanorods, where we mainly focus on the structural properties of the MQWs on nonpolar $\{1\bar{1}00\}$ *m*-plane sidewalls. The MQWs on the $\{1\bar{1}00\}$ *m*-plane sidewalls of the outside of the *n*-GaN nanorod were clearly stacked into dark (InGaN quantum well: QW) and bright (GaN quantum barrier: QB) layers as shown in Fig. 6.4 (b) − (d). Altogether the MQW structure on the outside of the *n*-GaN nanorod has a reasonably consistent multiple stack layer however, the QW and QB thickness have a little bit different thicknesses according to position of core-shell nanorod partially. At upper positions, the MQWs thicknesses are thicker than those at lower positions even in the same crystal facet. In other words, the thickness of the MQWs tends to increase from the bottom to the top of the core-shell nanorods. In particular, the thickness of MQWs is greatest at the edge region interface between $(1\bar{1}00)$ and $(1\bar{1}01)$ facets. This phenomenon may be related to the surface diffusion process in combination with the mean lifetime of the group III adatoms.[13] Although the MQW thickness varies slightly with the position on the core-shell nanorod, effective light emission is expected to be generated from the $\{1\bar{1}00\}$ *m*-plane sidewalls undoubtedly. However, we suggest that there is potential for interesting optical properties to be generated by varying the well and barrier thicknesses. This will be discussed in detail in next section on the basis of the results of PL analysis. Even though these MQW layers on the *n*-GaN nanorods have a small thickness variation, we expect that the MQWs can induce effective radiative recombination between electrons and holes from the MQWs on nonpolar $\{1\bar{1}00\}$ *m*-plane sidewalls regardless of their thickness.

6.3.3 Optical characterization of InGaN/GaN MQW nanorod arrays

Figure 6.5 shows the peak energy, centroid peak energy, and full width at half maximum (FWHM) plotted as functions of the percentage excitation laser power (10 – 100%) at low and high temperatures, i.e, 12 K (Fig. 6.5(a)) and 300 K (Fig. 6.5(b)). It should be noted that we used the centroid peak energy to reflect the net shift of the broad PL, as is evident from the well-thickness observation. With increased excitation laser power, almost no peak energy shift was observed at both low and high temperatures, showing the absolute reduction of the Quantum-confined Stark effect (QCSE), which is related to internal electric field (IEF), as a result of local epitaxy.[14, 15] The centroid peak energy also exhibits blueshifts of only 1.9 and 4.6 meV at the temperatures of 12 and 300 K, respectively. At the same time, a slight decrease of linewidth (the same as the FWHM in this communication) of as small as 3 meV was observed at 12 K. Generally, there are two possible mechanisms explaining the dependence of the blueshift behavior on the PL excitation power density: one is Coulomb screening of the QCSE and the other is band filling of localized states.[16, 17] The former usually shows a linewidth narrowing, but the latter shows a linewidth broadening.[16, 18] In our case, it is speculated that the band filling of localized states become the dominant process of nanorod (NR)-based QWs with increasing excitation power at 12 K since the IEF almost disappears. Moreover, the well-width variation has less of an effect than the emission energy shift, but strongly impacts spectrum broadening. Hence, we believe that the small decrease of linewidth is attributed to the well-width variation, thereby following the effect of the energy transition due to the simultaneous filling of carriers in the strongly localized states. On the other hand, we observed a large increase of linewidth when the excitation power was increased from 10 – 25% at 300 K, since the linewidth remained almost constant (Fig 6.5 (b)). The initial peak broadening can be attributed to the dominance of thermally activated nonradiative recombination centers at the high temperature since they enable excited carriers

to be readily recombined at high-energy extended states before reaching low-energy localized states.[17] With further increasing excitation power, radiative recombination became dominant after the rapid saturation of nonradiative centers, but the linewidth remained almost constant with a slight increase in centroid peak energy. Therefore, we believe that a similar shading phenomenon of the band filling effect was observed as discussed for Fig. 6.5 (a).
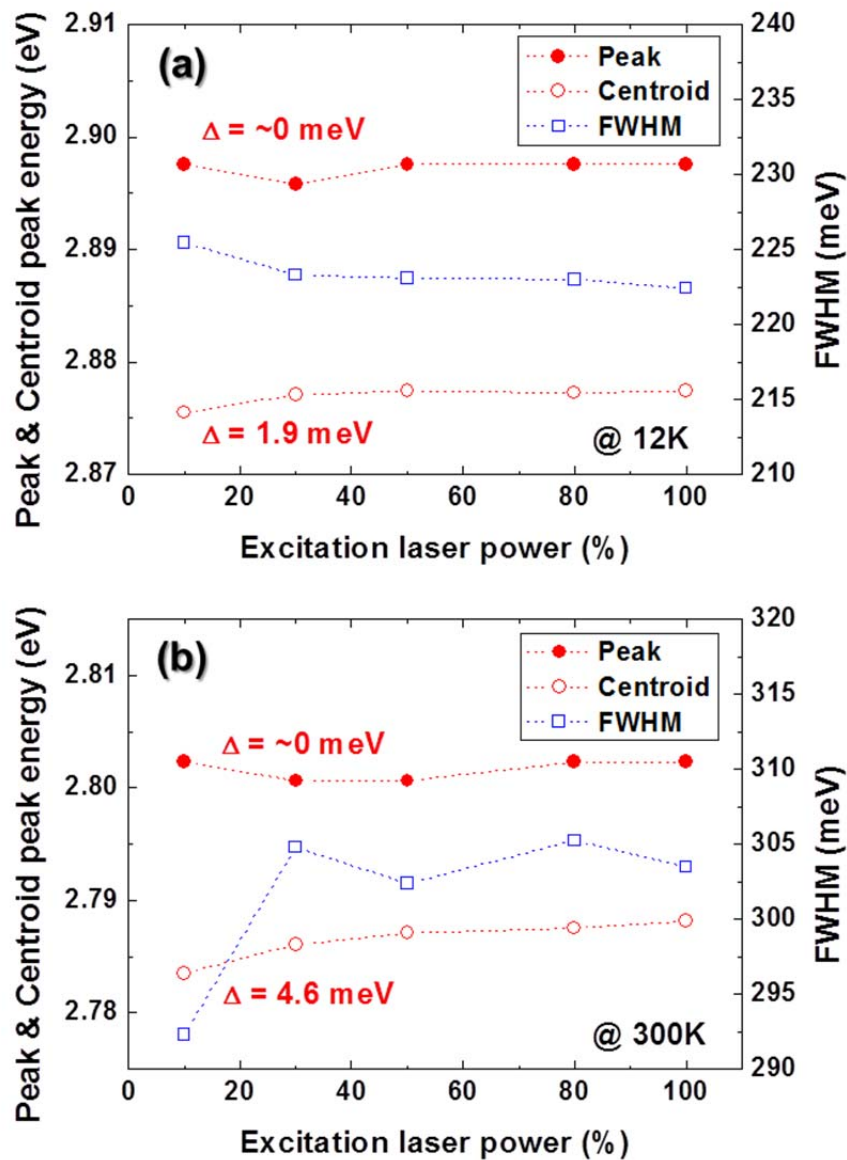
Figure 6.5 Excitation laser power dependence of PL emission peak energy, centroid peak energy, and linewidth (FWHM) at (a) 12 K and (b) 300 K.
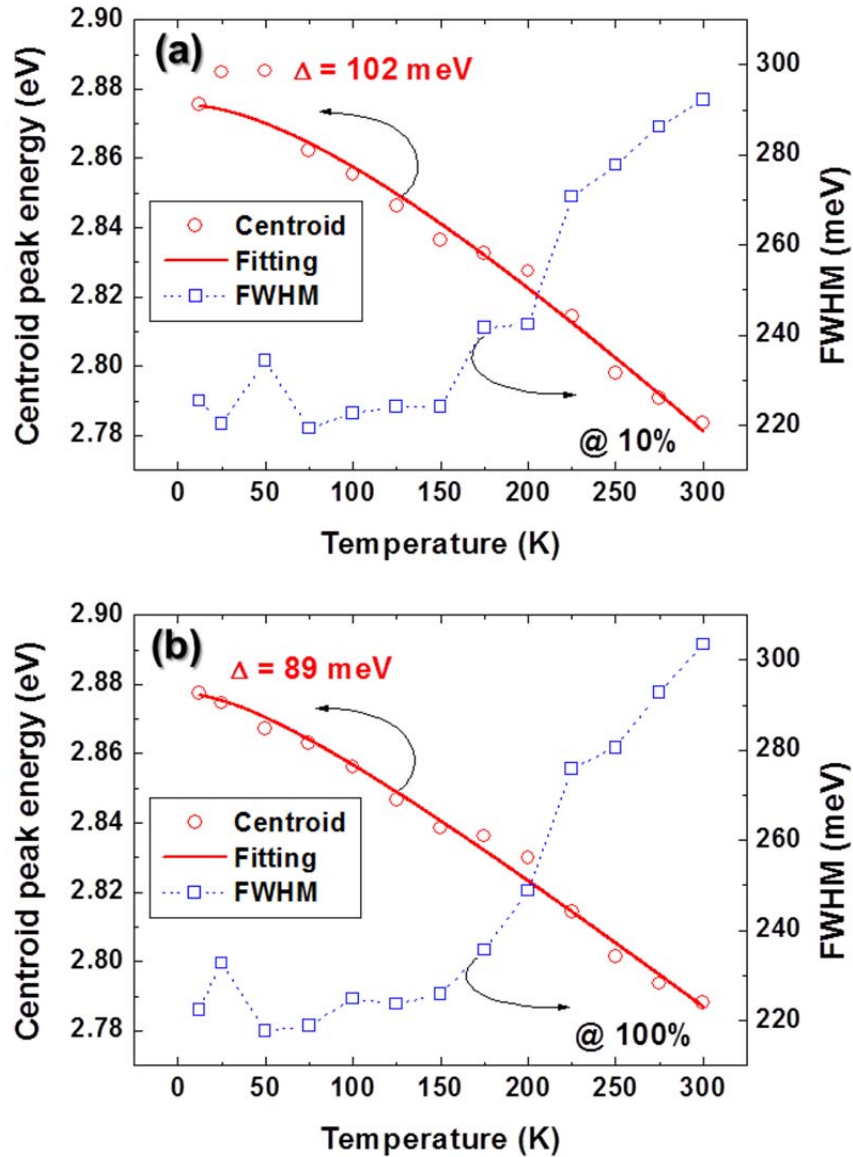
Figure 6.6 Temperature dependence of PL emission centroid peak energy and linewidth (FWHM) for excitation powers of (a) 10% and (b) 100%. The red solid lines represent the curves fitted using Varnish's model.

Figure 6.6 plots temperature dependences of the centroid peak energy and FWHM for low and high excitation power densities, i.e., 10% (Fig. 6.6 (a)) and 100% (Fig. 6.6 (b)). For an excitation power density of 10%, the centroid peak first undergoes a blueshift up to a temperature of ~50 K, since then it undergoes a continuous redshift, whilst a slight reflection

curve is observed at the full-delocalization temperature of ~175 K. It should be noted that *c*-plane InGaN QWs typically exhibit an *S*-shaped peak shift (decrease-increase-decrease) and a corresponding W-shaped curve (decrease-increase-decrease-increase) for the FWHM.[17, 18] Regardless of the significant difference in peak shift behavior between typical *c*-plane InGaN QWs and NR-based QWs, the linewidth of the NR-based QWs has a similar temperature dependence compared to that of *c*-plane InGaN QWs. The linewidth slightly decreases up to a temperature of 25 K, and then increases up to a temperature of 50 K, which is similar to the temperature of the highest centroid peak energy. Furthermore, it decreases up to a temperature of 75 K, and then the linewidth steadily increases up to 300 K. Hence, it clearly shows a W-shaped temperature dependence. To explain in detail the different temperature dependences of the peak shift for conventional *c*-plane InGaN QWs and NR-based QWs, it is necessary to understand the possible carrier transferring mechanisms. We notice that the excitation carrier density is sufficiently low since it is corresponded to < 1000 W/cm^2. In general, at low temperatures from 12 to 50 K has been considered to be the carrier hopping dominant mechanism, indicating that weakly localized carriers can become thermally activated and relax into other strongly localized states caused by inhomogeneous potential fluctuations.[19] The slight narrowing of the linewidth is also evidence of this redistribution of weakly localized carriers.[18] In the NR structures, however, the well-width variation of the InGaN QWs was observed, as is evident from Fig. 6.4 (b) – (d). Hence, it is speculated that the initial blueshift of as large as 10 meV for the NR-based QWs in the temperature range of 12 – 50 K is due to the anti-Stokes luminescence generated by the two-step absorption process, i.e., photon recycling, since there are overlapping states between the weakly localized state at a low energy level and the strongly localized state at a high energy level.[20, 21] As the temperature increased from 50 K, a large redshift of the centroid peak energy was observed. In fact, large blueshift have been observed for *c*-plane InGaN QWs in a similar

temperature range (60 – 150K) since thermally enabled carriers can occupy the higher-energy levels of the localized states.[17, 18] Hence, the NR-based QWs should also follow this band filling process in the same temperature range. However, in the NR-based QWs, it can be raised on multiple localized states owing to the well-width variation, as discussed for Fig. 6.4. As a consequence, the band-filling effect, i.e., the blueshift behavior can be weakened. This is consistent with the slope of 0.35 meV/K found for the temperature range of 75 – 150 K, compared with 0.45 meV/K for the temperature range of 200 – 300 K. In general, the redshift becomes dominant with increasing temperature owing to the temperature-dependent dilatation of the lattice and the electron-lattice interaction.[22, 23] This temperature-induced redshift of the peak energy can be described by Varshni's empirical model $E(T) = E(0) - \alpha T^2 / (T + \beta)$, where $E(0)$ is the energy gap at 0 K, and α and β are fitting parameters.[24] The red solid lines in Fig. 6.6 (a) are the fitting curves obtained using Varshni's model with $E(0) = 2.877$ eV, $\alpha = 0.39$ meV, and $\beta = 89$ K. The fitting curves closely match the experimental except in the initial temperature range of 12 – 50 K. Meanwhile, The small increase and decrease of linewidth in the temperature range of 25 – 75 K can be assigned to the crossover from the nonthermalization to thermalization of localized excitons (increase) and to the further redistribution of mobile carriers (decrease).[25, 26] The slow increase of the linewidth as large as 5 meV in the temperature range of 75 – 150 K indicates that the change of linewidth caused by carrier thermalization is screened by the overlapping of the localized states due to well-width variation. At 175 K, a gentle slope in the centroid energy and an abrupt increase of linewidth were observed, indicating that it almost reached to free-exciton ground state. Then, the temperature-induced bandgap shrinkage became more dominant, thereby a steeper slope of the peak energy shift and linewidth broadening were observed. On the other hand, the temperature dependence of the PL results under at the higher excitation power density (100 %) is plotted in Fig. 6.6 (b). The biggest difference was found at the low temperatures (< 50 K),

where a monotonic redshift of the centroid peak energy was observed. It is believed that a high excitation power density enables a sufficient number of injected carriers to occupy both weakly localized states and strongly localized states, for the carrier hopping effect to be reduced. Hence, the decrease of linewidth observed at the same temperature at an excitation power density of 10% was not observed at the higher excitation power density. Furthermore, the temperatures of rising and falling peak in linewidth were shifted ahead by ~25 K owing to the increase in injected carrier density in the strongly localized states. Above 75 K, the redshift of the centroid peak energy and the linewidth broadening behaviors were quite similar to those observed at 10% of PL excitation, where the same carrier relaxation mechanism could be proved. Note that the slope variation was found to be 0.33 eV/K at 75 – 150 K and 0.42 eV/K at 200 – 300 K, also indicating the small effect of band-filling on the peak shift behavior. The curve fitted using Varshni's model was also in good agreement with the experimental results, as shown by the red solid line in Fig. 6.6 (b). The total amount of energy shift over the entire temperature range was slightly reduced from 102 to 89 meV upon increasing the PL excitation power density.

6.3.4 Realization of 3D-LED

We fabricated the 3D-LED by *p*-GaN overgrowth on InGaN/GaN MQW core-shell nanorods. The properties of this 3D-LED structure were investigated by EL and current-voltage (*I-V*) characterizations. Figure 6.7 (a) shows the EL spectra for various injection current levels. The dominant EL emission wavelength was observed to be 500 nm at 1 mA, corresponding to the near-green region. However, the EL emission was shifted to the blue region with a slight shoulder peak when the injection current was increased to 20 mA, which is related to the dissimilar MQW layers on the different crystal facets of the GaN nanorod caused by the current injection path.[7, 10] The light emission of the MQWs mainly originates
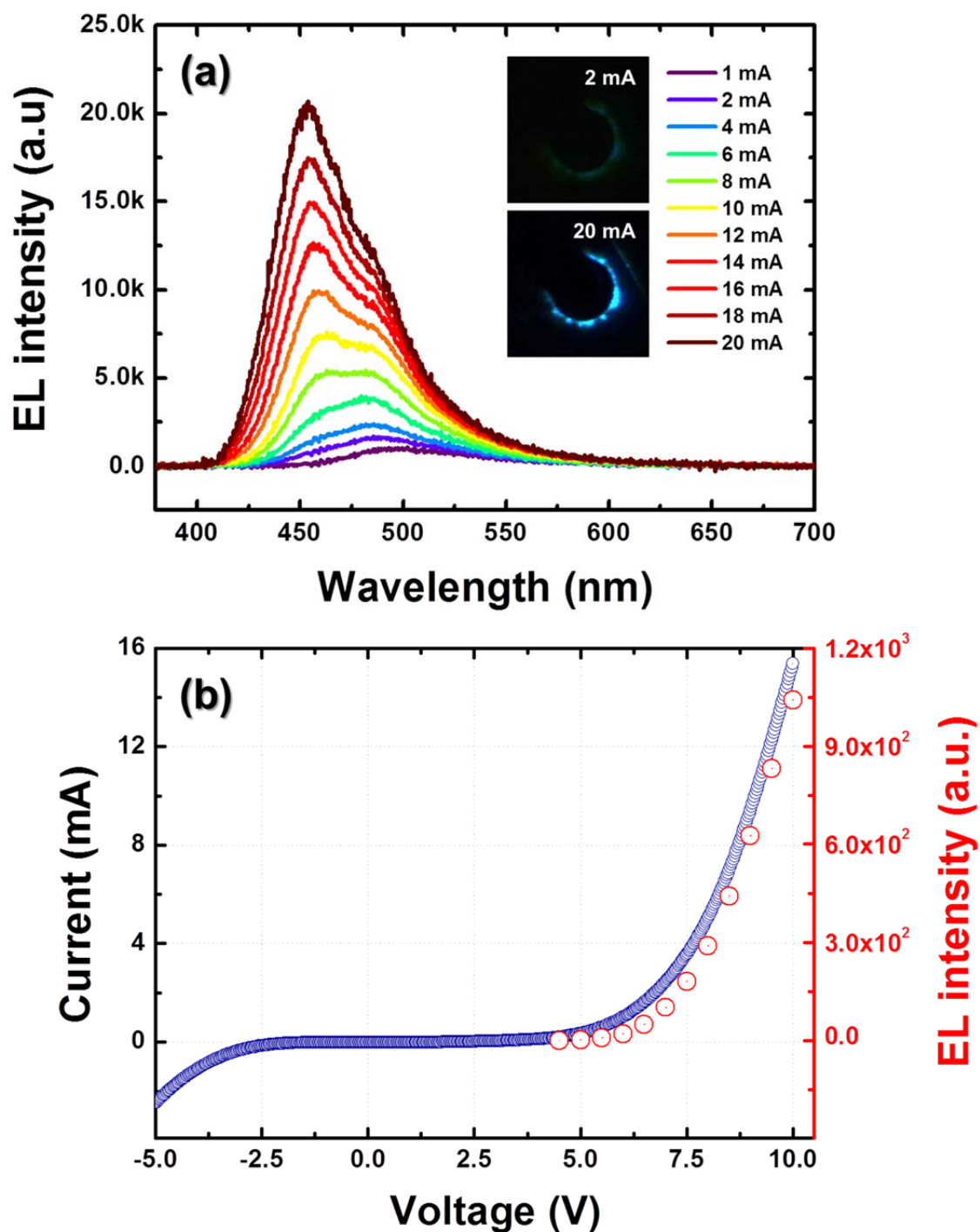
Figure 6.7 (a) EL spectra of the InGaN/GaN MQW core-shell nanorod embedded 3D-LED obtained at various injection currents from 1 to 20 mA. The insets are photographs of the light emission. (b) *I-V* characteristic curve of the MQW core-shell embedded 3D-LED.

from the upper region of the GaN nanorod particularly the edges between the semipolar and $\{1\bar{1}00\}$ nonpolar facets owing to the high resistivity of p-GaN at a low applied bias. However, the injected carriers can overcome the high resistivity of p-GaN when the applied bias is increased. As a result, light emission can be induced from the MQWs on the $\{1\bar{1}00\}$ nonpolar sidewalls of the GaN nanorods. In fact, the peak EL emission wavelength did not show a significant shift above 14 mA, as shown in Fig. 6.7 (a), indicating the dominant light emission from the MQWs on the $\{1\bar{1}00\}$ nonpolar sidewalls.[27, 28] We confirmed the *I-V* characteristics of the core-shell nanorod embedded 3D-LED as shown in Fig. 6.7 (b). The *I-V* curve shows the general rectifying phenomenon of the LED with a turn-on voltage of approximately 6 V. The current began to rise rapidly above the turn-on voltage according to applied bias, resulting in enhanced light emission intensity. Also, the leakage current was observed to be approximately 2 mA at −5 V. Two possibilities may account for the leakage current the unsuccessful growth of GaN nanorods within the nanopattern and a current path though semipolar plane.[27] Therefore, we consider that the leakage problem can be eliminated by employing a suitable patterning process or optimizing the growth conditions such as MQW thickness, p-GaN doping concentration with the thickness, aspect ratio of the core-shell nanorod, and so forth.

6.4 Summary

● In summary, we have demonstrated and analyzed GaN-nanorod-based In$_x$Ga$_{1-x}$N/GaN MQWs core-shell nanorods and its embedded the 3D-LED structure.

● An HR-TEM investigation revealed that the InGaN/GaN MQWs formed on the GaN nanorods had different characteristics depending on their position on the GaN nanorods.

● The luminescence properties of InGaN/GaN MQWs core-shell nanorods were measured by excitation and temperature-dependent PL analysis. In the excitation power dependence of the PL result, slight decrease of linewidth was observed at 12 K, which was attributed to the well-width variation, whereas the broadening of a small the linewidth at 300 K may have been related to the dominance of thermally activated nonradiative recombination centers.

● Also, the shift of the centroid peak showed a different behavior depending on the excitation power density, particularly at low temperature ranges (< 50 K) which is attributed to different occupy of injected carriers in both weakly and strongly localized states caused by excitation power density.

● Furthermore, the color of EL emitted by the fabricated 3D-LED changed with the injected current. This is attributed to the dissimilar MQW properties resulting from different crystal facets of the GaN nanorod.

● Nevertheless, the MQWs on the $\{1\bar{1}00\}$ nonpolar planes of GaN nanorods play a dominant role in light emission in the case of enhanced current injection.

● We believe that this 3D-LED will enable the realization of effective lighting devices with a controlled emission color.

6.5 References

1)   I. Akasaki, H. Amano, Y. Koide, K. Hiramatsu, N. Sawaki; J. Cryst. Growth **98**, 209 (1989).

2)   S. Nakamura, T. Mukai, M. Senoh, N. Iwasa; Jpn. J. Appl. Phys. **31**, L139 (1992).

3)   C. Wetzel, M. Zhu, J. Senawiratne, T. Detchprohm, P. Persans, L. Liu, E. Preble, D. Hanser; J. Cryst. Growth **310**, 3987 (2008).

4)   M.-H. Kim, M. F. Schubert, Q. Dai, J. K. Kim, E. F. Schubert, J. Piprek, Y. Park; Appl. Phys. Lett. **91**, 183507 (2007).

5)   B. H. Kong, H. K. Cho, K. M. Song, D. H. Yoon; J. Cryst. Growth **313**, 8 (2010).

6)   J.-S. Son, Y. Honda, M. Yamaguchi, H. Amano, K. H. Baik, Y. G. Seo, S.-M. Hwang; Thin Solid Films **546**, 108 (2013).

7)   Y. J. Hong, C. H. Lee, A. Yoon, M. Kim, H. K. Seong, H. J. Chung, C. Sone, Y. J. Park, G. C. Yi; Adv. Mater. **23**, 3284 (2011).

8)   M. Ebaid, J.-H. Kang, S.-H. Lim, J.-S. Ha, J. K. Lee, Y.-H. Cho, S.-W. Ryu; Nano Energy **12**, 215 (2015).

9)   L. Goren-Ruck, D. Tsivion, M. Schvartzman, R. Popovitz-Biro, E. Joselevich; ACS Nano **8**, 2838 (2014).

10)   B. O. Jung, S.-Y. Bae, S. Y. Kim, S. Lee, J. Y. Lee, D.-S. Lee, Y. Kato, Y. Honda, H. Amano; Nano Energy **11**, 294 (2015).

11)   B. O. Jung, S.-Y. Bae, Y. Kato, M. Imura, D.-S. Lee, Y. Honda, H. Amano; CrystEngComm **16**, 2273 (2014).

12)   R. Colby, Z. Liang, I. H. Wildeson, D. A. Ewoldt, T. D. Sands, R. E. García, E. A. Stach; Nano Lett. **10**, 1568 (2010).

13)   H. Fang, Z. Yang, Y. Wang, T. Dai, L. Sang, L. Zhao, T. Yu, G. Zhang; J. Appl. Phys.

103, 014908 (2008).

14) H. Yu, L. Lee, T. Jung, P. Ku; Appl. Phys. Lett. **90**, 141906 (2007).

15) T. Kim, J. Kim, M.-S. Yang, S. Lee, Y. Park, U.-I. Chung, Y. Cho; Appl. Phys. Lett. **97**, 241111 (2010).

16) Y.-J. Lee, C.-H. Chiu, C. C. Ke, P. C. Lin, T.-C. Lu, H.-C. Kuo, S.-C. Wang; IEEE J. Sel. Top. Quantum Electron. **15**, 1137 (2009).

17) Y.-H. Cho, G. Gainer, A. Fischer, J. Song, S. Keller, U. Mishra, S. DenBaars; Appl. Phys. Lett. **73**, 1370 (1998).

18) H. Wang, Z. Ji, S. Qu, G. Wang, Y. Jiang, B. Liu, X. Xu, H. Mino; Opt. Express **20**, 3932 (2012).

19) D. Monroe; Phys. Rev. Lett. **54**, 146 (1985).

20) R. Hellmann, A. Euteneuer, S. Hense, J. Feldmann, P. Thomas, E. Göbel, D. Yakovlev, A. Waag, G. Landwehr; Phys. Rev. B **51**, 18053 (1995).

21) A. Satake, Y. Masumoto, T. Miyajima, T. Asatsuma, T. Hino; Phys. Rev. B **61**, 12654 (2000).

22) H. Fan; Phys. Rev. **82**, 900 (1951).

23) K. O'Donnell, X. Chen; Appl. Phys. Lett. **58**, 2924 (1991).

24) Y. Varshni; Physica **34**, 149 (1967).

25) K. Kazlauskas, G. Tamulaitis, A. Žukauskas, M. Khan, J. Yang, J. Zhang, G. Simin, M. Shur, R. Gaska; Appl. Phys. Lett. **83**, 3722 (2003).

26) K. Kazlauskas, G. Tamulaitis, P. Pobedinskas, A. Žukauskas, M. Springis, C.-F. Huang, Y.-C. Cheng, C. Yang; Phys. Rev. B **71**, 085306 (2005).

27) H.-S. Chen, Y.-F. Yao, C.-H. Liao, C.-G. Tu, C.-Y. Su, W.-M. Chang, Y.-W. Kiang, C. Yang; Opt. Lett. **38**, 3370 (2013).

28) M. Tchernycheva, P. Lavenus, H. Zhang, A. V. Babichev, G. Jacopin, M.

Shahmohammadi, F. H. Julien, R. Ciechonski, G. Vescovi, O. Kryliouk; Nano Lett. **14**, 2456 (2014).

Chapter 7

Conclusions and future works

7.1 Conclusion

This thesis started with the hypothesis that the position-controlled selective area growth (SAG) of gallium nitride (GaN) nanorod structures fabricated by a bottom-up growth technique can be utilized as a useful architecture for light-emitting diodes (LEDs). The growth, fabrication, and characterization of GaN nanorods, InGaN/GaN multiple-quantum-well (MQW) core-shell nanorod arrays, and a three-dimensional (3D) LED device with embedded core-shell nanorods were reported. Pulsed-mode metalorganic chemical vapor deposition (MOCVD) growth technique was applied for the SAG of GaN nanorods. Selective-area-grown GaN nanorods, GaN nanorod based InGaN/GaN MQWs core-shell nanorods, and 3D-LED structures based on such nanorods were successfully demonstrated. The structural, physical, and optical characteristics of these structures were investigated using numerous analysis tools. The conclusions of this thesis are given below.

The suitability of pulsed-mode MOCVD growth for the position-controlled SAG of GaN nanorod arrays was examined. Selective-area-grown GaN nanorod arrays were achieved with selectivity, uniformity, and regularity with their dominant geometry along the (0001) c-axis. The morphological transition could be controlled through the precursor injection and interruption durations. For the optimized pulsed-mode growth conditions such as the temperature, the flow rate of the precursors, the working pressure, and so forth, a longer Ga injection duration allows a higher growth rate along the lateral direction. In addition, a longer N injection duration leads to the formation of a hexagonal pyramidal structure on the surface due to the overlap of Ga and N adatoms. Nevertheless, the morphology of the grown GaN

nanorods could be controlled by applying a suitable interruption duration in the case of longer precursor injection times. The appropriate duration to achieve the nanorod architecture was explained by pulsed-mode growth ratio (PMGR).

The effect of typical growth conditions in the pulsed-mode growth procedure was also investigated with the aim optimizing the growth conditions for the SAG of GaN nanorods. The vertical growth rate was enhanced and the lateral growth rate was suppressed by increasing the growth temperature regardless of the TMGa flow rate. On the other hand, both the vertical and lateral growth rates were prompted by increasing the TMGa flow rate independent of the growth temperature. These dependences of the growth behavior on the growth variables are related to the variation of the surface phenomena of Ga atoms such as adsorption, desorption, and diffusion behaviors caused by growth conditions. In addition, the results for the SAG of GaN nanorods depended on the pattern design of the growth mask.

The polarity of GaN nanorods was found to be Ga-polar from convergent-beam electron diffraction (CBED) patterns obtained by high-resolution transmission electron microscopy (HR-TEM). Also, a number of dislocations generated in the GaN underlayer were filtered by the growth mask, hence the selective-area-grown GaN nanorods could have characteristic of dislocation-free. As a result, they showed high crystallinity and good optical quality such as an intense ultraviolet (UV) emission peak located at approximately 365 nm. In addition, the defect-related yellow luminescence (YL) properties could be controlled via the N injection duration.

Highly ordered GaN nanorod based InGaN/GaN MQW core-shell nanorod arrays were fabricated by heteroepitaxial growth. The MQWs were formed anisotropically on GaN nanorods owing to the different growth rates of the oriented GaN planes. The average growth rate of the MQWs depended on the basal facet and decreased in the order (0001) polar > {1$\bar{1}$

00} nonpolar > {1$\bar{1}$01} semipolar. Furthermore, the high-quality InGaN/GaN MQW core-shell nanorods enabled improved light emission intensity combined with expended {1$\bar{1}$00} sidewall surface area of the GaN nanorods. The results of cathodoluminescence (CL) measurement suggest that extending the {1$\bar{1}$00} nonpolar *m*-plane can enhance the light emission properties by increasing the degree of integration on the substrate. In addition, the optical properties of the InGaN/GaN MQW core-shell nanorods were examined in more detail by analysis of the excitation power and temperature dependences of photoluminescence (PL). In the excitation power dependence of PL, the slight decrease of the linewidth at low temperatures is attributed to the well-width variation, whereas the broadening of the linewidth at room temperature may be related to the dominance of thermally activated nonradiative recombination centers. Also, the centroid peak shifts in a different manner depending on the excitation power density, particularly at low temperature range (<50 K), which is attributed to differentrate of occupation of injected carriers within both weakly and strongly localized states caused by excitation power density.

A InGaN/GaN MQW core-shell nanorod embedded 3D-LED structure was successfully fabricated by *p*-GaN overgrowth. This 3D-LED structure exhibited a rectifying diode phenomenon and near-green light emission first occurred at an injected current of ~1 mA. The light emission was sufficiently intense to be clearly viewed by the unaided eye at a low injected current. The light emission intensity was enchanced and blue emission was observed upon increasing the injected current. This color-tunable property is closely related to the current path within *p*-GaN. We expect that the position-controlled SAG of GaN nanorod arrays and InGaN/GaN core-shell nanoarrays including 3D-LED structure based on GaN nanorods by MOCVD will enable the fabrication of numerous novel optoelectronic devices.

7.2 Future works

Although a few LED device structures based on core-shell nanorod arrays have been demonstrated in this thesis, more important challenges remain in the realization of high-brightness 3D-LEDs. (i) First, the patterning process for position control should be further improved by optimizing the process conditions to decrease the area of unsuccessful growth. (ii) Second, the growth conditions of p-GaN should be optimized to obtain a mirrorlike surface morphology to improve the metal contact. (iii) Finally, a well-established fabrication process or a new type of 3D structure should be applied to improve the device performance. Therefore, future works should concentrate on solving these issues. For example, a metal-mask-based nanoimprint process can ameliorate the quality of patterning outcome. Moreover, an AlGaN layer should be inserted for p-GaN growth. This barrier will protect the InGaN QWs and help to increase the growth temperature of p-GaN, which is expected to reduce the surface roughness. Separate core-shell nanorod structures with a transparent conducting oxide (TCO) layer such as indium tin oxide (ITO) or aluminum zinc oxide (AZO) can have the potential to improve the output performance of 3D-LEDs structure. The realization of 3D-LEDs should enable the development of many optoelectronic devices in the upcoming future.

- LIST OF ACHIEVEMENTS -

September, 2015

Byung Oh Jung

Nagoya University

Graduate School of Engineering

Department of Electrical Engineering and Computer Science

A. Science Citation Index (SCI) International Journal Publications (* : Corresponding author)

01) "Highly-ordered catalyst-free InGaN/GaN core-shell architecture array with expanded active area region" **Byung Oh Jung***, Si-Young Bae, Sang Yun Kim, Seunga Lee, Jeong Yong Lee, Dong-Seon Lee, Yoshihiro Kato, Yoshio Honda, and Hiroshi Amano, *Nano energy* **11, 294 (2015)**.

02) "Morphology development of GaN nanowires using pulsed-mode MOCVD growth technique", **Byung Oh Jung***, Si-Young Bae, Yoshihiro Kato, Masataka Imura, Dong-Seon Lee, Yoshio Honda, and Hiroshi Amano, *CrystEngComm* **16, 2273 (2014)**.

03) "All oxide ultraviolet photodetectors based on p-Cu_2O film/n-ZnO heterostructure nanowires" Yul Ho Ok, Ki Ryong Lee, **Byung Oh Jung**, Yong Hyun Kwon, and Hyung Koun Cho*, *Thin Solid Films* **570, 282 (2014)**.

04) "Nonpolar a-GaN epilayers with reduced defect density using patterned r-plane sapphire substrates", Bo Hyun Kong, **Byung Oh Jung**, Hyung Koun Cho*, Jong Jin Jang, and Ok Hyun Nam, *Thin Solid Films* **544, 244 (2013)**.

05) "Semi-transparent all-oxide p-NiO/n-ZnO nanowire ultraviolet photosensors", Ki Ryong Lee, **Byung Oh Jung**, Sung Woon Cho, Karuppanan Senthil, and Hyung Koun Cho*, *J. Mater. Res.* **28, 2605 (2013)**.

06) "Ultraviolet light emitting diode based on p-NiO/n-ZnO nanowires heterojunction",

Byung Oh Jung, Yong Hun Kwon, Dong Ju Seo, Dong Seon Lee, and Hyung Koun Cho*, *J. Cryst. Growth* **370, 314 (2013)**.

07) "High-Purity ultraviolet electroluminescence from *n*-ZnO nanowires/p^+-Si heterostructure LEDs with *i*-MgO film as carrier control layer", **Byung Oh Jung**, Ju Ho Lee, Jeong Yong Lee, Jae Hyun Kim, and Hyung Koun Cho*, *J. Electrochem. Soc.* **159, H102 (2012)**.

08) "Highly sensible ZnO nanowire ultraviolet photodetectors based on mechanical schottky contact", Dong Chan Kim, **Byung Oh Jung**, Yong Hun Kwon, and Hyung Koun Cho*, *J. Electrochem. Soc.* **159, K10 (2012)**.

09) "Fully transparent vertically aligned ZnO nanostructure-based ultraviolet photodetectors with high responsivity", **Byung Oh Jung**, Dong Chan Kim, Bo Hyun Kong, Dong Wook Kim, and Hyung Koun Cho*, *Sens. Actuators B* **160, 740 (2011)**.

10) "Direct formation of transparent ITO top electrodes on high-density ZnO nanowires by magnetron sputtering", **Byung Oh Jung**, Dong Chan Kim, Bo Hyun Kong, Ju Ho Lee, Jeong Yong, Lee, and Hyung Koun Cho*, *Electrochem. Solid-State Lett.* **14, H446 (2011)**.

11) "Dramatically enhanced ultraviolet photosensing mechanism in a *n*-ZnO nanowires/*i*-MgO/*n*-Si structure with highly dense nanowires and ultrathin MgO layers", Dong Chan Kim, **Byung Oh Jung**, Ju Ho Lee, Hyung Koun Cho*, Jeong Yong Lee, and Jun Hee Lee, *Nanotechnology* **22, 265506 (2011)**.

12) "The effects of growth temperature on structural and emission properties of ZnO nanorod arrays grown by low-temperature metalorganic chemical vapor deposition", Mi Kyung Choi, **Byung Oh Jung**, Bo Hyun Kong, and Hyung Koun Cho*, *J. Ceram. Process. Res.* **12, s233 (2011)**.

B. International Conference Presentations (* : Presenter)

01) "Optimal Growth Condition in Pulsed-mode MOVPE Process for Selective Area Growth of GaN Nanorod Arrays and Its Based 3D-LED Structure" **Byung Oh Jung***, Si-Young Bae, Masataka Imura, Yoshio Honda, and Hiroshi Amano, *ICMAT2015 & IUMRS-ICA2015*, ICMAT15-A-0982, Jul. 02, 2015, Suntec, Singapore

02) "Selective Area Growth of GaN Nanorods on Si (111) Grown by Pulsed-Mode MOCVD" Si-Young Bae*, **Byung Oh Jung**, Kaddour Lekhal, Dong-Seon Lee, Yoshio Honda, and Hiroshi Amano, *The 2015 E-MRS (European Materials Research Society) Spring Meeting*, I-7 4, May 12, 2015, Lille, France

03) "Optical Characterization and Structural Investigation of GaN Nanorod Arrays and its Based InGaN/GaN MQWs Core-Shell Nanoarchitecture Arrays" **Byung Oh Jung***, Si-Young Bae, Seunga Lee, Sang Yun Kim, Masataka Imura, Yoshio Honda, and Hiroshi Amano, *2015 MRS (Materials Research Society) Spring Meeting & Exhibit*, S3.06, Apr. 07, 2015, San Francisco, USA

04) "Selective area grown GaN nanowire based InGaN/GaN MQWs coaxial array : structural characterization and luminescent properties", **Byung Oh Jung***, Si-Young Bae, Sang Yun Kim, Dong-Seon Lee, Yoshio Honda, Hiroshi Amano, *2014 MRS (Materials Research Society) Fall Meeting & Exhibit*, LL5.22, Dec. 01, 2014, Boston, USA

05) "Morphology Control of GaN-based Nano-LEDs Grown by Pulsed-mode MOCVD Epitaxy and its Material/Optical Chracterization" Si-Young Bae*, Jun-Yeob Lee, **Byung Oh Jung**, Jung-Hong Min, Dong-Seon Lee, Yoshihiro Kato, Masataka Imura, Yoshio Honda, Hiroshi Amano, *ENGE 2014 (International Conference on Electronic Materials and Nanotechnology for Green Environment)*, Nov. 17, 2014, Jeju, Korea

06) "Study of Ga-polar GaN nanowire arrays formation mechanism using pulsed-mode MOVPE growth technique", **Byung Oh Jung***, Si-Young Bae, Dong-Seon Lee, Yoshio Honda, Hiroshi Amano, *ISGN5 - 5th International Symposium on Growth of III-Nitrides*, J15, May. 20, 2014, Atlanta, USA

07) "Multidimensional p-NiO/n-ZnO nanowire based light emitting diodes showing pure ultraviolet emission", **Byung Oh Jung***, Yong Hun Kwon, Hyung Koun Cho, *ISSLED 2012 - 9th International Symposium on Semiconductor Light Emitting Devices*, P1-23, Jul. 23, 2012, Berlin, Germany

08) "Nonpolar a-GaN epilayers with reduced defect density using patterned r-plane sapphire substrates", Bo Hyun Kong, **Byung Oh Jung***, Hyung Koun Cho, Jong Jin Jang, Ok Hyun Nam, *Thin Films 2012*, ODF-2113, Jul. 15, 2012, SMU, Singapore

09) "Fabrication of *n*-ZnO Nanowire / *p*-NiO Multidimensional Ultraviolet Photodetectors Grown by Metalorganic Chemical Vapor Deposition", **Byung Oh Jung***, Yong Hun Kwon, Bo Hyun Kong, Hyung Koun Cho, *ICMOVPE - XVI*, TuP-60, May. 22, 2012, Busan, Korea

10) "Development of ZnO/MgO/p^+-Si heterostructures for pure UV light emitting diode with carrier blocking layer", **Byung Oh Jung***, Dong Chan Kim, Ju Ho Lee, Jeong Yong Lee, Ho Seong Lee, Hyung Koun Cho, *TMS 2012 Annual Meeting - The Minerals, Metals & Materials Society*, p14, Mar. 12, 2012, Orlando, USA

11) "Formation of multidimensional transparent top electrodes on highly dense ZnO nanowires by RF magnetron sputtering: deposition evolution and electrical properties", **Byung Oh Jung***, Dong Chan Kim, Ju Ho Lee, Jeong Yong Lee, Hyung Koun Cho, *TACT 2011 International Thin Films Conference*, B20110519019, Nov. 21, 2011, Kenting, Taiwan

12) "UV photodetector performance in highly dense ZnO nanowires with ultrathin MgO layers", Dong Chan Kim, **Byung Oh Jung**, Hyung Koun Cho*, *ICNFA 2011 - International Conference on Nanotechnology Fundamental and Applications*, p32, Jul. 28, 2011, Ottawa, Canada

13) "Enhanced pure ultraviolet emission of *n*-ZnO nanowire/*i*-MgO/p^+-Si heterojunction LEDs fabricated by metal-organic chemical vapor deposition", **Byung Oh Jung***, Dong Chan Kim, Ju Ho Lee, Jeong Yong Lee, Hyung Koun Cho, *2011 MRS (Materials Research Society) Spring Meeting & Exhibit*, EE9.22, Apr. 28, 2011, San Francisco, USA

14) "Highly sensitive ZnO nanowire UV photodetectors with dielectric MgO layers", Dong Chan Kim, **Byung Oh Jung***, Ju Ho Lee, Jeong Yong Lee, Hyung Koun Cho, *2011 MRS (Materials Research Society) Meeting & Exhibit*, EE9.7, Apr. 28, 2011, San Francisco, USA

C. Domestic Conference Presentations (* : Presenter)

01) "Realization of vertically well-aligned GaN nanowire based core-shell array growth by MOVPE : Morphology evolution and luminescent properties", **Byung Oh Jung**, Si-Young Bae, Masataka Imura, Yoshio Honda, Hiroshi Amano, *The 75th The Japan Society of Applied Physics (JSAP) Autumn Meeting*, 19p-PB6-25, Sep. 19, 2014, Hokkaido University, Japan

02) "Fabrication of p-Cu$_2$O / n-ZnO Nanowires Multidimensional Oxide Solar Cell grown by Metalorganic Chemical Vapor Deposition", **Byung Oh Jung**, Hyung Koun Cho, Sang Yun Kim, Ju Ho Lee, Jeong Yong Lee, *The 22th Materials Research Society of Korea Spring Meeting*, P-192, May. 17, 2012, Deogyusan Resort, Korea

03) "Effect of MgO carrier control layer on the pure UV emission from n-ZnO/i-MgO/p^+-Si heterostructure light emitting diodes", **Byung Oh Jung**, Yong Hun Kwon, Ju Ho Lee, Jeong Yong Lee, Hyung Koun Cho, *The 1th Korea Society of Optoelectronics Fall Meeting*, I-3, Nov. 17, 2011, Seoul National University, Korea

04) "Top electrode formation of transparent ITO for highly dense ZnO nanowires based opto-device by RF magnetron sputtering", **Byung Oh Jung**, Yong Hun Kwon, Hyung Koun Cho, *Conference on Electronic Materials & Nanotechnology for Green Environment (ENGE)*, N30, Oct. 28, 2011, Daejeon Convention Center, Korea

05) "Fully transparent UV photodetectors with high dense nanostructures", Dong Chan Kim, **Byung Oh Jung**, Yong Hun Kwon, Hyung Koun Cho, *The 12th Korean Institute of Electrical and Electronic Material Engineers (KIEEME) Annual Summer Meeting*, A1, Jun. 23, 2011, Hanwha Resort, Korea

06) "태양전지 응용을 위한 p-GaN 위에서의 n-ZnO 나노 막대 성장에 대한 연구", 서동주, 배시영, 심재필, 이동선, 정병오, 조형균, 제**18**회 광전자 및 광통신 학술회의, WP-III18, May 25, 2011, 경주대명리조트, 대한민국

07) "Pure ultraviolet emission of ZnO nanostructures light emitting diode caused by MgO insulating layer", **Byung Oh Jung**, Dong Chan Kim, Hyung Koun Cho, *2011 Conference of Korean Institute of Electrical and Electronic Material Engineers (KIEEME) Spring forum*, PO22, Apr. 22, 2011, Far East University, Korea

08) "Two dimensional ITO electrodes on high dense ZnO nanowires by RF magnetron sputtering: deposition evolution and photo-detecting properties", **Byung Oh Jung**, Dong Chan Kim, Hyung Koun Cho, *2011 The Korean Association of Crystal Growth Spring Meeting*, p-20, Apr. 15, 2011, Hanyang University, Korea

- ACKNOWLEDGEMENTS -

The Ph.D course at the Amano Lab has been the best time of my life. Above all, I would like to express my deepest appreciation sincerely to my supervisor Prof. Hiroshi Amano for encouraging, supporting, and advising me. It is difficult to express just how valuable his guidance has been. His scientific enthusiasm and professionalism have greatly shaped my thinking as a researcher and will be helpful in my future life. I would also like to take this opportunity to offer my congratulations on his Nobel Prize in Physics once again. Hearing the news of his award was a fantastic experience. Thank you, thank you for all you are doing. I would also like to thank Prof. Yoshio Honda for his dispassionate advice and opinions. I would like to thank the other professors of my Ph.D committee (Prof. Kazuo Nakazato, Prof. Hiroki Kondo, and Prof. Tomonori Ito) for their extensive opinions, advice, and support.

I'm very thankful to my coworker Dr. Si-Young Bae, who provided tremendous support in everyday discussions with me on my research topic, helping me to resolve issues in my work during our overlap. Special thanks are given to Mr. Yoshihiro Kato and Mr. Koji Neishi of Tokyo Electron Ltd. for their support in MOCVD maintenance and growth calibration. The collaboration with and support from Prof. Dong-Seon Lee at GIST in Korea have been very helpful, and Mr. Sang Yun Kim at KAIST in Korea helped enormously in TEM investigation. Also, I would like to thank all the members of the Amano Lab, especially Zheng Sun who endlessly helped me when I faced problems of Japanese language.

Special thanks are given to a long list of friends and colleagues, who helped me personally or professionally during my Ph.D course. I thank Prof. Hyung Koun Cho, Prof. Sung Wng Kim, Prof. Young Joon Hong, Dr. Dong Chan Kim, Dr. Bo Hyun Kong, Dr. Ji-Su Son, Dr. Ju Ho Lee, Yong Hun Kwon, Dong Kyu Seo, Dong Ju Seo, Ki Bum Song, Jeong Kyu Lee, and Sung Hwan Kim for their support.

ACKNOWLEDGEMENTS

Last but not least, I would like to thank my family for their constant love, confidence, and support. My lovely puppy pupu, you may rest in peace now without any suffering in the sky. Above all, I'm highly indebted to my wife MinJu Jang, who has stood by me and shown her love through the best and worst times during my Ph.D course. I promise you, I'll love you forever. You've made me so very happy.

Byung Oh Jung

Nagoya University

Sep. 2015

- CURRICULUM VITAE -

Sep., 2015

Byung Oh Jung

Nagoya University

Graduate School of Engineering

Department of Electrical Engineering and Computer Science

※ Personal Information

Gender	Male	Nationality	Korea
Date of Birth	May. 12. 1983		
Present Address	Amano Laboratory Dept. of Elect. Eng. and Com. Sci., Nagoya Univ. C3-1, Chikusa-ku, Nagoya, 464-8603, JAPAN		
E-mail	jungbyungoh@gmail.com, b_jung@nuee.nagoya-u.ac.jp		

※ Education

Ph. D.	Department of Electrical Engineering and Computer Science Nagoya University, Nagoya, Japan (2012.10 - 2015.09) **Supervisor : Prof. *Hiroshi Amano***
Thesis	Study on position-controlled GaN nanorod arrays and their application to three dimensional light emitting diodes
M. S.	School of Advanced Materials Science and Engineering Sungkyunkwan University, Korea (2010.09 - 2012.08) **Supervisor : Prof. *Hyung Koun Cho***
Thesis	Low-dimensional ZnO based photoelectronic devices
B. S.	Department of Electrical & Communication Engineering Hanyang University, Korea (2002.03 - 2010.02)

※ **Research Interests**

1) Position-controlled and self-assembled metalorganic chemical vapor deposition (MOCVD) growth of wide bandgap (II-VI or III-V) semiconductor nanostructures and thin film.

2) Doping, bandgap engineering, and heteroepitaxy in 1D nanostructures for quantum functional nanodevices

3) Synthesis of functional materials for photonics and energy application

4) Electrical and optical characterizations of 1D nanorod based quantum structures

※ **Representative Research Accomplishments**

1) Position-controlled MOCVD growth of GaN micro- and nanoarchitecture arrays

   : Position- and crystal facets- controlled selective area growth of GaN nanorod arrays

   : Realization of longer GaN nanorod over 5μm by multi-step MOCVD growth procedure

2) Self-assembled growth of ZnO nanowire arrays and MgZnO nanowalls

   : Shape-controlled nanoarchitecturing by MOCVD growth procedure

3) Metalorganic chemical vapor deposition (MOCVD)

   : In$_{1-x}$Ga$_x$N/GaN quantum structure of thinfilm and coaxial nanostructure

   : Doping of Si and Mg in GaN

4) Device fabrication

   : Wavelength-tuned In$_{1-x}$Ga$_x$N/GaN coaxial nanorod embedded 3D-LEDs

   : Thin film based LEDs from violet to green

   : Thin film (2D) - nanorod (1D) hybrid structure LEDs

   : Oxide material based functional opto-electronic device

5) Etc.

   : Thin films deposition by RF sputtering & Atomic layer deposition (ALD) systems